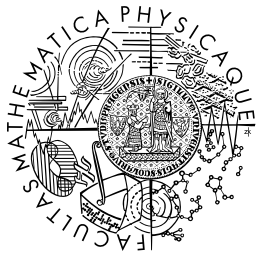

FACULTY
OF MATHEMATICS
AND PHYSICS
Charles University

DOCTORAL THESIS

Maxim Tchaplianka

Electronic structure and magnetic properties of materials with strong electron-electron correlations

Institute of Physics of the Czech Academy of Sciences

Supervisor of the doctoral thesis: Ing. Alexander B. Shick, CSc., DSc.

Study programme: Physics (P1701)

Study branch: Physics of Condensed Matter and Materials Research (4F3)

Prague 2023

I declare that I carried out this doctoral thesis independently, and only with the cited sources, literature and other professional sources. It has not been used to obtain another or the same degree.

I understand that my work relates to the rights and obligations under the Act No.~121/2000 Sb., the Copyright Act, as amended, in particular the fact that the Charles University has the right to conclude a license agreement on the use of this work as a school work pursuant to Section 60 subsection 1 of the Copyright~Act.

In ..... date ....

Author's signature

I would like to thank my supervisor Dr. Alexander Shick for the guidance and motivation. I would also like to thank Dr. Jindrich Kolorenč, the head of the condensed matter theory department in FZU, for reviewing this work and giving much needed criticism and advice. I would also like to thank my parents and my brother Anton for their love and support. Finally, I would like to thank my wonderful wife Wenrui, for giving me something worth struggling for.

The study presented in this thesis was financially supported by Operational Programme Research, Development and Education financed by European Structural and Investment Funds and the Czech Ministry of Education, Youth and Sports (Project No. SOLID21 - CZ.02.1.01/0.0/0.0/16_019/0000760), and by the Czech Science Foundation (GACR) Grant No. 21-09766S.

Title: Electronic structure and magnetic properties of materials with strong electron-electron correlations

Author: Maxim Tchaplianka

Department: Institute of Physics of the Czech Academy of Sciences

Supervisor: Ing. Alexander B. Shick, CSc., DSc., Institute of Physics of the Czech Academy of Sciences

Abstract: In this thesis, we present several computational methods of studying magnetic materials, and apply them to several real materials. Density functional theory with exact diagonalization is used to investigate three materials which consist of a cobalt impurity coupled to a metallic substrate. The observables and spectral densities found in each case are presented. Next, FeHfSb and $UFe_{10}Si_2$ are investigated as potentially magnetically hard materials, via the calculation of their magnetocrystalline anisotropy and thermodynamic stability.

Keywords: density functional theory, Anderson impurity model, exact diagonalization, magnetic anisotropy, Kondo effect

Contents

Introduction

In the field of condensed matter physics, one of the domains known to produce complex emergent properties is that of strong electron-electron correlations. Band theory, the most straightforward approach to solid state physics, breaks down when electron-electron interactions are significantly stronger than the width of energy bands. This allows for the appearance of a wealth of physical phenomena that goes beyond the standard properties of metals and insulators. Examples include high-temperature superconductivity in cuprates [1], metal–insulator transitions triggered by environmental changes [2], and the emergence of quasiparticles like heavy fermions [3]. Those properties are of great scientific and industrial interest.

Strongly correlated materials typically have incompletely filled d-shells and f-shells, as those shells are more localized and have narrower energy bands. A particular class of materials that exhibits interesting strongly-correlated properties is metals with embedded or adhesed impurities — atoms of a different element from the material's composition which break the crystal's symmetry. Under some conditions, impurities with magnetic moment may cause the appearance of the Kondo effect — the existence of a conductivity minimum at a finite temperature. Moreover, magnetic impurities play a major role in inducing magneto-crystalline anisotropy in materials, giving their magnetization a preferred direction.

Ab-initio computational exploration of strongly correlated materials is not straightforward, since electronic structure methods generally assume weak electron correlations. The usual approach thus involves combining an ab-initio method with a method that can model strong interactions, such as dynamical mean-field theory (DMFT) or exact diagonalization (ED).

One of the most popular ab-initio methods is density functional theory (DFT), a versatile method for calculating the electronic density of a many-body system using a self-consistent loop. DFT can employ a wide variety of formalisms and approximations suited for different materials and different degrees of balance between precision and efficiency. These include local approximations of the exchange interaction, effective potential treatment of the atomic cores, selection of basis set and the incorporation of additional phenomena, such as spin-orbit coupling and magnetic fields.

As mentioned before, on its own DFT is insufficient for dealing with strongly-correlated materials, since approximations of the exchange interaction assume a locally homogeneous density, characteristic of weakly-interacting electrons. A common variant of DFT that addresses the issue is DFT+U, which includes an additional energy term for the d and f-shells in the vicinity of nuclei. The interaction energy is calculated from the density matrix, and is approximated according to the nature of the problem.

Another approach, used specifically for magnetic impurities, employs the Anderson impurity model (AIM). Under AIM, the impurity's orbital structure is described by a local Hamiltonian matrix, and the rest of the system, named the "bath" for its thermodynamic role, is described as a spectrum of states, coupled to the impurity. The combination of the two methods is performed by using the projected density of states (DOS) of the impurity as calculated in DFT to construct AIM, which is then solved by a quantum Monte Carlo (QMC) algorithm. Alternately, the bath can be discretized so that the system's entire Hamiltonian can be solved by exact diagonalization (ED). This method is known as DFT+ED.

The objectives of this thesis are to study the strengths and limitations of DFT+U and DFT+ED, to apply those computational methods to systems with magnetic impurities, and to evaluate their performance by comparing them to experimental results, as well as to other ab-initio work.

The structure of this thesis is as follows:

- Chapter 1 lays out the formalism and assumptions behind density functional theory and presents an overview of some of the methods applied to each part of it that are relevant to our work.

- Chapter 2 covers the Anderson impurity model and the many-body formalism used to describe it. This part describes how the results of a DFT calculation can be used to build an impurity that includes electron-electron interaction in the impurity, crystal field splitting and spin-orbit coupling.QMC is briefly described as one of the methods commonly used to solve AIM. Then, the method of exact diagonalization of a discretized impurity model is described, along with implementation details.

- Chapter 3 documents the application of DFT+ED to three systems of magnetic cobalt impurities coupled to crystals — a cobalt atom in bulk copper, a cobalt adatom on a copper surface, and finally a copper adatom on a Cu_2N surface which itself is situated on copper. For each system, FLAPW with LDA is used to calculate the projected DOS on the impurity's valence shell, which is then used to create a discrete model, solvable by Lanczos diagonalization. The results for cobalt atom in bulk copper are compared to calculations performed with CT-QMC. The adatom systems' ground states were interpreted using a phenomenological model of magnetic anisotropy, finding Kondo resonance. Their differential conductance was characterized and compared to experimental results.

- Chapter 4 deals with the magnetic properties of two permanent magnet candidates — Fe_2Hf doped with antimony and UFe_{12} doped with silicon. FLAPW is used to calculate the magnetic parameters of each crystal and to compare them to the required properties of good permanent magnets.

Additionally, there are three appendices. Appendix A.1 specifies the notational conventions used in this thesis. Appendix A.2 gives additional details on the Metropolis-Hastings algorithm of CT-QMC. Appendix A.3 shows how the Kondo model is derived from the single-impurity Anderson model.

Chapter 1

Density functional theory

1.1 Basics

Density functional theory is one of the most popular methods for computational modeling and investigation of many-body quantum systems. Its original form was introduced by Hohenberg and Kohn in 1964, building on previous density functional formalism by Thomas and Fermi [4].

DFT describes a many-body system of nuclei and N electrons which uses the Born-Oppenheimer approximation [5] — the nuclei are assumed to be static, which allows us to separate the total wavefunction into the nuclear and electronic parts, remove the nuclear kinetic term from the Hamiltonian and convert the electron-nucleon interaction into a static potential. The system's Schrödinger equation can then be described solely in the electronic Hilbert space.

$$\hat{H}\psi_j\left(\{\mathbf{r}_1 \dots \mathbf{r}_N\}\right) = E_j\psi_j\left(\{\mathbf{r}_1 \dots \mathbf{r}_N\}\right) \tag{1.1}$$

The system is assumed to be spinless. The extention to spin-polarized systems is done by converting the wavefunction into a two-component spinor.

The Hamiltonian consists of three operators:

$$\hat{H} = \hat{T} + \hat{V} + \hat{U}. \tag{1.2}$$

$\hat{T} = -\frac{1}{2}\sum_{n=1}^{N}\nabla_n^2$ represents kinetic energy, $\hat{V} = \sum_{n=1}^{N} V\left(\mathbf{r}_n\right)$ represents electron-nucleus interaction and $\hat{U} = \sum_{n\neq n'}\frac{1}{|\mathbf{r}_n - \mathbf{r}_{n'}|}$ represents electron-electron interaction (we use a reduced unit system where $m = e = \hbar = 1$). While $\hat{T}$ and $\hat{U}$ are universal operators, $\hat{V}$ is unique for every system and encodes its atomic structure.

Exact solution of the system is not viable for more than very few electrons. Fortunately, in systems where interactions are weak and local, the one-electron approximation is sufficient to describe the system's physics up to a satisfactory degree of accuracy. Being a one-electron method, the principal parameter of DFT is electron density, which is found by integrating out all spatial degrees of freedom out of the probability density save for one:

$$\rho\left(\mathbf{r}\right) \equiv \left|\langle \mathbf{r}_2, \dots, \mathbf{r}_N | \mathbf{r}, \mathbf{r}_2, \dots, \mathbf{r}_N \rangle\right|^2 = \int \mathrm{d}\mathbf{r}_2 \cdots \int \mathrm{d}\mathbf{r}_N \left|\psi\left(\mathbf{r}, \mathbf{r}_2, \dots, \mathbf{r}_N\right)\right|^2. \tag{1.3}$$

The density element $\rho(\mathbf{r})\,\mathrm{d}\mathbf{r}$ can be interpreted as the probability of finding an electron at a certain point in volume element . The density can also be expressed in the second quantization formalism using the operators $c^\dagger(\mathbf{r})$ and $c(\mathbf{r})$ which respectively create and annihilate an electron at position $\mathbf{r}$ in the state $|\psi\rangle$:

$$\rho(\mathbf{r}) = \langle\psi| c^\dagger(\mathbf{r})\, c(\mathbf{r}) |\psi\rangle . \tag{1.4}$$

Though the integration removes most of the information in the wavefunction, the electron density still contains much chemically-useful information. In particular, the projection of the density on the eigenstates of a single atom characterizes the coupling between it and the environment.

The ground state density $\rho_0(\mathbf{r})$ is found by expressing the system's energy as a functional of the electronic density and finding the functional's global minimum. The total energy functional is defined as

$$E[\rho] \equiv \min_{\{\psi|\rho=\rho(\psi)\}} \langle\psi| \hat{H} |\psi\rangle . \tag{1.5}$$

(For brevity, in the expressions of other energy functionals below, $\min_{\{\psi|\rho=\rho(\psi)\}}$ will be omitted.) In words, the energy functional $E[\rho]$ returns the eigen-energy of the Hamiltonian corresponding to the least energetic wavefunction ψ whose electronic density is ρ.

The energy functional can be separated in the same manner as Eq. (1.2):

$$E[\rho] = T[\rho] + V[\rho] + U[\rho] . \tag{1.6}$$

The nucleus-electron interaction functional can be expressed exactly as a function of the electronic density:

$$V[\rho] = \langle\psi| c^\dagger(\mathbf{r})\, V(\mathbf{r})\, c(\mathbf{r}) |\psi\rangle = \int \mathrm{d}^3\mathbf{r} V(\mathbf{r})\, \rho(\mathbf{r}) . \tag{1.7}$$

The electron-electron interaction functional $U[\rho]$ has coupling terms between every two possible $|\psi\rangle$ states. The leading terms of the functional include two-electron interactions, and will be separated from the rest of the functional, which will be dubbed the correlation term $E_\mathrm{c}[\rho]$. The antisymmetry of the electron wavefunction necessitates differentiating the creation and annihilation operators by index. The electron-electron interaction is thus

$$\begin{aligned} U[\rho] &= \langle\psi| c_m^\dagger(\mathbf{r})\, c_n^\dagger(\mathbf{r}') \frac{1}{|\mathbf{r}-\mathbf{r}'|} c_n(\mathbf{r}')\, c_m(\mathbf{r}) |\psi\rangle \\ &\quad - \langle\psi| c_m^\dagger(\mathbf{r})\, c_n^\dagger(\mathbf{r}') \frac{1}{|\mathbf{r}-\mathbf{r}'|} c_m(\mathbf{r}')\, c_n(\mathbf{r}) |\psi\rangle + E_\mathrm{c}[\rho] \\ &= \iint \mathrm{d}^3\mathbf{r}\mathrm{d}^3\mathbf{r}' \frac{\rho(\mathbf{r})\,\rho(\mathbf{r}')}{|\mathbf{r}-\mathbf{r}'|} + E_\mathrm{x}[\rho] + E_\mathrm{c}[\rho] . \end{aligned} \tag{1.8}$$

The first term (often called the Hartree term) represents the classical Coulomb repulsion between electrons, appearing as interaction between different parts of

the electronic density. The second term (often called the Fock term) represents the exchange interaction, and can be seen as a correction to Eq. (1.8) that removes the self-interaction from the first term. It can be expressed in terms of the two-electron density

$$\rho(\mathbf{r},\mathbf{r}') \equiv \int \mathrm{d}\mathbf{r}_3 \cdots \int \mathrm{d}\mathbf{r}_N \left|\psi(\mathbf{r},\mathbf{r}',\mathbf{r}_3,\ldots,\mathbf{r}_N)\right|^2 = \langle\psi| c^\dagger(\mathbf{r}) c(\mathbf{r}') |\psi\rangle ,$$

so that

$$E_\mathrm{x}[\rho] = -\iint \mathrm{d}^3\mathbf{r}\mathrm{d}^3\mathbf{r}' \frac{\left|\rho(\mathbf{r},\mathbf{r}')\right|^2}{|\mathbf{r}-\mathbf{r}'|}.$$

As with the electronic density, $\rho(\mathbf{r},\mathbf{r}')\,\mathrm{d}^3\mathbf{r}\mathrm{d}^3\mathbf{r}'$ can be interpreted as the probability of finding an electron in each of the points $\mathbf{r}$ and $\mathbf{r}'$.

The correlation term $E_\mathrm{c}[\rho]$ represents the remainder of $U[\rho]$ — the part of the electron-electron energy which isn't covered by the Hartree and Fock terms. It has no exact expression, and an appropriate approximation is chosen on case-by-case basis. The exchange and correlation interactions are usually grouped together as the exchange-correlation (xc) term:

$$E_\mathrm{xc}[\rho] = E_\mathrm{x}[\rho] + E_\mathrm{c}[\rho] ,$$

since electronic density approximations treat both at the same time.

Due to the contribution of electronic correlation to the total kinetic energy, the kinetic energy functional can only be expressed exactly in the case with no electron-electron interactions, where each electron is subject only to the external atomic potential. The kinetic energy energy can be split into the non-interacting term

$$T_0[\rho] = -\frac{1}{2}\langle\psi| c^\dagger(\mathbf{r}) \nabla^2 c(\mathbf{r}) |\psi\rangle = -\frac{1}{2}\int \mathrm{d}^3\mathbf{r}\rho(\mathbf{r})\nabla\rho(\mathbf{r}) \tag{1.9}$$

and the correction term $T_c[\rho]$ which is incorporated into the correlation term $E_\mathrm{c}[\rho]$.

It is customary to group the universal functionals into a single functional $F[\rho] \equiv T[\rho] + U[\rho]$, since it can be explored and approximated analytically on its own. The total energy can thus be expressed as the sum

$$E[\rho] = F[\rho] + \int \mathrm{d}^3\mathbf{r} V(\mathbf{r})\rho(\mathbf{r}) , \tag{1.10}$$

where the first element is universal and the second is particular to the system.

1.2 Hohenberg-Kohn theorems and Kohn-Sham equations

DFT relies on the two Hohenberg-Kohn theorems [4].

Theorem 1. *The external single-particle potential $V(\mathbf{r})$ and the ground state electron density $\rho_0(\mathbf{r})$ are unique functionals of each other*[1].

The ground state density $\rho_0(\mathbf{r})$ is determined uniquely from $V(\mathbf{r})$ via the ground eigenstate of the Hamiltonian which uses $V(\mathbf{r})$ as the nuclear potential. $V(\mathbf{r})$ is determined uniquely from $\rho_0(\mathbf{r})$ up to a constant due to the fact that two different nuclear potentials cannot produce the same electron density. This can be proven by contradiction — if two such potentials existed, it could be shown that the ground-state energy of each of their Hamiltonians would be smaller than the other one [4]. As a consequence, the solution of the system depends on finding self-consistency between the Hamiltonian and the electronic density. Another consequence is that the ground-state density $\rho_0(\mathbf{r})$ not only represents the ground state, but determines all of the system's excited states as well via the Hamiltonian.

Theorem 2. *The energy functional $E[\rho]$ has a minimum at the ground state density ρ_0.*

The second theorem implies that the ground-state energy is

$$E[\rho_0] = \min_{\rho} \{E[\rho]\}. \tag{1.11}$$

It can be proven using Rayleigh-Ritz variational principle [5]. An arbitrary state $|\psi\rangle$ in the system is expanded in the eigenstate basis:

$$|\psi\rangle = \sum_{n=0}^{\infty} C_n |\psi_n\rangle .$$

The energy of the state is (assuming the state has been normalized)

$$E = \langle\psi| \hat{H} |\psi\rangle = \sum_{n=0}^{\infty} |C_n|^2 E_n.$$

If E_0 is the lowest energy (assuming no degeneracy), then it is also the lowest value E can take, and occurs only if $|\psi\rangle = |\psi_0\rangle$, which is the state corresponding to the density ρ_0. Therefore

$$E[\rho_0] = E_0.$$

The formal solution for DFT thus involves the minimization of the energy functional under a conserved number of electrons. Since the number of electrons is

$$N = \int \mathrm{d}^3\mathbf{r}' \rho(\mathbf{r}'),$$

the condition can be expressed using the Lagrange multiplier μ as

[1] Though this formulation assumes unique ground states, the theory has been extended to degenerate ground states [6].

$$\frac{\delta}{\delta\rho\left(\mathbf{r}\right)}\left(E\left[\rho\left(\mathbf{r}\right)\right]-\mu\left(\int \mathrm{d}^3\mathbf{r}'\rho\left(\mathbf{r}'\right)-N\right)\right)=0, \tag{1.12}$$

which reduces to

$$\frac{\delta E\left[\rho\left(\mathbf{r}\right)\right]}{\delta\rho\left(\mathbf{r}\right)}=\mu. \tag{1.13}$$

We use $F\left[\rho\right]$ from Eq. (1.10) in order to separate the equation into the universal and particular parts.

$$\frac{\delta F\left[\rho\left(\mathbf{r}\right)\right]}{\delta\rho\left(\mathbf{r}\right)}+V\left(\mathbf{r}\right)=\mu. \tag{1.14}$$

Solving Eq. (1.14) directly via a minimization algorithm is not practical due to the effectively infinite dimensions of the space of possible densities, and because the exact functional $F\left[\rho\left(\mathbf{r}\right)\right]$ is not known. In order to make the evaluation of the condition more tractable, the system will be mapped to an effective non-interacting model with an effective potential $V_{\mathrm{eff}}\left(\mathbf{r}\right)$. Its energy functional is

$$E_{\mathrm{eff}}\left[\rho\right]=T_0\left[\rho\right]+\int \mathrm{d}^3\mathbf{r}V_{\mathrm{eff}}\left(\mathbf{r}\right)\rho\left(\mathbf{r}\right). \tag{1.15}$$

By equating this energy functional with the exact one in Eq. (1.6), $V_{\mathrm{eff}}\left(\mathbf{r}\right)$ can be written as

$$V_{\mathrm{eff}}\left(\mathbf{r}\right)=V\left(\mathbf{r}\right)+\int \mathrm{d}^3\mathbf{r}V\left(\mathbf{r}\right)\rho\left(\mathbf{r}\right)+V_{\mathrm{xc}}\left(\mathbf{r}\right), \tag{1.16}$$

with the xc potential

$$V_{\mathrm{xc}}\left(\mathbf{r}\right)\equiv\frac{E_{\mathrm{xc}}\left[\rho\left(\mathbf{r}\right)\right]}{\delta\rho\left(\mathbf{r}\right)}.$$

Substituting the energy functional from Eq. (1.15) into Eq. (1.14) gives the minimization equation for the effective system:

$$\frac{\delta T_0\left[\rho\left(\mathbf{r}\right)\right]}{\delta\rho\left(\mathbf{r}\right)}+V_{\mathrm{eff}}\left(\mathbf{r}\right)=\mu.$$

The many-body ground state wavefunction of the non-interacting system is a Slater determinant of the single-particle orbitals:

$$\psi\left(\mathbf{r}_1\ldots\mathbf{r}_N\right)=\begin{vmatrix}\phi_1\left(\mathbf{r}_1\right) & \cdots & \phi_N\left(\mathbf{r}_1\right)\\ \vdots & \ddots & \vdots\\ \phi_1\left(\mathbf{r}_N\right) & \cdots & \phi_N\left(\mathbf{r}_N\right)\end{vmatrix} \tag{1.17}$$

Each of the single-particle wavefunctions can be derived by solving a single-particle Schrödinger equation with the effective potential $V_{\mathrm{eff}}\left(\mathbf{r}\right)$, known as the Kohn-Sham equation:

$$\left(-\frac{1}{2}\nabla^2 + V_{\text{eff}}(\mathbf{r})\right)\phi_n(\mathbf{r}) = \varepsilon_n\phi_n(\mathbf{r}). \tag{1.18}$$

The ground state density of the effective system is equal to the ground state density of the original system, due to the equivalence of their energy functionals. It is built from the eigenstates of Eq. (1.18) as

$$\rho_0(\mathbf{r}) = \sum_{n=1}^{N} |\phi_n(\mathbf{r})|^2. \tag{1.19}$$

The Kohn-Sham system's total energy can be expressed in terms of functionals by integrating Eq. (1.18) over all eigenfunctions:

$$T_0[\rho_0] + \int \mathrm{d}\mathbf{r}\rho_0(\mathbf{r}) V_{\text{eff}}[\rho_0] = \sum_{n=1}^{N} \epsilon_n. \tag{1.20}$$

By combining Eq. (1.15), Eq. (1.16) and Eq. (1.20), we get the total energy, which is the quantity that is being minimized by the whole process [7]:

$$E = \sum_{n=1}^{N} \epsilon_n - \frac{1}{2}\int \mathrm{d}\mathbf{r}\frac{\rho_0(\mathbf{r})\rho_0(\mathbf{r}')}{|\mathbf{r}-\mathbf{r}'|} - \int \mathrm{d}\mathbf{r}\rho_0(\mathbf{r}) V_{\text{xc}}(\mathbf{r}) + E_{\text{xc}}[\rho]. \tag{1.21}$$

All of the basic components of the DFT process have introduced. Its purpose is to achieve self-consistency between the electron density and the energy functional by repeatedly calculating one from the other until the system's energy stabilizes. There are many variations on this common theme, differing from each other by their choice of basis, method of solving the Kohn-Sham equation, the approximation of the exchange correlation, the inclusion of additional phenomena, like spin or a magnetic field, and extensions to relativistic and time-dependent theories. Those choices determine the quality and value of the process — how quickly will the loop converge, how long will each iteration take, how closely will the converged energy and ground state match the real values, how much will the conserved quantities be conserved, and ultimately how much will the resulting model reflect the behavior of the real material under study.

Below is a short overview of various DFT methods, categorized by the part of the process they address. Some of those will be presented in the following sections:

1. xc functional approximation (electron-electron potential)
   (a) Local density approximation (LDA)
   (b) generalized gradient approximation (GGA)
2. Basis set
   (a) Augmented plane-wave (APW), linearized APW (LAPW)
   (b) Korringa-Kohn-Rostoker (KKR), linearized muffin-tin orbitals (LMTO)

3. Effective potential treatment (electron-nucleus potential)
   (a) Muffin-tin potential
   (b) Pseudo-potential, ultrasoft pseudopotential
   (c) Full-potential
   (d) Atomic sphere approximation (ASA)
4. Additional phenomena
   (a) Spin-polarization, spin-orbit coupling, magnetic field (LSDA)
   (b) DFT+U (particularly LDA+U)
   (c) Relativistic kinetic energy
   (d) Time-dependent electron-nucleus interaction

1.3 Local density approximation

Though the xc energy functional in Eq. (1.8) cannot be expressed exactly as a functional of ρ, it can be approximated by one of several xc functionals that differ in accuracy and complexity. The simplest of those is LDA. It exploits the short range of xc interactions and assumes that it depends only on the electronic density at each point in space. The functional then takes a similar form to that of the electron-nucleus interaction term:

$$E_{\mathrm{xc}}^{\mathrm{LDA}}[\rho] = \int \mathrm{d}^3\mathbf{r}\rho(\mathbf{r})\,\varepsilon_{\mathrm{xc}}(\rho(\mathbf{r}))\,. \tag{1.22}$$

$\varepsilon_{\mathrm{xc}}(\rho(\mathbf{r}))$ is the xc energy per particle of a homogeneous electron gas. The effective LDA xc potential is [5]

$$V_{\mathrm{xc}}^{\mathrm{LDA}}(\mathbf{r}) = \frac{\delta E_{\mathrm{xc}}^{\mathrm{LDA}}}{\delta\rho} = \varepsilon_{\mathrm{xc}}(\rho(\mathbf{r})) + \rho(\mathbf{r})\frac{\delta\varepsilon_{\mathrm{xc}}(\rho(\mathbf{r}))}{\delta\rho}.$$

The $\varepsilon_{\mathrm{xc}}(\rho(\mathbf{r}))$ function can be divided into exchange and correlation parts:

$$\varepsilon_{\mathrm{xc}}(\rho) = \varepsilon_{\mathrm{x}}(\rho) + \varepsilon_{\mathrm{c}}(\rho)\,. \tag{1.23}$$

The exchange energy, being a compensation for the self-interaction in the Coulomb term, can be expressed as interaction with the effective Kohn-Sham exchange hole function $\rho_{\mathrm{x}}(\mathbf{r},\mathbf{r}')$:

$$E_{\mathrm{xc}}^{\mathrm{LDA}}[\rho] = \int \mathrm{d}^3\mathbf{r}\frac{\rho(\mathbf{r})\,\rho_{\mathrm{x}}(\mathbf{r},\mathbf{r}')}{|\mathbf{r}-\mathbf{r}'|}. \tag{1.24}$$

In order to cancel the self-interaction exactly, the hole function should have a total charge exactly inverse to that of a single electron. This is known as the sum rule

$$\int \mathrm{d}\mathbf{r}\rho_{\mathrm{x}}\left(\mathbf{r},\mathbf{r}'\right)=-1. \tag{1.25}$$

The simplest expression of $E_{\mathrm{x}}^{\mathrm{LDA}}\left[\rho\right]$ that fulfills the above criterion is the Thomas-Fermi approximation, the progenitor of DFT [5]. By demanding that

$$E_{\mathrm{x}}^{\mathrm{TF}}\left[\rho\right]=-\frac{3}{4}\left(\frac{3}{\pi}\right)^{\frac{1}{3}}\int \mathrm{d}\mathbf{r}\rho^{\frac{4}{3}}\left(\mathbf{r}\right)\overset{!}{=}\int \mathrm{d}\mathbf{r}\rho\left(\mathbf{r}\right)\varepsilon_{\mathrm{x}}^{\mathrm{TF}}\left(\rho\left(\mathbf{r}\right)\right),$$

we get

$$\varepsilon_{\mathrm{x}}^{\mathrm{TF}}\left(\rho\right)=-\frac{3}{4}\left(\frac{3}{\pi}\rho\right)^{\frac{1}{3}}.$$

$\varepsilon_{\mathrm{c}}\left(\rho\right)$ doesn't have an analytical expression, but it can be calculated using quantum Monte Carlo [8, 9].

1.3.1 Local spin density approximation

The DFT formalism as described in Chapter 1 applies to a spinless system. A spinless approach is insufficient for our work, since magnetic phenomena necessarily involve spin polarization. Spin-dependence can be worked into the theoretical model either in the DFT phase or in the AIM phase that comes later (and is described in Sec. 2.3). The former case requires the extension of the DFT formalism to the spin-dependent case.

The full $\frac{1}{2}$-spin density requires two scalar fields, for the two directions of spin along some axis (conventionally $\hat{z}$) — $\rho_{\uparrow}\left(\mathbf{r}\right)$ and $\rho_{\downarrow}\left(\mathbf{r}\right)$ [10]. The electronic density used up until now has been the sum of the two fields:

$$\rho\left(\mathbf{r}\right)=\rho_{\uparrow}\left(\mathbf{r}\right)+\rho_{\downarrow}\left(\mathbf{r}\right).$$

The Kohn-Sham eigenstates would also need to be spin-dependent, so that the electronic density of each spin can be expressed as

$$\rho_{\sigma}\left(\mathbf{r}\right)=\sum_{n}\phi_{n\sigma}\left(\mathbf{r}\right)\phi_{n\sigma}\left(\mathbf{r}\right).$$

Out of the functionals, the only one with an explicit spin dependence is the xc energy. The treatment of spin-polarization can thus be performed using local spin density approximation (LSDA)[2].

The magnetization density is

$$\mathbf{m}\left(\mathbf{r}\right)=\sum_{n\sigma\sigma'}\phi_{n\sigma}\left(\mathbf{r}\right)\left[\vec{\sigma}\right]_{\sigma\sigma'}\phi_{n\sigma'}\left(\mathbf{r}\right),$$

where $\vec{\sigma}$ is the Pauli matrix vector

[2] A complete extension of the DFT formalism to the spin polarized case can be read in Ref. [11].

$$\vec{\sigma} = \begin{pmatrix} 0 & 1 \\ 1 & 0 \end{pmatrix} \hat{x} + \begin{pmatrix} 0 & -i \\ i & 0 \end{pmatrix} \hat{y} + \begin{pmatrix} 1 & 0 \\ 0 & -1 \end{pmatrix} \hat{z}. \tag{1.26}$$

The presence of magnetization requires the introduction of a new term to the xc potential — the internal magnetic field [10]

$$\mathbf{B}_{\mathrm{xc}}(\mathbf{r}) = -\frac{\delta E_{\mathrm{xc}}[\rho, \mathbf{m}]}{\delta \mathbf{m}}.$$

The LSDA xc potential is

$$V_{\mathrm{xc}}^{\mathrm{LSDA}}(\mathbf{r}) = \varepsilon_{\mathrm{xc}}(\rho(\mathbf{r}), \mathbf{m}(\mathbf{r})) + \rho(\mathbf{r}) \frac{\delta \varepsilon_{\mathrm{xc}}(\rho(\mathbf{r}))}{\delta \rho} - \mathbf{B}_{\mathrm{xc}}(\mathbf{r}) \cdot \vec{\sigma}.$$

In the standard choice of $\hat{z}$ as the axis of magnetization, $\mathbf{m}(\mathbf{r}) = m(\mathbf{r})\hat{z}$ with

$$m(\mathbf{r}) = \rho_{\uparrow}(\mathbf{r}) - \rho_{\downarrow}(\mathbf{r}).$$

The LSDA energy functional can be expressed as $E^{\mathrm{LSDA}}[\rho, m]$, with only the xc term depending on m.

1.3.2 LSDA+U

LDA and LSDA have a weakness in treating materials where the density can't be assumed to be locally homogeneous. As such, it is unsuitable for treating strongly correlated atoms, such as transition metals and rare earth elements. The popular method of dealing with such systems is to explicitly introduce to make the energy functional directly dependent on interaction between local electronic orbitals [12]. This allows DFT, generally a weak interaction method, to be applied to strongly correlated systems.

The LSDA+U xc functional is generated by adding to the LSDA energy functional the electron-electron interaction term $E^{\text{e-e}}[n_{\gamma\gamma'}]$ (here $\gamma \equiv m\sigma$ is a common index for both the spin and orbit) and subtracting the double-counting term $E^{\mathrm{DC}}[n_{\gamma\gamma'}]$. Both of those are functionals of $n_{\gamma\gamma'} \equiv \left\langle c_{\gamma}^{\dagger} c_{\gamma'} \right\rangle$, the occupation matrix of local spin-orbitals γ and γ'. The energy functional is then

$$E^{\mathrm{LSDA+U}}[\rho, m, n_{\gamma\gamma'}] = E^{\mathrm{LSDA}}[\rho, m] + E^{\text{e-e}}[n_{\gamma\gamma'}] - E^{\mathrm{DC}}[n_{\gamma\gamma'}]. \tag{1.27}$$

The interaction term is [13]

$$E^{\text{e-e}}[n_{\gamma\gamma'}] = \frac{1}{2} \sum_{\{\gamma_i\}} n_{\gamma_1\gamma_2} \left(U_{\gamma_1\gamma_3\gamma_2\gamma_4}^{\text{e-e}} - U_{\gamma_1\gamma_3\gamma_4\gamma_2}^{\text{e-e}} \right) n_{\gamma_3\gamma_4}, \tag{1.28}$$

where $\hat{U}^{\text{e-e}}$ is the interaction matrix between orbitals:

$$U_{\gamma_1\gamma_3\gamma_2\gamma_4}^{\text{e-e}} = \langle \psi | c_{\gamma_1}^{\dagger}(\mathbf{r}) c_{\gamma_3}^{\dagger}(\mathbf{r}') \frac{1}{|\mathbf{r} - \mathbf{r}'|} c_{\gamma_4}(\mathbf{r}') c_{\gamma_2}(\mathbf{r}) | \psi \rangle \delta_{\sigma_1\sigma_2} \delta_{\sigma_3\sigma_4}. \tag{1.29}$$

The interaction matrix can be expressed in a manner that highlights its symmetry in the spherical basis around the atomic nucleus. It's expressed as a series of terms, each having a lower symmetry than the previous one [14]:

$$U^{\text{e-e}}_{\gamma_1\gamma_3\gamma_2\gamma_4} = \sum_{n=0}^{l} a_{2n}\left(m_1, m_3, m_2, m_4\right) F_{2n}, \tag{1.30}$$

with l as the valence shell's azimuthal quantum number. Each term in this expression is separated into the radial and angular components. The Slater integrals F_n are integrals over the products of radial parts, and a_n are products of spherical harmonics:

$$a_n\left(m_1, m_3, m_2, m_4\right) = \frac{4\pi}{2n+1} \sum_{q=-n}^{n} \left\langle lm_1\right| Y_n^q \left|lm_3\right\rangle \left\langle lm_2\right| \left[Y_n^q\right]^\star \left|lm_4\right\rangle .$$

The Slater integrals for the unscreened potential can be calculated from the radial parts $R\left(r\right)$ of the atomic orbitals [15]:

$$F_k = \int_0^\infty r_1^2 \mathrm{d}r \int_0^\infty r_2^2 \mathrm{d}r R^2\left(r_1\right) R^2\left(r_2\right) \frac{r_<^k}{r_>^{k+1}}.$$

Those values, however, will be vastly exaggerated for atoms embedded inside a material. There are multiple ways to address the problem. The Slater integrals can be used as parameters and be reduced by some amount, judged by the agreement of the observables (e.g. the impurity occupation or magnetic moment) with values achieved in other methods (experimental or computational). Alternatively, the values can be taken from ab-initio calculations using methods such as constrained LDA [16] or constrained random-phase approximation (cRPA) [17]. Both approaches are used in this work.

Generally, the Slater integrals are expressed in terms of Coulomb direct interaction U and exchange interaction J. for d-shell orbitals ($l = 2$), those are [12]

$$\begin{aligned} F_0 &= U, \\ F_2 &= 8.615J, \\ F_4 &= 0.625F_2. \end{aligned}$$

For f-shell orbitals ($l = 3$), [12]

$$\begin{aligned} F_0 &= U, \\ F_2 &= 11.922J, \\ F_4 &= 0.668F_2, \\ F_6 &= 0.494F_2. \end{aligned}$$

1.3.2.1 Double-counting

The functional $E^{\text{e-e}}\left[n_{\gamma\gamma'}\right]$ accounts for all interactions, including terms that have already been accounted for in $U\left[\rho\right]$. Those terms need to be explicitly substracted

from $E^{\text{e-e}}\left[n_{\gamma\gamma'}\right]$ in the form of $E^{\text{DC}}\left[n_{\gamma\gamma'}\right]$. The double-counting term approximates the value of $E^{\text{e-e}}$ in the absence of orbital polarization (so that the LSDA+U functional will converge to the LSDA functional), and is a function of the occupation matrix's orbital trace $n_\sigma \equiv \text{Tr}_{mm'}\left[n_{mm'\sigma\sigma}\right]$.

Two commonly used approximations for the double counting term in d and f orbitals are the fully-localized limit [18, 12]

$$E^{\text{DC}}_{\text{FLL}}\left[n_\sigma\right] = \frac{U}{2}\left(n_\uparrow + n_\downarrow\right)\left(n_\uparrow + n_\downarrow - 1\right) - \frac{J}{2}\sum_\sigma n_\sigma\left(n_\sigma - 1\right),$$

and the around mean-field form [19, 13]

$$E^{\text{DC}}_{\text{AMF}} = \left(\frac{U}{2}n_\uparrow n_\downarrow + \frac{n_\uparrow^2 + n_\downarrow^2}{2}\frac{2l}{(2l+1)}\left(U - J\right)\right).$$

Both expressions are spherically symmetrical, which is enough for most cases where the spherical term isn't canceled out.

1.3.2.2 Orbital polarization correction

One of the uses of LSDA+U is to describe local orbital magnetism in d and f orbitals, a task that LSDA without interactions performs relatively poorly [13]. In particular, the orbital polarization correction (OPC) approach is useful in cases where the Coulomb interaction is weak.

Under the OPC method, the electron-electron energy functional and double-counting term in Eq. (1.27) are grouped as a correction term to the LSDA energy functional, so that

$$E^{\text{LSDA+U}}\left[\rho, m, \hat{n}_{\gamma\gamma'}\right] = E^{\text{LSDA+U}}\left[\rho, m\right] + \Delta E^{\text{e-e}}\left[\hat{n}\right].$$

The correction term is separated into the spherical term (which includes the spherical double-counting terms) and the remaining, anisotropic term [20, 21], which consists of the orbital polarization correction E^{OPC} and the non-spherical double-counting term E^{NSDC}:

$$\Delta E^{\text{e-e}}\left[\hat{n}\right] = \frac{U - J}{2}\left(\text{Tr}\left[\hat{n}\right] - \text{Tr}\left[\hat{n}^2\right]\right) + E^{\text{OPC}}\left[\hat{n}\right] - E^{\text{NSDC}}\left[\hat{n}\right]. \tag{1.31}$$

In systems where $U = J$, the spherical term is canceled out, and the OPC becomes the leading term.

The energy contributions of the terms $E^{\text{OPC}}\left[\hat{n}\right]$ and $E^{\text{NSDC}}\left[\hat{n}\right]$ depend on the structure of the atom's valence shell.

1.3.3 Generalized Gradient Approximation

A popular alternative to LSDA is the generalized gradient approximation (GGA), which relaxes the local homogeneity demand, and assumes the local interactions

depend on both the local density and the local density's gradients $\nabla\rho_\sigma$. The most general GGA functional has the shape

$$E_{\mathrm{xc}}^{\mathrm{GGA}}[\rho] = \int \mathrm{d}^3\mathbf{r} f\left(\rho_\uparrow, \rho_\downarrow, \nabla\rho_\uparrow, \nabla\rho_\downarrow\right). \tag{1.32}$$

There are many possible choices of the f function, some analytical and some semi-empirical [22]. The various forms of GGA constitute compromises between computational expense and preservation of the properties of LDA's $\varepsilon_{\mathrm{xc}}(\rho)$, such as the shape of the potential curve, the scaling properties and the sum rule in Eq. (1.25). In this work, the GGA potentials used are those calculated using the Perdew-Burke-Ernzerhof (PBE) functional.

PBE uses two dimensionless density gradients, representing the length scales of the inhomogeneity and screening respectively:

$$s(\mathbf{r}) \equiv \frac{|\nabla\rho(\mathbf{r})|}{2k_F(\mathbf{r})\rho(\mathbf{r})},$$
$$t(\mathbf{r}) \equiv \frac{|\nabla\rho(\mathbf{r})|}{2k_s(\mathbf{r})\rho(\mathbf{r})}.$$

$k_F = (3\pi^2\rho)^{\frac{1}{3}}$ and $k_s = \sqrt{4k_F/\pi}$ are the Fermi wavelength and screening wavenumber respectively, under the Thomas-Fermi approximation. Other important parameters and functions are the local Wigner-Seitz radius $r_s = \left(\frac{3}{4\pi\rho}\right)^{\frac{1}{3}}$ and the relative spin polarization $\zeta \equiv \frac{m}{\rho}$.

The correlation functional of PBE is generated by adding to the correlation energy density of LSDA the term $H_{\mathrm{c}}(r_s, \zeta(\mathbf{r}), t(\mathbf{r}))$, so that

$$E_{\mathrm{c}}^{\mathrm{PBE}}[\rho_\uparrow, \rho_\downarrow] = \int \mathrm{d}^3\mathbf{r}\rho(\mathbf{r})\left(\varepsilon_{\mathrm{c}}^{\mathrm{LSDA}}(\rho(\mathbf{r}), \zeta(\mathbf{r})) + H_{\mathrm{c}}(r_s(\mathbf{r}), \zeta(\mathbf{r}), t(\mathbf{r}))\right).$$

The exchange functional of PBE is generated by multiplying the exchange energy density of LSDA by an enhancement factor F_{x}, which is a function of the screening:

$$E_{\mathrm{x}}^{\mathrm{PBE}}[\rho] = \int \mathrm{d}^3\mathbf{r}\rho(\mathbf{r})\,\varepsilon_{\mathrm{x}}^{\mathrm{LDA}}(\rho(\mathbf{r}))\,F_{\mathrm{x}}(s(\mathbf{r})).$$

The functions H_{c} and F_{x} are constructed to satisfy numerous conditions. H_{c} should converge to the second-order gradient approximation in the slowly-varying limit $t \to 0$, and make the correlation cancel out in the rapidly varying limit $t \to \infty$. F_{x} should give the exchange functional the same linear response to small density variations ($s \to 0$) as LSDA. The exchange functional should fulfill the Oliver-Perdew spin-scaling relation [23]

$$E_{\mathrm{x}}[\rho_\uparrow, \rho_\downarrow] = \frac{1}{2}\left(E_{\mathrm{x}}[2\rho_\uparrow] + E_{\mathrm{x}}[2\rho_\downarrow]\right)$$

and Lieb-Oxford bound [24]

$$E_{\mathrm{x}}\left[\rho_{\uparrow},\rho_{\downarrow}\right] \geq E_{\mathrm{xc}}\left[\rho_{\uparrow},\rho_{\downarrow}\right] \geq -1.679e^{2}\int \mathrm{d}\mathbf{r}\rho^{\frac{4}{3}}\left(\mathbf{r}\right).$$

Finally, the xc energy should also maintain a linear scaling under uniform scaling to the high density limit.

The expressions of H_{c} and F_{x} that fulfill those conditions can be seen in Ref. [22, 25] (or a more concise form in Ref. [7]). The expressions use several empiricaly-derived constants, whose values were revised in further variations on PBE [26, 27].

PBE allows for a considerably more accurate total energy calculation than LSDA, and a better description of magnetic moments in metals. Its main drawbacks compared to LSDA are the computational expense and the poor approximation of the asymptotic behavior $-1/r$ expected from electronic potentials.

1.4 Plane-wave basis

Numerical solution of the Kohn-Sham equations almost never involves direct solution of the differential equation Eq. (1.18). Instead, a basis set $\{|\varphi_m\rangle\}$ is selected to represent the system, and a wavefunction $\phi_n\left(\mathbf{r}\right)$ can be numerically represented with a discrete vector of expansion coefficients $\{c_{nm}\}$ in the form

$$\phi_n\left(\mathbf{r}\right) = \langle\mathbf{r}|\phi_n\rangle = \sum_m c_{nm}\varphi_m\left(\mathbf{r}\right). \tag{1.33}$$

The Kohn-Sham equation then take the form of the matrix eigenvalue equation

$$\left(\hat{H} - \epsilon_n\hat{S}\right)\mathbf{c}_n = 0, \tag{1.34}$$

where $\hat{H}$ is the Kohn-Sham Hamiltonian in the basis $\{|\varphi_m\rangle\}$ and $\hat{S}$ is the overlap matrix $S_{mm'} \equiv \langle\varphi_m|\varphi_{m'}\rangle$. The overlap matrix is diagonal in the case of an orthogonal basis set and an identity matrix in the case of an orthonormal basis set.

The systems that concern our work are crystals, and those are described by a periodic Hamiltonian. According to Bloch's theorem, the eigenstates of such a Hamiltonian are plane-waves multiplied by functions with the same periodicity as the crystal [28]. The periodic factor of the wavefunction can undergo a Fourier transform to the reciprocal space and become a linear combination of planewaves with a wavevector $\mathbf{g}$ [10]. The Kohn-Sham eigenstates are therefore $|\phi_{n\mathbf{k}}\rangle$, their projection on the real space being

$$\phi_{n\mathbf{k}}\left(\mathbf{r}\right) = \langle\mathbf{r}|\phi_{n\mathbf{k}}\rangle = \frac{1}{\sqrt{\Omega_G}}\sum_{\mathbf{g}} c_{\mathbf{g}n\mathbf{k}}e^{i(\mathbf{g}+\mathbf{k})\cdot\mathbf{r}}, \tag{1.35}$$

with Ω_G as the reciprocal volume of the $\mathbf{g}$ vector range. The $\mathbf{g}$ vectors are limited to the first Brillouin zone, because the periodicity of the crystal makes it possible to map every vector $\mathbf{k}$ to a vector inside the Brillouin zone. In practice,

the expansion coefficients usually decrease with the size of $\mathbf{g}$, so their range can be truncated by a ceiling value $|\mathbf{g}| < g_{\max}$.

The eigenstates form a band structure in the Brillouin zone, with $\epsilon_{n\mathbf{k}}$ as the energy of the n-th band at point $\mathbf{k}$. The basis set is enumerated by the vectors $\mathbf{g}$. The secular equations Eq. (1.34) are performed at each $\mathbf{k}$-point independently:

$$\sum_{\mathbf{g}'} \left(H^{\mathbf{k}}_{\mathbf{g}\mathbf{g}'} - \epsilon_n S^{\mathbf{k}}_{\mathbf{g}\mathbf{g}'} \right) c_{\mathbf{g}'n\mathbf{k}} = 0, \tag{1.36}$$

with $H^{\mathbf{k}}_{\mathbf{g}\mathbf{g}'} = \langle \mathbf{k}+\mathbf{g}| \hat{H} |\mathbf{k}+\mathbf{g}'\rangle$ and $S^{\mathbf{k}}_{\mathbf{g}\mathbf{g}'} = \langle \mathbf{k}+\mathbf{g}|\mathbf{k}+\mathbf{g}'\rangle$.

1.4.1 Partial occupancies

The first term in the Kohn-Sham energy Eq. (1.21) is the integral over all energy bands below Fermi energy ϵ_F. In the plane-wave basis, it takes the shape

$$E = \sum_n \frac{1}{\Omega_{\mathrm{BZ}}} \int d\mathbf{k} \epsilon_{n\mathbf{k}} \Theta \left(\epsilon_{n\mathbf{k}} - \epsilon_F \right), \tag{1.37}$$

where Ω_{BZ} is the reciprocal volume of the Brillouin zone and ϵ_F is defined to preserve the number of electrons:

$$N = \sum_n \frac{1}{\Omega_{\mathrm{BZ}}} \int d\mathbf{k} \Theta \left(\epsilon_{n\mathbf{k}} - \epsilon_F \right). \tag{1.38}$$

Fully-occupied bands are fully integrated over, while partially-occupied bands are integrated only over the parts below ϵ_F.

The total energy is computed numerically in a discretized $\mathbf{k}$ space [29, 30, 31]:

$$E \simeq \sum_{n,\mathbf{k}} w_{\mathbf{k}} \epsilon_{n\mathbf{k}} \Theta \left(\epsilon_{n\mathbf{k}} - \epsilon_F \right), \tag{1.39}$$

where $w_{\mathbf{k}}$are the weighing factors of each k-point, which should be normalized:

$$\sum_{\mathbf{k}} w_{\mathbf{k}} = 1 \tag{1.40}$$

The more k-points are included, the closer will the calculated energy be to the accurate one. However, the convergence is very slow, because the discretization loses information about the limits of integration over partially occupied bands. It can be boosted by replacing the step-function in Eq. (1.39) by a smoother function, such as the Fermi-Dirac distribution function

$$f\left(\epsilon\right) = \frac{1}{e^{\frac{\epsilon-\epsilon_F}{\sigma}} + 1}, \tag{1.41}$$

or the Gaussian

$$f(\epsilon) = \frac{1 - \operatorname{erf}\left(\frac{\epsilon - \epsilon_F}{\sigma}\right)}{2}. \tag{1.42}$$

Smearing out the function makes the sum more responsive to variations in the Fermi energy, thereby reducing its error. The total energy is then

$$E = \sum_{n,\mathbf{k}} w_{\mathbf{k}} \epsilon_{n\mathbf{k}} f(\epsilon_{n\mathbf{k}}), \tag{1.43}$$

and the electron density in Eq. (1.19) is then converted to

$$\rho_0(\mathbf{r}) = \sum_{n,\mathbf{k}} w_{\mathbf{k}} f(\epsilon_{n\mathbf{k}}) |\phi_{n\mathbf{k}}(\mathbf{r})|^2. \tag{1.44}$$

As can be seen, the electron density can be described numerically in terms of the discrete values of $w_{\mathbf{k}}$, $\epsilon_{n\mathbf{k}}$ and $|\phi_{n\mathbf{k}}\rangle$.

The use of Fermi-Dirac distribution function gives a physical interpretation to the smearing - we work in the canonical ensemble, and $\sigma = \frac{1}{\beta} \equiv k_B T$. With a nonzero temperature, E is no longer the minimal energy — under the thermodynamic interpretation, the system gained heat. The true minimal energy is therefore the free energy

$$F = E - \frac{1}{\beta} \sum_{n,\mathbf{k}} w_{\mathbf{k}} S(f(\epsilon_{n\mathbf{k}})), \tag{1.45}$$

where the entropy per state is

$$S(f(\epsilon_{n\mathbf{k}})) = f(\epsilon_{n\mathbf{k}}) \ln f(\epsilon_{n\mathbf{k}}) - (1 - f(\epsilon_{n\mathbf{k}})) \ln(1 - f(\epsilon_{n\mathbf{k}})). \tag{1.46}$$

Fermi-Dirac smearing is rarely used in practice, due to the poor compromise between convergence speed and accuracy of the converged state. In our work, we use Gaussian smearing for ionic relaxation, and the tetrahedron method with Blöchl corrections [32] for calculating the total energy, DOS and magnetic moments of pre-relaxed structures.

1.5 Augmented plane-wave methods

1.5.1 Augmented plane-wave method

The augmented plane-wave method (APW) is an alternative to the plane-wave basis, commonly used for transition metals and their compounds [10]. APW generally retains the size of the basis set, including all electrons in the calculation, but reduces the incidence of high-order waves. It divides space into different regions with different basis expansions - plane waves in the interstitial region, and atomic orbitals in spheres centered around nuclei (dubbed “muffin-tins”,

due to the shape of their 2D analogue) [10]. The effective potential $V_{\text{eff}}(\mathbf{r})$ is approximated as being constant in the interstitial region and radially symmetrical inside the muffin-tin region:

$$V_{\text{eff}}(\mathbf{r}) \approx \begin{cases} 0 & \mathbf{r} \in \text{I} \\ V_{\text{MT}}(r) & \mathbf{r} \in \text{MT} \end{cases}$$

The Kohn-Sham eigenstates are then (the n and $\mathbf{k}$ indices for $c_{\mathbf{g}}$ have been ignored for convenience)

$$\phi_{n\mathbf{k}}(\mathbf{r}) = \begin{cases} \frac{1}{\sqrt{\Omega_G}} \sum_{\mathbf{g}} c_{\mathbf{g}} e^{i(\mathbf{g}+\mathbf{k})\cdot\mathbf{r}} & \mathbf{r} \in \text{I} \\ \sum_{lm} A_{lm} u_l(r) Y_{lm}(\theta, \phi) & \mathbf{r} \in \text{MT} \end{cases}. \tag{1.47}$$

Inside the muffin-tin, the coordinates are spherical. $Y_{lm}(\theta, \phi)$ are spherical harmonics which depend on the $\mathbf{r}$ vector's azimuth θ and altitude ϕ. $u_l(r)$ is the radial component, a function of the distance from the nucleus, and is derived from the radial Schrödinger's equation

$$\left(-\frac{\mathrm{d}^2}{\mathrm{d}r^2} + \frac{l(l+1)}{r^2} + V_{\text{MT}}(r) - E_l\right) r u_l(r) = 0, \tag{1.48}$$

where $V_{\text{MT}}(r)$ is a radial muffin-tin potential and E_l is the energy eigenvalue and a free parameter. The continuity of the wavefunction in the boundary between the muffin tin and the interstitial area is maintained by a constraint imposed on the spherical expansion coefficients A_{lm}:

$$A_{lm} = \frac{4\pi i^l}{\sqrt{\Omega_G} u_l(R)} \sum_{\mathbf{g}} c_{\mathbf{g}} j_l(|\mathbf{k}+\mathbf{g}| \cdot R) Y_{lm}^{\star}(\mathbf{k}+\mathbf{g}), \tag{1.49}$$

where R is the radius of the muffin tin and j_l are the spherical Bessel functions. The coefficients A_{lm} are uniquely defined from the planar coefficients $c_{\mathbf{g}n\mathbf{k}}$ and the energies E_l, which are used as the variational parameters when solving the Kohn-Sham equations.

One of the main difficulties of the APW method is that the exact solution requires the eigenvalues of Eq. (1.48) to be equal to the band energies. If the calculation is performed by selecting constant values for E_l, solving Eq. (1.48) and getting a basis which is then used to solve Eq. (1.34), the eigenvalues ϵ_n may be different from energies E_l. On the other hand, setting E_l to be equal to the band energies would turn the secular equation from a simple eigenvalue problem to a much more computationally complex problem of finding the roots of a polynomial.

Another possible problem is the asymptote problem — if $u_l(R)$ is small or equal to zero, then unless the coefficients A_{lm} are very large to infinite (as can be deduced from the presence of $u_l(R)$ in the denominator of the coefficients in Eq. (1.49)), the function $\phi(\mathbf{r})$ asymptotically approaches zero from within the muffin-tin zone, making the muffin-tin effectively decoupled from the interstitial zone.

1.5.2 Linearized augmented plane-wave method

The most popular solution to the problems of APW mentioned above is the linearized augmented plane-wave method (LAPW). It extends the APW method by converting the radial component u_l into a linear combination of itself and its own derivative with respect to energy, $\dot{u}_l \equiv \frac{\mathrm{d}u_l}{\mathrm{d}\epsilon}$. The derivative of u_l must be orthogonal to it, so that $\langle u_l | \dot{u}_l \rangle = 0$. The wavefunction becomes

$$\phi_{n\mathbf{k}}(\mathbf{r}) = \begin{cases} \frac{1}{\sqrt{\Omega_G}} \sum_{\mathbf{g}} c_{\mathbf{g}} e^{i(\mathbf{g}+\mathbf{k})\cdot\mathbf{r}} & \mathbf{r} \in \mathrm{I} \\ \sum_{lm} \left(A_{lm} u_l(r) + B_{lm} \dot{u}_l(r) \right) Y_{lm}(\theta, \phi) & \mathbf{r} \in \mathrm{MT} \end{cases}. \tag{1.50}$$

The energy derivative of the radial component satisfies the equation

$$\left(-\frac{\mathrm{d}^2}{\mathrm{d}r^2} + \frac{l(l+1)}{r^2} + V_{\mathrm{MT}}(r) - E_l \right) r\dot{u}_l = r u_l. \tag{1.51}$$

The new expansion coefficients B_{lm} give the basis additional variational freedom — if there is a discrepancy between the band energy ϵ and the muffin-tin energy E_l, the coefficients can be chosen to make the linear combination $A_{lm} u_l(r) + B_{lm} \dot{u}_l(r)$ into an effective radial component with an energy closer to ϵ. The LAPW has an error on the order of $(\epsilon - E_l)^2$ in the wavefunction and on the order of $(\epsilon - E_l)^4$ in the band energy. This enables the calculation to converge to a solution much more quickly.

The variational freedom allows for greater flexibility in treating non-spherical potentials inside the sphere. Additionally, LAPW resolves the asymptote problem at the muffin-tin boundary — even if $u_l(r)$ approaches zero at the muffin-tin boundary, $\dot{u}_l(r)$ generally doesn't, and the decoupling of the two zones is prevented.

1.5.3 Full-potential LAPW

LAPW outperforms APW in reduced-symmetry solids, such as *bcc* crystals. However, the muffin-tin approximation of the potential makes it less than optimal for calculating the local charge density of a specific atom. The full-potential LAPW method (FLAPW), introduced by Wimmer *et al.* in 1981 [33, 34], uses the exact potential in both the muffin tin spheres and the interstitial area. The core electrons are treated relativistically, while the valence electrons are treated semi-relativistically [34].

In each zone, the potential is expressed in the same basis as the charge density - plane waves in the interstitial area and multipoles in the muffin-tin sphere:

$$V_{\mathrm{eff}}(\mathbf{r}) = \begin{cases} \sum_{\mathbf{G}} \tilde{V}_{\mathbf{G}} e^{i\mathbf{G}\mathbf{r}} & \mathbf{r} \in \mathrm{I} \\ \sum_{lm} V_l(\mathbf{r}) Y_{lm}(\theta, \phi) & \mathbf{r} \in \mathrm{MT} \end{cases} \tag{1.52}$$

The full potential is derived from the charge density through a process detailed in Ref. [33, 35], intended to maintain the potential's smoothness at the muffin-tin radius. The charge density inside the muffin-tin is used to generate a smooth pseudo-charge density, which has the same multipoles on the boundary as the

original charge but a more rapidly converging Fourier (plane-wave) components. The interstitial potential can then be calculated using effective pseudo-charge density, since it's only influenced by the charge density's multipoles. The muffin-tin potential is then calculated from interstitial potential and original charge density.

1.6 Pseudo-wavefunction methods

The plane-wave basis is efficient for describing free conduction electrons, since those are generally found at a large distance from the nuclei, where the potentials of many nuclei affect the electrons in aggregate. For core and valence electrons, however, the potential of their nucleus is dominant, and their natural basis is that of atomic orbitals. Attempting to describe them using planewaves would create a Kohn-Sham wavefunction with many high-order $\mathbf{g}$ components, which would be costly and inaccurate.

This situation can be remedied by using pseudo-wavefunction methods, in which the basis of wavefunctions $|\phi_n\rangle$ is substituted by the basis of pseudo-wavefunctions $\left|\tilde{\phi}_n\right\rangle$ (in PAW texts the transformation is sometimes called "pseudization" [36]). The pseudo-wavefunctions are made to be equal to the original wavefunctions outside of a defined core radius while being much smoother inside the core region.

The pseudo-wavefunction method utilized in this work is the projector-augmented wave (PAW) method, which combines techniques used for ultrasoft pseudo-potentials and LAPW [37, 36]. The details of PAW will be preceded by an overview of pseudo-potentials and Vanderblit's ultrasoft pseudo-potentials method.

1.6.1 Pseudo-potentials

The first method which utilized pseudo-wavefunctions is the pseudopotential method, which involves replacing each atom's core (the nucleus and core electrons) with an effective potential $\tilde{V}(r)$ whose ground state matches the real ground state outside of the core radius r_c [10]. This treats the core electrons as static and takes them out of the electronic density. The pseudo-wavefunction $\tilde{\phi}_n$ is then the solution of the Schrödinger equation for the valence shell with azimuthal quantum number l:

$$\left(-\frac{\mathrm{d}^2}{\mathrm{d}r^2}+\frac{l\left(l+1\right)}{r^2}+\tilde{V}\left(r\right)-E_n\right)\tilde{\phi}_n\left(r\right)=0,$$

while also being definitionally equal to ϕ_n for $r < r_c$.

When using the pseudopotential method, the crystal's potential is assembled in the unit cell from a library of pseudo-potentials, pre-calculated in isolation or inside a crystal. For the library pseudo-potentials to be useful in different systems, they need to be transferable — a pseudopotential calculated in one atomic configuration can be accurately transferred to another one. This condition is maintained by requiring the logarithmic derivative of the real wavefunctions and pseudo-wavefunctions to be equal at the core radius [10]:

$$\frac{1}{\tilde{\phi}_n(r_c)}\frac{\mathrm{d}\tilde{\phi}_n(r_c)}{\mathrm{d}r} = \frac{1}{\phi_n(r_c)}\frac{\mathrm{d}\phi_n(r_c)}{\mathrm{d}r}.$$

Other desirable properties are the accuracy of the pseudo-wavefunction's charge density, and softness — the pseudo-wavefunction's planewave expansion should converge as quickly as possible. A popular approach to a compromise between these features is to require pseudo-wavefunctions to have the same norm inside the core region as the exact wavefunction [38]. The most popular norm-conserving pseudopotential generation method is the Bachelet-Hamann-Schlüter process [39]. It works by adding to the generation algorithm three additional steps — derivation of the pseudo-wavefunction from the pseudopotential, normalization of the pseudo-wavefunction, and the derivation of a new pseudopotential via the inversion of the Schrödinger's equation. The compromise between softness and transferability is maintained by selecting the core radius - a larger core allows for a softer wavefunction, but worsens the transferability [36].

1.6.2 Ultrasoft pseudo-potentials

The ultrasoft pseudopotential approach abandons the requirement for norm conservation inside the core sphere, thereby allowing the pseudo-wavefunctions to be much smoother [36, 40]. Without norm conservation, a difference is formed between the core charges of the all-electron wavefunctions $|\phi_n\rangle$ and pseudo-wavefunctions $\left|\tilde{\phi}_n\right\rangle$, which is compensated using the augmentation term[3]

$$Q_{mn} = \langle\phi_m|\phi_n\rangle - \langle\tilde{\phi}_m|\tilde{\phi}_n\rangle. \tag{1.53}$$

The augmentation charges are expanded inside the core radius using the projectors $|p_n\rangle$, fixed functions which form a reciprocal basis with $\left|\tilde{\phi}_n\right\rangle$ inside the core, so that

$$\langle p_m|\tilde{\phi}_n\rangle = \begin{cases}\delta_{mn} & r \le r_c \\ 0 & r > r_c\end{cases}.$$

The charge density is then expressed as a sum of the pseudo-wavefunction charge density and the augmentation charges [10]:

$$\rho(\mathbf{r}) = \sum_n \left(\tilde{\phi}_n^\star(\mathbf{r})\,\tilde{\phi}_n(\mathbf{r}) + \sum_{mm'} Q_{mm'}(\mathbf{r})\,\langle\tilde{\phi}_n|p_m\rangle\langle p_{m'}|\tilde{\phi}_n\rangle\right). \tag{1.54}$$

The added augmentation charges give the overlap matrix $\mathbf{S}$ in the secular equation Eq. (1.34) the form

$$\mathbf{S} = \mathbf{I} + \sum_{mn} Q_{mn}\,|p_m\rangle\,\langle p_n|\,. \tag{1.55}$$

[3]State products like $\langle\phi_m|\phi_n\rangle$ are generally performed not over all space but inside a radius that encompasses r_c [40].

The smoothness of ultrasoft pseudo-potentials allows for a much lower energy cutoff, which improves the computational cost. They can also have much larger core radii, as much as half of the distance to the nearest neighbor. They are particularly useful for $3d$-metals. Their disadvantage is the difficulty of their construction, since they require several cutoff radii to be adjusted [36].

1.6.3 Projector-augmented wave method

The PAW method is an all-electron method that usually implements frozen cores — the core states are represented explicitly, but are calculated in advance for isolated atoms. The method borrows from LAPW the notion that the interstitial and atomic regions have different natural basis sets. The Kohn-Sham state $|\phi_{n\mathbf{k}}\rangle$ and the pseudo-wavefunction $\left|\tilde{\phi}_{n\mathbf{k}}\right\rangle$ are both expressed in the basis of plane waves. Inside a core radius, $|\phi_{n\mathbf{k}}\rangle$ is expanded by the all-electron partial waves $|\varphi_{\mathbf{R}lm}\rangle$, which are expressed in the atomic orbital basis, and the pseudo-wavefunction is expanded by the pseudo partial waves $|\tilde{\varphi}_{\mathbf{R}lm}\rangle$. The all-electron and pseudo partial waves are constructed so that the expansion coefficients are the same for the exact and pseudo-wavefunction:

$$\begin{aligned} |\phi_{n\mathbf{k}}\rangle &= \sum_{\mathbf{R}lm} c_{\mathbf{R}lm} \, |\varphi_{\mathbf{R}lm}\rangle \,, \\ \left|\tilde{\phi}_{n\mathbf{k}}\right\rangle &= \sum_{\mathbf{R}lm} c_{\mathbf{R}lm} \, |\tilde{\varphi}_{\mathbf{R}lm}\rangle \,. \end{aligned} \tag{1.56}$$

The coefficients in Eq. (1.56) are expressed as the projection of the pseudo-wavefunction on the projectors $|p_{\mathbf{R}n}\rangle$, similar to the ones introduced in Sec. 1.6.2:

$$c_{\mathbf{R}lm} = \langle p_{\mathbf{R}lm} | \phi \rangle. \tag{1.57}$$

The Kohn-Sham states can then be described in the form

$$|\phi_{n\mathbf{k}}\rangle = \left|\tilde{\phi}_{n\mathbf{k}}\right\rangle + \sum_{\mathbf{R}lm} \left(|\varphi_{\mathbf{R}lm}\rangle - |\tilde{\varphi}_{\mathbf{R}lm}\rangle \right) \langle p_{\mathbf{R}lm} | \tilde{\phi}_{n\mathbf{k}} \rangle.$$

The charge density then has an analogous shape to Eq. (1.54):

$$\begin{aligned} \rho\left(\mathbf{r}\right) &= \sum_{n\mathbf{k}} \langle \phi_{n\mathbf{k}} | \mathbf{r} \rangle \langle \mathbf{r} | \phi_{n\mathbf{k}} \rangle \\ &= \sum_{n\mathbf{k}} \left(\tilde{\phi}^{\star}_{n\mathbf{k}}\left(\mathbf{r}\right) \tilde{\phi}_{n\mathbf{k}}\left(\mathbf{r}\right) + \sum_{\mathbf{R}lml'm'} Q_{\mathbf{R}lml'm'}\left(\mathbf{r}\right) \langle \tilde{\phi}_{n\mathbf{k}} | p_{\mathbf{R}lm} \rangle \langle p_{\mathbf{R}'l'm'} | \tilde{\phi}_{n\mathbf{k}} \rangle \right). \end{aligned}$$

Like the projector functions, the augmentation matrix in PAW is in the basis of atomic orbitals:

$$Q_{\mathbf{R}lml'm'} = \langle \varphi_{\mathbf{R}lm} | \varphi_{\mathbf{R}l'm'} \rangle - \langle \tilde{\varphi}_{\mathbf{R}lm} | \tilde{\varphi}_{\mathbf{R}l'm'} \rangle \tag{1.58}$$

PAW potentials generally have smaller core radii than ultrasoft pseudo-potentials, limiting the approximation to a smaller area. This makes the calculation more accurate, but also requires higher energy cutoffs and larger basis sets, which makes computation more expensive [37]. The smaller core radius, as well as the all-electron character of the method, makes PAW particularly useful for core-sensitive properties such as magnetic moments.

1.7 Summary

In this chapter, the general DFT formalism was derived from first principles for the non-relativistic, non-interacting, spinless case. This was followed by descriptions of DFT techniques relevant to our work — the choice of basis, the choice of xc energy approximation and the addition of spin-dependence and electron-electron interaction to the formalism.

The DFT process is shown in Fig. 1.1. The names of several methods appear to the right of the step to which they apply. Self consistency between the electron density and the energy functional is generated by repeatedly calculating one from the other until the system's energy stabilizes. After each iteration, the newly calculated density is mixed with the existing one using the parameter α in order to have a smoother descent.

Once the DFT process converges to a solution, it's possible to calculate the local density of states (DOS) — the projection of the DFT eigenstates on the local spin-orbitals, integrated over the momenta so that it's a function of only the local spin-orbital and energy:

$$\rho_{m\sigma}(\epsilon) = \frac{1}{\Omega_{BZ}} \int_{\mathrm{BZ}} \mathrm{d}\mathbf{k} \delta(\epsilon - \epsilon_{n\mathbf{k}}) \left| \langle n\mathbf{k} | m\sigma \rangle \right|^2, \tag{1.59}$$

with Ω_{BZ} as the Brillouin zone volume. The local DOS employs the single-site approximation, as it averages away all of the electronic structure outside of the atom to which it is applied.

In the context of a DFT+ED calculation, the goal of the DFT process is to generate the impurity's local Green's function. The Green's function (also known as the correlation function of creation and annihilation operators) contains information about the energy spectrum and dynamics of a many-body system. For the non-interacting case, it is expressed in the complex frequency space z as

$$G^{\mathrm{DFT}}_{mm'\sigma\sigma'}(z) = \frac{1}{\Omega_{\mathrm{BZ}}} \int_{\mathrm{BZ}} \mathrm{d}\mathbf{k} \langle m\sigma | \left(z + \epsilon_F - \hat{H}^{\mathrm{DFT}}(\mathbf{k}) \right)^{-1} | m'\sigma' \rangle . \tag{1.60}$$

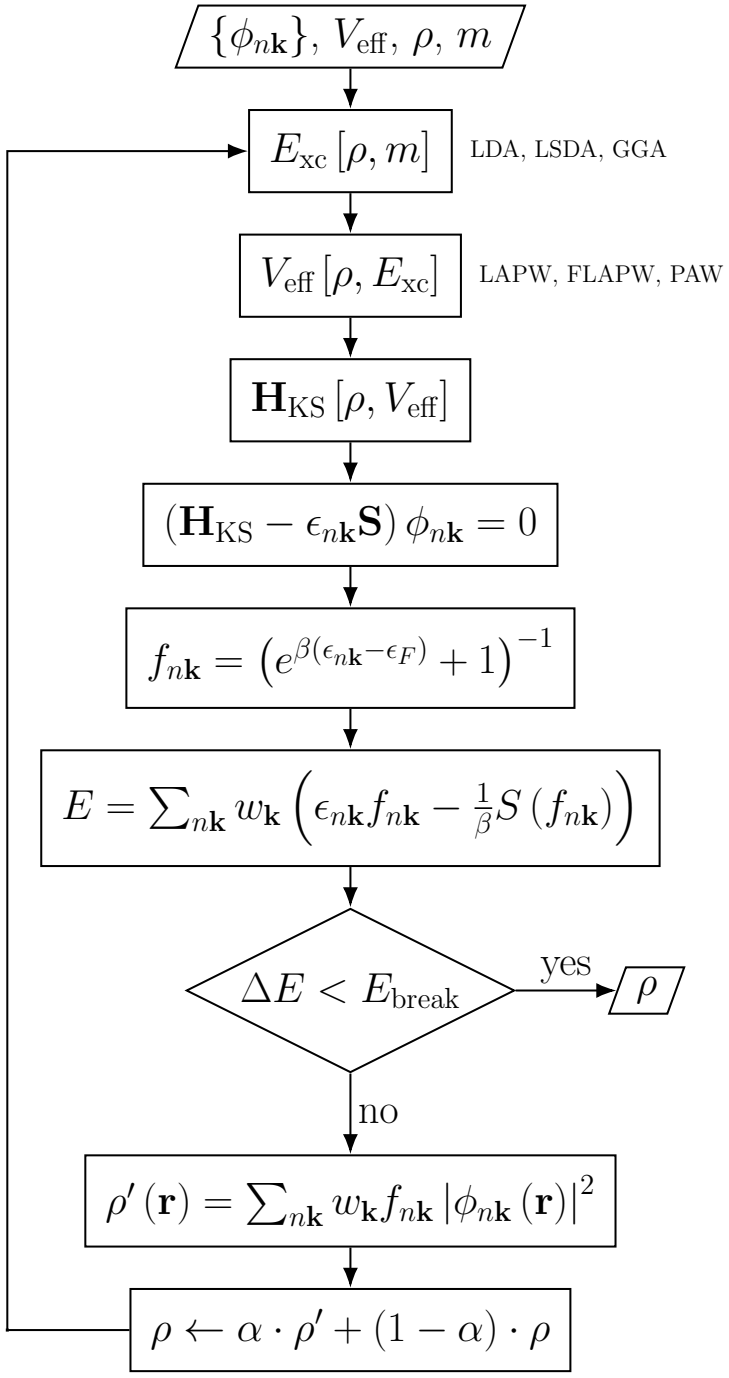

Figure 1.1: Flowchart of a DFT algorithm.

Chapter 2

Methods of many-body physics for realistic materials

In the previous chapter, LSDA+U was proposed as a method for extending the DFT formalism to materials with strong interactions. Though LSDA+U is an effective method for bulk materials, it is not particularly well-suited for describing the orbital characteristics of magnetic impurities explicitly.

In this chapter another approach will be presented, which employs the Anderson impurity model, introduced by Anderson in 1961 [41] in order to qualitatively describe the behavior of magnetic impurities embedded in metals. A real material can be modeled by using the impurity's local DOS found by DFT to construct the Anderson model's bath and local Hamiltonian. This is done by requiring that under the one-electron approximation, the model's properties will match those of the DFT output.

Two of the methods of solving AIM are continuous-time quantum Monte Carlo (CT-QMC) and exact diagonalization. In quantum Monte Carlo, measurement of observables like the Green's function is performed by randomly sampling the state space and summing over the observables in each state. Since we have not used this method in practice, it is only presented here for reference.

Exact diagonalization is applied to AIM by discretizing discretizing each impurity's bath to a small number of energy levels and then diagonalizing the resulting Hamiltonian. The construction of the discrete model is done with the principle that its behavior should be as close as possible to the continuous model. This is implemented by fitting the discrete model's parameters so that the hybridization functions of both models are as close as possible, where the closeness is defined by a residual function. Observables are measured in the grand-canonical ensemble using matrix operations. The computational methods involved in the procedure are detailed in this chapter.

2.1 Anderson impurity model

The AIM, introduced by Anderson in 1961 [41], describes an impurity atom embedded in a material or adhesed to it using second quantization formalism. The conduction electron sites are numbered with a single index k (not to be confused with the plane-wave wavevector $\mathbf{k}$), and the hybridization between them and the

impurity is limited to one-electron hoppings. The system's Hamiltonian is

$$\hat{H}_{\text{imp}} = \hat{H}_0 + \hat{H}_{\text{int}} + \hat{H}_{\text{bath}} + \hat{H}_{\text{hyb}}. \tag{2.1}$$

The terms in Eq. (2.1) represent, in order, the energy of impurity orbitals, the spherically symmetric Coulomb interaction of the impurity electrons, the energy of bath orbitals, and the hybridization between the bath and the impurity electrons. The operators are

$$\hat{H}_0 = \sum_{m\sigma} \epsilon_m n^d_{m\sigma}, \tag{2.2}$$

$$\hat{H}_{\text{int}} = \frac{1}{2} \sum_{mm'm''m'''\sigma\sigma'} U_{mm'm''m'''} d^\dagger_{m\sigma} d^\dagger_{m'\sigma'} d_{m''\sigma'} d_{m'''\sigma}, \tag{2.3}$$

$$\hat{H}_{\text{bath}} = \sum_{k\sigma} \epsilon_k n^b_{k\sigma}, \tag{2.4}$$

$$\hat{H}_{\text{hyb}} = \sum_{mk\sigma} \left(V_{mk} d^\dagger_{m\sigma} b_{k\sigma} + \text{h.c.} \right). \tag{2.5}$$

Where $d^\dagger_{m\sigma}$ creates an impurity electron in orbital m and spin σ[1], $b^\dagger_{k\sigma}$ creates an impurity electron with energy ϵ_k and spin σ, and $n^d_{m\sigma} = d^\dagger_{m\sigma} d_{m\sigma}$ and $n^b_{k\sigma} = b^\dagger_{k\sigma} b_{k\sigma}$ are the number operators for the impurity and bath respectively. The bath is at its lowest energy state when all and only negative energy levels are occupied, giving it an effective Fermi energy of 0. For now, the local Hamiltonian is assumed to be diagonal.

Following the formalism of Gunnarsson *et al.* [42, 43], the bath will be transformed into a basis that is diagonal in the impurity's spin-orbital basis, so that each state is coupled to one of the impurity's orbitals. The basis' vectors are

$$|b(\epsilon, m, \sigma)\rangle = \frac{1}{V_m(\epsilon)} \sum_k V_{mk} \delta(\epsilon - \epsilon_k) |k\sigma\rangle, \tag{2.6}$$

where

$$[V_m(\epsilon)]^2 = \sum_k V^2_{mk} \delta(\epsilon - \epsilon_k). \tag{2.7}$$

This transformation introduces a continuous energy spectrum to the formalism. Though the expressions in Eq. (2.6) and Eq. (2.7) are still effectively discrete, it is now possible to treat them as effectively continuous in the limit of very numerous and dense bath states by converting every Dirac delta function to a very narrow peak.

The Hamiltonian after the transformation is

$$\begin{aligned}\hat{H}_{\text{imp}} = &\sum_{m\sigma} \epsilon_m n^d_{m\sigma} + \sum_{mk\sigma} \int \mathrm{d}\epsilon n^b_{m\sigma}(\epsilon) + \sum_{m\sigma} \int \mathrm{d}\epsilon \left(V_m(\epsilon) d^\dagger_{m\sigma} b_{m\sigma}(\epsilon) + \text{h.c.} \right) \\ &+ \frac{1}{2} \sum_{mm'm''m'''\sigma\sigma'} U_{mm'm''m'''} d^\dagger_{m\sigma} d^\dagger_{m'\sigma'} d_{m''\sigma'} d_{m'''\sigma},\end{aligned} \tag{2.8}$$

where $n^b_{m\sigma}(\epsilon) = b^\dagger_{m\sigma}(\epsilon) b_{m\sigma}(\epsilon)$ is the continuous occupation of the bath coupled to spin-orbital $m\sigma$.

[1] It is denoted with the character d because we primarily work with d-shell electrons.

2.2 Density of states and many-body functions

We facilitate the mapping from DFT to AIM through the DFT local density of states in Eq. (1.59). The diagonal part of the non-interacting, one-particle local Green's function in Eq. (1.60) can be rewritten as a Hilbert transform of the DOS:

$$G_{m\sigma}^{\mathrm{DFT}}(\epsilon - i\eta) = \int_{-\infty}^{\infty} \mathrm{d}\epsilon' \frac{\rho_{m\sigma}(\epsilon')}{\epsilon - \epsilon' - i\eta}, \tag{2.9}$$

where η is an imaginary additive that prevents a singularity for $\epsilon = \epsilon'$ and provides a way to derive the DOS analytically from the Green's function:

$$\lim_{\eta\to 0}\left(\mathrm{Im}\left[G_{m\sigma}(\epsilon - i\eta)\right]\right) = \lim_{\eta\to 0}\left(\int_{-\infty}^{\infty} \mathrm{d}\epsilon' \rho_{m\sigma}(\epsilon') \frac{\eta}{(\epsilon - \epsilon')^2 + \eta^2}\right) = \pi\rho_{m\sigma}(\epsilon), \tag{2.10}$$

$$\rho_{m\sigma}(\epsilon) = \lim_{\eta\to 0}\left(-\frac{1}{\pi}\mathrm{Im}\left[G_{m\sigma}(\epsilon - i\eta)\right]\right). \tag{2.11}$$

The non-interacting local Green's function of the AIM is the resolvent of the interaction-free model, measured in the local spin-orbitals:

$$G_{m\sigma}^{\mathrm{AIM}}(z) = \langle m\sigma| \left(z - \hat{H}_0 - \hat{H}_{\mathrm{bath}} - \hat{H}_{\mathrm{hyb}}\right)^{-1} |m\sigma\rangle \tag{2.12}$$

In order to work with a Hamiltonian matrix limited to the local states, the non-interacting Hamiltonian $\hat{H}_0 + \hat{H}_{\mathrm{bath}} + \hat{H}_{\mathrm{hyb}}$ will be downfolded to the local basis. The resulting form of the diagonal Green's function is

$$G_{m\sigma}^{\mathrm{AIM}}(z) = \langle m\sigma| \left(z - \hat{H}_0 - \hat{\Delta}(z)\right)^{-1} |m\sigma\rangle = \frac{1}{z - \epsilon_m - \Delta_{m\sigma}(z)}. \tag{2.13}$$

$\hat{\Delta}(z)$ is the hybridization function, which is expressed as a matrix in the local basis for every given z, and $\Delta_{m\sigma}(z)$ are its diagonal elements. It represents the shift in impurity energy levels induced by the bath. It can be derived for a discrete model by expressing the entire Hamiltonian as a block matrix, calculating Eq. (2.12) explicitly and bringing it to the form of Eq. (2.13). In the case of a continuous bath, the hybridization function is

$$\hat{\Delta}(z) = \hat{H}_{\mathrm{hyb}}^{\dagger}\left(z - \hat{H}_{\mathrm{bath}}\right)^{-1}\hat{H}_{\mathrm{hyb}} = \int \mathrm{d}\epsilon' \frac{\left[V_{m\sigma}(\epsilon')\right]^2}{z - \epsilon'}. \tag{2.14}$$

The self-consistency between DFT and AIM is manifested by equating the Green's functions in Eq. (2.9) and Eq. (2.13):

$$G_{m\sigma}^{\mathrm{DFT}}(z) = G_{m\sigma}^{\mathrm{AIM}}(z) \tag{2.15}$$

This equation allows to construct an effective hybridization function that corresponds to a given DOS, by substituting $G_{m\sigma}^{\mathrm{DFT}}(z)$ into Eq. (2.13):

$$\Delta_{m\sigma}(z) = z - \epsilon_m - \left[G_{m\sigma}^{\mathrm{DFT}}(z)\right]^{-1} \tag{2.16}$$

We expect the hybridization function to approach 0 when the absolute value of z is very large. The conditions that this expectation imposes on the DOS can be found by following Ref. [44] and expanding the Green's functions in the limit $|z| \to \infty$ using the geometric series

$$\frac{1}{z-\epsilon} = \sum_{n=0}^{\infty} \frac{\epsilon^n}{z^{n+1}}. \tag{2.17}$$

For the DFT-derived Green's function, the expansion is.

$$G_{m\sigma}^{\mathrm{DFT}}(z) = \sum_{n=0}^{\infty} \frac{1}{z^{n+1}} \int_{-\infty}^{\infty} \mathrm{d}\epsilon \cdot \epsilon^n \rho_{m\sigma}(\epsilon). \tag{2.18}$$

For the AIM Green's function, it is

$$G_{m\sigma}^{\mathrm{AIM}}(z) = \sum_{n=0}^{\infty} \frac{1}{z^{n+1}} \left(\epsilon_m + \Delta_{m\sigma}(z)\right)^n. \tag{2.19}$$

In order to get a full expansion of $G_{m\sigma}^{\mathrm{AIM}}(z)$, we need to expand the hybridization function as well, using the explicit expression in terms of the AIM parameters as appearing in Eq. (2.49). Nevertheless, since the first term of the hybridization function's expansion is on the order of z^{-1} as well, it has no terms before the Green's function's third order.

By equating Eq. (2.18) and Eq. (2.19) up to the second order, we get the conditions

$$\int_{-\infty}^{\infty} \mathrm{d}\epsilon \rho_{m\sigma}(\epsilon) = 1 \tag{2.20}$$

and

$$\int_{-\infty}^{\infty} \mathrm{d}\epsilon \cdot \epsilon \rho_{m\sigma}(\epsilon) = \epsilon_m. \tag{2.21}$$

The first condition imposes normalization on the DOS. The second gives the criteria for setting the AIM's spin-orbital energies - each should be the statistical center of mass of the respective projected DOS.

The FLAPW method is sensitive to the choice of the muffin-tin radius, since part of the impurity's electronic density remains outside of it. As a result, the total sum of states as calculated by the FLAPW method is expected to be less than 1. Each spin-orbital will thus be manually normalized by dividing it by the integral $A_{m\sigma}$. The integrals $A_{m\sigma}$ will be later used to re-normalize the hybridization function.

The occupation of a spin-orbital in the limit of low temperatures is the integral of the DOS over energy, weighed by the Fermi-Dirac function:

$$n_{m\sigma} = \int_{-\infty}^{\infty} \mathrm{d}\epsilon f(\epsilon)\, \rho_{m\sigma}(\epsilon)\,. \tag{2.22}$$

For low temperatures, the occupation is simply the integral up to the Fermi energy:

$$n_{m\sigma} \approx \int_{-\infty}^{\epsilon_F} \mathrm{d}\epsilon \rho_{m\sigma}(\epsilon)\,. \tag{2.23}$$

2.3 Crystal field splitting and spin-orbit coupling terms

The electronic structure of an individual atom in vaccum is usually described in the basis of atomic orbitals, where the angular part of each orbital is a Laplace spherical harmonic. The advantage of this basis is that each of its states is described uniquely by the quantum numbers $\{n, l, m\}$. However, in quantum chemistry it is customary to work in the basis of real harmonics, since computation with real numbers is considerably less expensive than with complex numbers. The real harmonics are sometimes called cubic harmonics, since their shape is relatively simple to describe in a Cartesian coordinate system.

A d valence shell (i.e. with azimuthal quantum number $l = 2$) has five orbitals. Its spherical harmonics are

$$\begin{pmatrix} Y_2^{-2} \\ Y_2^{-1} \\ Y_2^{0} \\ Y_2^{1} \\ Y_2^{2} \end{pmatrix} = \sqrt{\frac{15}{8\pi}} \begin{pmatrix} \frac{(x-iy)^2}{2r^2} \\ \frac{(x-iy)z}{r^2} \\ \frac{3z^2-r^2}{\sqrt{6}r^2} \\ -\frac{(x+iy)z}{r^2} \\ \frac{(x+iy)^2}{2r^2} \end{pmatrix}. \tag{2.24}$$

In the basis of cubic harmonics, the orbitals are denoted as

$$m \in \left\{ yz, xz, xy, x^2-y^2, 3z^2-r^2 \right\}. \tag{2.25}$$

The transition from spherical harmonics Y_l^m to cubic harmonics K_l^m is done using the following transformation matrix [45]:

$$\begin{pmatrix} K_2^{yz} \\ K_2^{zx} \\ K_2^{xy} \\ K_2^{x^2-y^2} \\ K_2^{3z^2-r^2} \end{pmatrix} = \sqrt{\frac{15}{4\pi}} \begin{pmatrix} \frac{yz}{r^2} \\ \frac{zx}{r^2} \\ \frac{xy}{r^2} \\ \frac{x^2-y^2}{2r^2} \\ \frac{3z^2-r^2}{2\sqrt{3}r^2} \end{pmatrix} = \begin{pmatrix} & \frac{i}{\sqrt{2}} & & \frac{i}{\sqrt{2}} & \\ & \frac{1}{\sqrt{2}} & & -\frac{1}{\sqrt{2}} & \\ \frac{i}{\sqrt{2}} & & & & -\frac{i}{\sqrt{2}} \\ \frac{1}{\sqrt{2}} & & & & \frac{1}{\sqrt{2}} \\ & & 1 & & \end{pmatrix} \begin{pmatrix} Y_2^{-2} \\ Y_2^{-1} \\ Y_2^{0} \\ Y_2^{1} \\ Y_2^{2} \end{pmatrix}. \tag{2.26}$$

In the absence of external potentials, the energies of all orbitals of the same shell are equal. An atom embedded in a crystal, however, experiences a potential

induced by the electric field of the surrounding atoms which breaks the degeneracy of the valence states. The contribution of the crystal field to the energy of each orbital can be evaluated by measuring the potential inside the muffin-tin sphere. The potential from the surrounding atoms at positions $\mathbf{R}_j$ and charges q_j is [46]

$$v\left(\mathbf{r}\right)=e\sum_{j}\frac{q_j}{\left|\mathbf{r}-\mathbf{R}_j\right|}.$$

where e is the electron charge. When expanded around $\mathbf{r}=0$, the potential of an octahedral ligand structure with a distance is

$$v_{\mathrm{oct}}\left(\mathbf{r}\right)=\frac{35q_{\mathrm{oct}}}{4a^5}\left(\frac{3}{5}r^4-x^4-y^4-z^4\right),$$

where all ligand atoms are of charge q_{oct} and are at a distance of a from the central atom [45, 46]. A cubic ligand structure with the same charges and a side length of $2a$ has a potential of a similar shape but inverted sign [45]:

$$v_{\mathrm{cube}}\left(\mathbf{r}\right)=-\frac{8}{9}v_{\mathrm{oct}}\left(\mathbf{r}\right).$$

The crystal field contribution to the energy of each orbital is

$$\varepsilon_l^m=I_r\int_{\mathrm{MT}}\mathrm{d}\mathbf{r}v_{\mathrm{cube}}\left(\mathbf{r}\right)\left|K_l^m\left(\mathbf{r}\right)\right|^2, \tag{2.27}$$

where I_r is the part of the integral which depends on the radial component. As can be seen, for the cubic harmonics K_2^{yz}, K_2^{zx} and K_2^{xy}, the integrals are identical up to coordinate change. Performing the calculation for $K_2^{x^2-y^2}$ and $K_2^{3z^2-r^2}$ shows that their energies are equal too [45, 46]. Cubic symmetry thus splits the orbitals into two groups — t_{2g} for $\{yz,xz,xy\}$ and e_g for $\{x^2-y^2,3z^2-r^2\}$.

The local Hamiltonian described in Eq. (2.1) can now be extended to include the energy splitting induced by the crystal field $\Delta_{mm'}^{\mathrm{CF}}$, as well as the spin-orbit coupling term $\xi\mathbf{l}\cdot\mathbf{s}$:

$$\hat{H}_0=\sum_{mm'\sigma\sigma'}\left(\epsilon_d\delta_{mm'}+\Delta_{mm'}^{\mathrm{CF}}+\xi\mathbf{l}\cdot\mathbf{s}\right)d_{m\sigma}^{\dagger}d_{m'\sigma'}. \tag{2.28}$$

The spin vector $\mathbf{s}$ is

$$\mathbf{s}=\frac{1}{2}\sum_{m\sigma\sigma'}d_{m\sigma}^{\dagger}\vec{\sigma}_{\sigma\sigma'}d_{m\sigma'}, \tag{2.29}$$

with $\vec{\sigma}$ from Eq. (1.26).

In a system with cubic symmetry, the orbital vector $\mathbf{l}=\mathbf{l}_{t_{2g}}+\mathbf{l}_{e_g}$ consists of separate parts for t_{2g} and e_g orbitals [47]:

$$\mathbf{l}_{t_{2g}}=i\sum_{\sigma}\left(\sum_{m'm''\in\{yz,xz,xy\}}\epsilon_{mm'm''}d_{m'\sigma}^{\dagger}d_{m''\sigma}\right), \tag{2.30}$$

$$\mathbf{l}_{e_g}=\frac{1}{2}\sum_{\sigma}\left(\sum_{mm'\in\{x^2-y^2,3z^2-r^2\}}d_{m\sigma}^{\dagger}\vec{\sigma}_{mm'}d_{m'\sigma}\right), \tag{2.31}$$

where $\epsilon_{mm'm''}$ is the Levi-Civita symbol, and $\vec{\sigma}_{mm'}$ is the Pauli matrix vector applied to the two e_g levels instead of two spins.

The spin-orbit coupling strength ξ is calculated using the LDA solution inside the muffin-tin radius [48]:

$$\xi = \int_0^{R_{MT}} dr \cdot r \frac{1}{2\left(M_l\left(r\right)c\right)^2} \frac{\mathrm{d}V\left(r\right)}{\mathrm{d}r} \left(u_l\left(r\right)\right)^2, \tag{2.32}$$

where $V\left(r\right)$ is the atomic potential, $u_l\left(r\right)$ are the radial solutions of the Kohn-Sham-Dirac scalar-relativistic equations, and $M_l\left(r\right) = m + \frac{E_l - V(r)}{2c^2}$ is the relativistic mass with E_l as the eigenenergy of $u_l\left(r\right)$.

2.4 Continuous-time quantum Monte Carlo

Solving the Anderon impurity model entails finding the full local Green's function. This is a challenging task, since intra-d-shell interactions in the impurity greatly complicate the structure of the Hamiltonian, and prevent the sort of analytical simplifications performed in Sec. 2.2. One of the most common approaches to deal with the complexity is continuous-time quantum Monte Carlo [49]. It is applicable to systems with arbitrary bath size, but its quality goes down at low temperatures.

In general, a Monte Carlo algorithm calculates the value of an observable in a thermodynamic system using a representative sampling of the system's thermodynamic ensemble, obtained by stochastically transitioning from state to neighboring state over the course of many steps. In the case of continuous-time quantum Monte Carlo, the ensemble in question is the sum of all Feynman diagrams contributing to the interacting imaginary-time Green's function of the impurity.

The thermodynamic ensemble of the system is encoded in its partition function, which can be expressed as

$$Z = \mathrm{Tr}\left[\hat{T}_\tau e^{-\int_0^\beta \mathrm{d}\tau \hat{H}(\tau)}\right]. \tag{2.33}$$

The parameter τ represents imaginary time — an analytical continuation of time into the imaginary number line, so that the thermodynamic beta is $\beta \equiv -i\tau$. In the expression above, $\hat{T}_\tau$ is the imaginary time-ordering operator, and $\hat{H}\left(\tau\right)$ is the system's Hamiltonian in the interaction picture. The Hamiltonian is split into two parts — the exactly solvable, time-independent $\hat{H}_0$ and the time-dependent $\hat{H}_1$:

$$\hat{H}\left(\tau\right) = \hat{H}_0 + \hat{H}_1\left(\tau\right) \tag{2.34}$$

There are multiple possible ways to split the Hamiltonian into $\hat{H}_0$ and $\hat{H}_1$, depending on the physical properties of the system, such as the size of the impurity, the strength of the interaction parameters and the temperature. Out of those, the algorithm most applicable for strongly-correlated single-impurity systems and to relatively low temperatures is the hybridization expansion (CT-HYB), where $\hat{H}_0$ describes a bath and an interacting impurity decoupled from each other and $\hat{H}_1$ is

the impurity-bath coupling term. Though the bath is continuous, it is discretized for the purposes of the calculation. The Hamiltonian's parts are thus

$$\hat{H}_0 = \hat{H}_{\text{loc}} + \hat{H}_{\text{bath}} \tag{2.35}$$

and

$$\hat{H}_1(\tau) = \sum_{mk} \left(V_{mk} d^\dagger_{m\sigma}(\tau) b_{mk\sigma}(\tau) + V^\star_{mk} d_{m\sigma}(\tau) b^\dagger_{mk\sigma}(\tau) \right). \tag{2.36}$$

The full derivation of the CT-HYB partition function appears in Ref. [49]. The derivation consists of taking the time-independent part out of the integral, expressing the time-dependent exponent as a Taylor series, time-ordering each term in the series, cancelling the terms where the creation and annihilation operators aren't paired, separating the bath operators from the impurity operators and integrating the bath operators out. Additionally, since the bath-impurity coupling is diagonal in the impurity's spin-orbital basis, the partition function can be factorized into separate partition functions for each orbital. The resulting partition function takes the form

$$Z = \prod_{m\sigma} Z_m, \tag{2.37}$$

where the partition function of each separate orbital is

$$\begin{aligned} Z_{m\sigma} &= Z_{\text{bath}} \det\left[\boldsymbol{\Delta}^m\right] \\ &\times \sum_{n=0}^{\infty} \iiiint \mathrm{d}\tau_1 \cdots \mathrm{d}\tau_n \mathrm{d}\tau'_1 \cdots \mathrm{d}\tau'_n \mathrm{Tr}\left[\hat{T}_\tau e^{-\beta \hat{H}_{\text{loc}}} d_{m\sigma}(\tau_n) d^\dagger_{m\sigma}(\tau'_n) \cdots d_{m\sigma}(\tau_1) d^\dagger_{m\sigma}(\tau'_1) \right]. \end{aligned} \tag{2.38}$$

Z_{bath} is the partition function of the bath. $\det\left[\boldsymbol{\Delta}^m\right]$ is the determinant of the matrix $\boldsymbol{\Delta}$ whose elements are the imaginary time hybridization functions

$$\boldsymbol{\Delta}^m_{ij} = \tilde{\Delta}_m(\tau_i - \tau_j), \tag{2.39}$$

generalized to the non-diagonal case from Eq. (2.49) and transformed, so that

$$\tilde{\Delta}_m(\tau) = \frac{1}{\beta} \sum_n e^{i\omega_n \tau} \sum_k \frac{|V_{mk}|^2}{i\omega_n - \epsilon_k} = \sum_k \frac{|V_{mk}|^2}{e^{\beta\epsilon_k} + 1} \times \begin{cases} -e^{-\epsilon_k(\tau-\beta)} & 0 < \tau < \beta \\ e^{-\epsilon_k \tau} & -\beta < \tau < 0 \end{cases}. \tag{2.40}$$

Each of the configurations that are summed and integrated over in Eq. (2.38) represents the imaginary time evolution of the impurity, with ladder operators adding and removing particles. Each operator pair $d_{m\sigma}(\tau_n) d^\dagger_{m\sigma}(\tau'_n)$ can be represented by a segment contained in the periodic line $[0, \beta)$, with no two segments overlapping. Each term of the interaction only affects imaginary time intervals in which all involved impurity electrons are present.

The most widely used updating method in CT-QMC is the Metropolis-Hastings algorithm, a relatively simple method that preserves detailed balance [50, 51]. The details of the methods are described in Appendix A.2.

The Green's function is calculated in the imaginary time domain:

$$\begin{aligned} G_{mm'\sigma\sigma'}\left(\tau_A-\tau_B\right) &= -\left\langle \hat{T}_\tau d_{m\sigma}\left(\tau_A\right) d^\dagger_{m'\sigma'}\left(\tau_B\right)\right\rangle_{S_{\text{eff}}} \\ &= -Z_{\text{bath}} \det\left[\mathbf{\Delta}^m\right] \sum_{n,\{i\}} \iiiint \mathrm{d}\tau_1 \cdots \mathrm{d}\tau'_n \\ &\times \mathrm{Tr}\left[\hat{T}_\tau e^{-\beta \hat{H}_{\text{loc}}} d_{m\sigma}\left(\tau_A\right) d^\dagger_{m'\sigma'}\left(\tau_B\right) d_{i_n}(\tau_n) d^\dagger_{i_n}(\tau'_n) \cdots d_{i_1}(\tau_1) d^\dagger_{i_1}(\tau'_1)\right]. \end{aligned} \tag{2.41}$$

Since an n-order configuration with the added points at τ_A and τ_B is equivalent to an $n+1$-order configuration where those points are part of the ensemble, Green's function can be measured by taking two of the configuration's points, designating them τ_A and τ_B and treating the calculated trace as a contribution to the value of $G_{mm'\sigma\sigma'}\left(\tau_A-\tau_B\right)$.

2.5 Exact diagonalization

The exact diagonalization model consists of an impurity with N_d spin-orbitals, each of which is coupled to N_k bath orbitals. The total number of spin-orbitals in the system is $N_{\text{tot}} = N_d\left(N_k+1\right)$.

The bath of Eq. (2.8) will be discretized — the continuous energy spectrum ϵ will be replaced by N_k discrete energy levels ϵ_{mk}, coupled to the m impurity orbital by amplitude V_{mk}. The crystal field term will be assumed to be diagonal and included in the orbital energy ϵ_m. The SOC term will be neglected, due to the difficulty of extending the fitting (which will be described further on) to a non-diagonal local Hamiltonian. The new Hamiltonian is

$$\begin{aligned} \hat{H}_{\text{imp}} &= \sum_{m\sigma} \epsilon_m n^d_{m\sigma} \\ &+ \frac{1}{2} \sum_{abcd\sigma\sigma'} U_{abcd} d^\dagger_{a\sigma} d^\dagger_{b\sigma'} d_{c\sigma'} d_{d\sigma} \qquad (2.42) \\ &+ \sum_{mk\sigma} \epsilon_{mk} n^b_{mk\sigma} + \sum_{mk\sigma} \left(V_{mk} d^\dagger_{m\sigma} b_{mk\sigma} + \text{h.c.}\right). \qquad (2.43) \end{aligned}$$

An example of the model's structure is depicted in Fig. 2.1, for the case of an impurity in a potential with cubic symmetry and 4 bath orbitals. Each rectangle represents a two-electron site. Each impurity orbital is coupled to the four sites in the respective bath column. In this example, there are zero bath excitations — all and only the bath states below the Fermi energy are occupied.

The energies and amplitudes of the discrete bath will be chosen to make the discrete model represent the behavior of the continuous model's impurity as accurately as possible. Since the effect of the bath on the impurity is encoded entirely in the hybridization function, the discrete model will be built by fitting its hybridization function to the hybridization function of the continuous model.

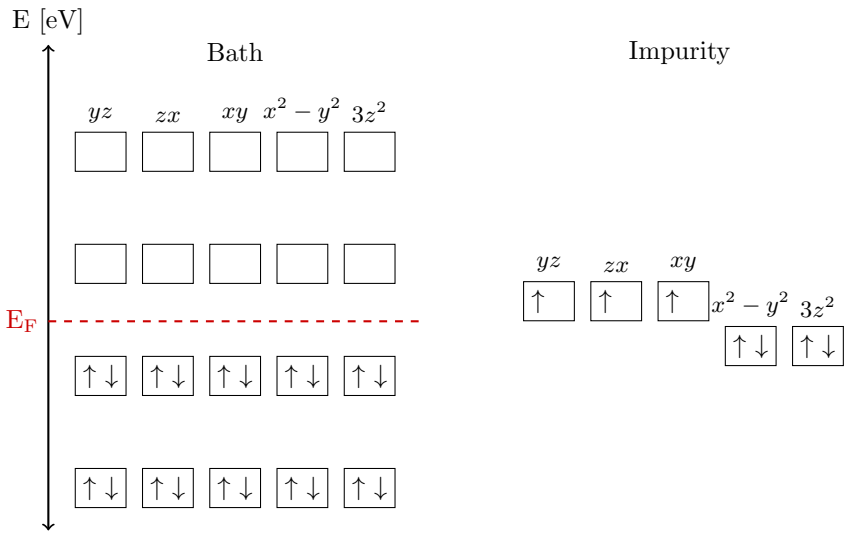

Figure 2.1: Illustration of the discrete AIM with a $3d$-shell impurity in the basis of cubic harmonics, where each impurity orbital is coupled to four bath sites. The depicted configuration has $N_{\mathrm{tot}} = 28$ with no bath excitations.

The fitting will be performed in the Matsubara frequency space $\omega_n = \frac{\pi}{\beta}(2n+1)$, where β is the inverse temperature. Unlike the real energy space, where the discrete model hybridization function has singularities at each energy level and the continuous model hybridization function is non-smooth if it is derived from a non-smooth DOS, the Matsubara frequency hybridization function is smooth and continuous over its entire domain. The hybridization function is derived from the DOS in the manner shown in Sec. 2.2.

$$G_{m\sigma}(i\omega_n) = \int_{-\infty}^{\infty} \mathrm{d}\epsilon \frac{\rho_{m\sigma}(\epsilon)}{i\omega_n - \epsilon_m}, \tag{2.44}$$

$$\Delta_{m\sigma}(i\omega_n) = i\omega_n - \epsilon_m - G_{m\sigma}^{-1}(i\omega_n). \tag{2.45}$$

If the given DOS has been normalized as shown in SSec. 2.2 for the purpose of calculating the hybridization function, the hybridization function will be denormalized, so that its analytical continuation to real frequencies will have a real part which corresponds to the original DOS. If the normalized DOS is $\rho'_{m\sigma} \equiv \rho_{m\sigma}(\epsilon)/A_{m\sigma}$, the effect of the normalization on the Green's function is

$$G'_{m\sigma}(i\omega_n) = \int_{-\infty}^{\infty} \mathrm{d}\epsilon \frac{\rho'_{m\sigma}(\epsilon)}{i\omega_n - \epsilon - \epsilon_m} = \frac{G_m(i\omega_n)}{A_{m\sigma}}. \tag{2.46}$$

The effect is similar in real frequencies due to the analytical continuity of the Green's function over the two domains. The effect on the real frequency hybridization function is thus

$$\mathrm{Im}\left[\Delta'_{m\sigma}(\epsilon)\right] = -\mathrm{Im}\left[\left[G'_{m\sigma}\right]^{-1}(\epsilon)\right] = -A_{m\sigma}\mathrm{Im}\left[G_m^{-1}(\epsilon)\right] = A_{m\sigma}\mathrm{Im}\left[\Delta_m(\epsilon)\right]. \tag{2.47}$$

For the same analytical continuity argument as with the Green's function, the effect can be generalized back to Matsubara frequencies. The de-normalization process is therefore

$$\Delta_{m\sigma}\left(i\omega_n\right) = \frac{\Delta'_{m\sigma}\left(i\omega_n\right)}{A_{m\sigma}}. \tag{2.48}$$

2.5.1 Fitting

The Matsubara frequency hybridization function of the discrete Anderson model in Eq. (2.43) is

$$\tilde{\Delta}_{m\sigma}\left(i\omega_n\right) = \sum_{k=1}^{N_k} \frac{V_{mk}^2}{i\omega_n - \epsilon_{mk}}. \tag{2.49}$$

The fitting is done by minimizing the residual function

$$f_m\left(\{\epsilon_{km}, V_{km}\}\right) = \sum_{n=1}^{N_\omega} \frac{1}{\omega_n^\gamma} \left|\tilde{\Delta}_{m\sigma}\left(i\omega_n\right) - \Delta_{m\sigma}\left(i\omega_n\right)\right|^2. \tag{2.50}$$

The factor $\frac{1}{\omega_n^\gamma}$ is used to attenuate the significance of the higher frequencies. The higher γ is, the more the minimization neglects the hybridization function's tail. We will always set $\gamma = \frac{1}{2}$.

The minimization is done using the Limited-memory, bounded Broyden-Fletcher-Goldfarb-Shanno method (L-BFGS-B) [52, 53] in the space of parameters $\{\epsilon_{mk}, V_{mk}\}$. In the algorithm, the direction of the next iteration's step is determined by the gradient of the residual function. In the Fortran implementation we used, the function's gradient needs to be supplied manually per step. It was therefore calculated analytically as a function of $i\omega_n$, $\Delta_m\left(i\omega_n\right)$ and $\{\epsilon_{mk}, V_{mk}\}$ from Eq. (2.49) and Eq. (2.50). It is expressed as

$$g = \nabla f\left(\{\epsilon_k, V_k\}\right) = \left[\frac{\partial f}{\partial \epsilon_k}, \frac{\partial f}{\partial V_k}\right], \tag{2.51}$$

where

$$\frac{\partial f}{\partial \epsilon_k} = -\sum_{n=1}^{N_\omega} \frac{2}{\sqrt{\omega_n}} \left(\mathrm{Re}\left[\Delta - \tilde{\Delta}\right] \frac{\partial \mathrm{Re}\left[\tilde{\Delta}\right]}{\partial \epsilon_k} + \mathrm{Im}\left[\Delta - \tilde{\Delta}\right] \frac{\partial \mathrm{Im}\left[\tilde{\Delta}\right]}{\partial \epsilon_k}\right), \tag{2.52}$$

$$\frac{\partial f}{\partial V_k} = -\sum_{n=1}^{N_\omega} \frac{2}{\sqrt{\omega_n}} \left(\mathrm{Re}\left[\Delta - \tilde{\Delta}\right] \frac{\partial \mathrm{Re}\left[\tilde{\Delta}\right]}{\partial V_k} + \mathrm{Im}\left[\Delta - \tilde{\Delta}\right] \frac{\partial \mathrm{Im}\left[\tilde{\Delta}\right]}{\partial V_k}\right). \tag{2.53}$$

The analytical derivatives of $\tilde{\Delta}$ are

$$\frac{\partial \tilde{\Delta}}{\partial \epsilon_k} = \frac{V_k^2}{\left(i\omega_n - \epsilon_k\right)^2} = \frac{V_k^2}{2i\omega_n\epsilon_k - \epsilon_k^2 - \omega_n^2}, \tag{2.54}$$

$$\frac{\partial \tilde{\Delta}}{\partial V_k} = \frac{2V_k}{i\omega_n - \epsilon_k}. \tag{2.55}$$

2.5.2 Diagonalization and calculation of observables

The complete Fock space of the system whose Hamiltonian is Eq. (2.43) is spanned by all possible occupation configurations of the system's N_{tot} sites. If we sort the configurations by occupation number N and make a separate space for each N, we can describe the Fock space as the direct sum of $N_{\text{tot}}+1$ Hilbert spaces, where the N-th Hilbert space is spanned by all of the possible ways N electrons can be distributed across N_{tot} sites. A method for truncating the dimensionality of each Hilbert space is presented in Sec. 2.5.4.

The eigenstates of $\hat{H}_{\text{imp}}$ in the Hilbert space N will be denoted as $|N\alpha\rangle$, where α is the eigenstate index. The eigenvalues will be denoted as $E_{N\alpha}$, so that $\hat{H}_{\text{imp}}|N\alpha\rangle = E_{N\alpha}|N\alpha\rangle$. Observables are calculated in the grand-canonical ensemble, as a sum over the weighted averages in each sector:

$$\left\langle \hat{O} \right\rangle = \frac{1}{Z}\sum_{N,\alpha} e^{-\beta E_{N\alpha}} \langle N\alpha| \hat{O} |N\alpha\rangle , \tag{2.56}$$

where $\beta \equiv \frac{1}{k_B T}$ is the inverse temperature and $Z = \sum_{N,\alpha} e^{-\beta E_{N\alpha}}$ is the grand partition function. The chemical potential is included in the energy $E_{N\alpha}$.

The Green's function is calculated in the grand-canonical ensemble as the sum of the retarded and advanced Green's functions [44]. The diagonal elements of the Green's function are

$$G_{mm\sigma\sigma}(z) = \frac{1}{Z}\sum_{N,\alpha} e^{-\beta E_{N\alpha}} \left(\left[G^{>}_{N\alpha}(z) \right]_{mm\sigma\sigma} + \left[G^{<}_{N\alpha}(z) \right]_{mm\sigma\sigma} \right), \tag{2.57}$$

where

$$\left[G^{>}_{N\alpha}(z) \right]_{mm\sigma\sigma} = \langle N\alpha| d_{m\sigma} \left(z + E_{N\alpha} - \hat{H}_{\text{imp}} \right)^{-1} d^{\dagger}_{m\sigma} |N\alpha\rangle , \tag{2.58}$$

$$\left[G^{<}_{N\alpha}(z) \right]_{mm\sigma\sigma} = \langle N\alpha| d^{\dagger}_{m\sigma} \left(z - E_{N\alpha} + \hat{H}_{\text{imp}} \right)^{-1} d_{m\sigma} |N\alpha\rangle . \tag{2.59}$$

The Lehmann representation of Green's function describes it in terms of transition amplitudes between different eigenstates.

$$\begin{aligned} G^{>}_{mm\sigma\sigma}(z) &= \sum_{N\alpha,N'\alpha'} \left| \langle N\alpha| d^{\dagger}_{m\sigma} |N'\alpha'\rangle \right|^2 \frac{e^{-\beta E_{N\alpha}} + e^{-\beta E_{N'\alpha'}}}{z + E_{N\alpha} - E_{N'\alpha'}} \\ &= \sum_{N\alpha\alpha'} \left| \langle N\alpha| d^{\dagger}_{m\sigma} |N-1,\alpha'\rangle \right|^2 \frac{e^{-\beta E_{N\alpha}} + e^{-\beta E_{N-1,\alpha'}}}{z + E_{N\alpha} - E_{N-1,\alpha'}}. \end{aligned} \tag{2.60}$$

The density of states is calculated using Eq. (2.11). In the Lehmann representation, it acquires the form

$$\rho_{m\sigma}(\epsilon) = \sum_{N\alpha\alpha'} \left| \langle N\alpha| d^{\dagger}_{m\sigma} |N-1,\alpha'\rangle \right|^2 \left(e^{-\beta E_{N\alpha}} + e^{-\beta E_{N-1,\alpha'}} \right) \delta\left(\epsilon + E_{N\alpha} - E_{N-1,\alpha'} \right). \tag{2.61}$$

In this form it is apparent that the spectral density is made of resonance peaks between eigen-energies in neighboring sectors. The resonance peaks are very

dense, which makes the DOS a continuous spectrum at high temperatures, when broadened by the imaginary additive in Eq. (2.11). For very low temperatures ($\beta \gg 1$) all eigen-energy contributions to Eq. (2.61) fall off except for the ground state energies, which makes the resonance peaks between them sparse enough to be visible.

2.5.2.1 Discrete domain

The energy domain of the computer model is a discrete collection of values that are arranged uniformly between the minimum and maximum energy (which are opposites) with a resolution of $\Delta\epsilon$. An imaginary additive of η creates a peak with a full width at half-maximum (FWHM) of 2η: with $f(\epsilon) \equiv \mathrm{Im}\left[1/(\epsilon - i\eta)\right]$ as a single broadened peak around $\epsilon = 0$, the two energies at half maximum are ϵ_0, where

$$\begin{aligned} f(\epsilon_0) &\stackrel{!}{=} \frac{f(\epsilon)}{2}, \\ \mathrm{Im}\left[\frac{1}{\epsilon_0 - i\eta}\right] = \frac{\eta}{\epsilon_0^2 + \eta^2} &\stackrel{!}{=} \frac{1}{2\eta}, \\ \epsilon_0 &= \pm\eta. \end{aligned}$$

A discretized integral over $f(\epsilon)$ diverges for imaginary additives that approach zero. In order to prevent the integral from diverging, the imaginary additive will not be set to a smaller value than $\pi\Delta\epsilon$.

2.5.3 The Lanczos method

The diagonalization of each sector's Hamiltonian matrix is performed using the implicitly restarted Lanczos method implemented in the Arnoldi Package (ARPACK) [44, 54]. The Lanczos method is a special case of Arnoldi iteration for Hermitian matrices, used to approximate the extremal (largest or smallest; in our case, the latter) eigenvalues of a matrix. It uses an iterative process to transform the Hamiltonian matrix $\mathbf{H}$ into a tridiagonal matrix $\mathbf{T}$, which can then be easily diagonalized.

The tridiagonalization process starts by setting up an arbitrary normalized Lanczos vector $\mathbf{v}_1$ with a non-zero overlap with every eigenvector of $\mathbf{H}$. Each subsequent Lanczos vector is generated by multiplying $\mathbf{H}$ by the previous Lanczos vector, orthogonalizing the result to the previous Lanczos vectors and normalizing it. After n iterations, the result is the the unitary matrix $\mathbf{V}$ with vectors $\mathbf{v}_1 \ldots \mathbf{v}_n$ and the tridiagonal matrix $\mathbf{T}$ which fulfills

$$\mathbf{T} = \mathbf{V}^\dagger \mathbf{H} \mathbf{V}.$$

The diagonal and near-diagonal elements of $\mathbf{T}$ are produced during the iterative process [55].

The implicitly restarted Lanczos method is an algorithmic variant of Lanczos method which reduces the storage and computational requirements. It does so by periodically compressing the size of the Krylov space spanned by vectors $\mathbf{v}_i$ to

N	full	N_{exc}				
		1	2	3	4	5
26	$1.22 \cdot 10^{14}$	7650	$1.4 \cdot 10^{6}$	$1.7 \cdot 10^{7}$	$1.53 \cdot 10^{7}$	$1.09 \cdot 10^{8}$
27	$1.08 \cdot 10^{14}$	5220	$1.03 \cdot 10^{6}$	$1.31 \cdot 10^{7}$	$1.22 \cdot 10^{7}$	$8.86 \cdot 10^{7}$
28	$8.87 \cdot 10^{13}$	2645	$6.07 \cdot 10^{5}$	$8.42 \cdot 10^{6}$	$8.29 \cdot 10^{6}$	$6.27 \cdot 10^{7}$
29	$6.73 \cdot 10^{13}$	930	$2.77 \cdot 10^{5}$	$4.42 \cdot 10^{6}$	$4.76 \cdot 10^{6}$	$3.83 \cdot 10^{7}$
30	$4.71 \cdot 10^{13}$	201	9151	$1.84 \cdot 10^{6}$	$2.26 \cdot 10^{6}$	$2 \cdot 10^{7}$

Table 2.1: Dimensions of the full and reduced Hilbert space for $N_{\text{d}} = 10$, $N_b = 20$ and $N_{\underline{b}} = 20$, for selected values of N and N_{exc}.

a smaller collection of Lanczos vectors, so that their orthonormality is conserved and the components with the desired quality (in our case — small eigenvalues) are enhanced. This process is known as implicit restarting, and is performed using a truncated form of the implicitly shifted QR scheme [54].

2.5.4 Reduced Fock space

The Hilbert space of a system with N_{tot} sites occupied by N electrons is spanned by $\binom{N_{\text{tot}}}{N}$ states. For all models except for the simplest ones this number can get exceedingly large — a AIM with a d valence shell and a 4-peak discrete bath (50 states) populated by 28 electrons, for example, has a dimension of 88.7 trillion. In order to make the Hilbert space more manageable, we employ the Gunnarsson-Schoenhammer expansion, which includes only bath fillings that are likely to contribute significantly to the grand-canonical potential [56, 44]. The reduced Hilbert space is expressed as

$$\mathcal{H}_N\left[N_{\text{exc}}\right] = \left\{ \left| f^n b^p \underline{b}^q \right\rangle, 0 \leq p+q \leq N_{\text{exc}}, n+p-q = N - N_{\underline{b}} \right\}, \tag{2.62}$$

where n is the number of electrons in the impurity valence shell, p is the number of bath electrons above the Fermi energy and q is the number of bath holes below the Fermi energy and $N_{\underline{b}}$ is the number of bath states below Fermi energy. The total number of excitations and holes in the bath is capped by the parameter N_{exc}. With $N_b = N_{\text{tot}} - N_{\text{imp}} - N_{\underline{b}}$ as the number of bath sites above Fermi energy, the dimensionality of the reduced Hilbert space is

$$\dim\left[\mathcal{H}_N\left[N_{\text{exc}}\right]\right] = \sum_{\substack{p+q \leq N_{\text{exc}} \\ n+p-q = N - N_{\underline{b}}}} \binom{N_{\text{imp}}}{n} \binom{N_b}{p} \binom{N_{\underline{b}}}{q}, \tag{2.63}$$

where $\binom{N}{n} \equiv \frac{N!}{n!(N-n)!}$ is the binomial coefficient.

As an example, the dimensions of full and reduced Hilbert spaces for selected electron occupations were calculated and are shown in Tab. 2.1. The system chosen for the calculations has 10 impurity levels and a bath of 40 levels, half of which are below Fermi level.

2.6 Summary

In this chapter, the formalism of multi-orbital AIM was presented. The method of constructing the model from the DFT output was shown in detail, justified by the requirement that the Green's function of the impurity model will match the Green's function of DFT. The orbital structure of a d valence shell in a crystal field was described. QMC was described in brief, as an alternative to ED. The methods of diagonalization and calculation of observables were shown, as well as the Fock space's representation in the software.

There are remaining implementation details that were not covered in this chapter — the choice of N_k, N_{exc} and double-counting term in AIM. Those will be described in the next chapter, as part of the theory's application to real materials.

Chapter 3

Application of DFT+ED to materials with magnetic $3d$ metal impurities

In this chapter, we use the DFT+ED method described in Sec. 2.5 to examine the properties of strongly correlated systems with cobalt impurities. In the first section, we study a cobalt impurity in bulk copper. We test our method by setting up a system with similar parameters to the DFT+QMC calculations in Ref. [57] (room temperature and zero SOC) and compare the results. We then perform diagonalization on a low-temperature system, with and without SOC, in order to study the behavior of the ground states and lowest excitations.

In the second section, we apply our method to study a cobalt adatom on a copper substrate. We detect a state where a resonance peak occurs, and spin-orbit coupling creates a singlet ground state, indicating a Kondo effect. We then calculate the differential conductance and find it to be in agreement with experimentally observed scanning tunneling spectroscopy (STS) measurements [58].

In the third section, we study a cobalt adatom situated on a Cu_2N layer on top of a copper substrate. We find a conducting mixed ground state with resonance between a singlet and a doublet, indicating a Kondo effect. The energy gaps between each sector's ground-state energy and the first excited energy are used to construct an effective model of the system's anisotropy, which is then used to sketch the system's differential conductance. We then use the method to study the effect of a strong external magnetic field on the system, and compare the results to X-ray magnetic circular dichroism (XMCD) measurements.

3.1 Kondo effect

AIM's main early success was the modeling of the Kondo effect — the scattering of conduction electrons by magnetic impurities, which contributes to the electric resistivity at low temperatures and converts its characteristic monotonically increasing shape into a convex shape with a resistance minimum at a positive temperature. The effect was explained by Kondo in 1964 [59] — he derived the magnetic impurity's logarithmic contribution to resistivity by constructing an Anderson-like model (the Kondo model) and applying third-order perturbation theory to AIM.

The Kondo model is single-impurity and spin-dependent. The derivation of Eq. (3.2) from the ground state and first excitation of the discrete AIM is shown in Appendix A.3. Its Hamiltonian is [3]

$$\hat{H}_{\mathrm{K}} = \sum_{k\sigma} \epsilon_k n_{k\sigma} + \sum_{kk'} J_{kk'} \mathbf{s}_{kk'} \mathbf{S}_d. \tag{3.1}$$

The second term represents the spin-impurity exchange interaction. The spin operators of the bath and impurity respectively are $\mathbf{s}_{kk'} \equiv \sum_{\sigma\sigma'} b^\dagger_{k\sigma} \vec{\sigma}_{\sigma\sigma'} b_{k'\sigma'}$ and $\mathbf{S}_d \equiv \sum_{\sigma\sigma'} d^\dagger_\sigma \vec{\sigma}_{\sigma\sigma'} d_{\sigma'}$. In the case of a spin parallel to the z-axis, the exchange interaction is simplified so that

$$\hat{H}_{\mathrm{K}} = \sum_{k\sigma} \epsilon_k n_{k\sigma} + \sum_{kk'} J_{kk'} \left(n^d_\uparrow - n^d_\downarrow \right) \left(b^\dagger_{k\uparrow} b_{k'\uparrow} - b^\dagger_{k\downarrow} b_{k'\downarrow} \right). \tag{3.2}$$

The coefficient $J_{kk'}$ represents the exchange interaction strength between the impurity and bath states k and k'. In Appendix A.3, its value is shown to be

$$J_{kk'} = V^\star_k V_{k'} \left(\frac{1}{\epsilon_d + U - \epsilon_{k'}} + \frac{1}{\epsilon_k - \epsilon_d} \right), \tag{3.3}$$

where ϵ_d is the single-impurity orbital energy and U is the impurity's electron interaction.

The sign of $J_{kk'}$ determines the nature of the exchange interaction. If $J_{kk'}$ is positive, the anti-parallel spin alignment is energetically preferrable, and the coupling anti-ferromagnetic. In that case, the system's lowest energy state is a singlet.

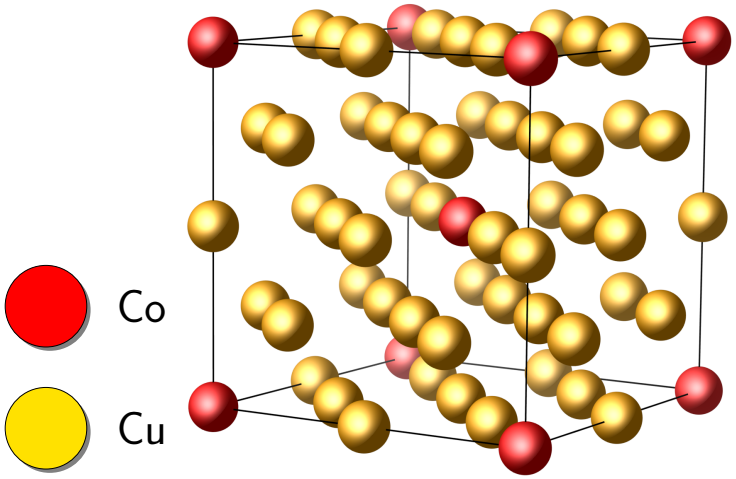

Figure 3.1: Model $CoCu_{15}$ supercell, consisting of two unit cells.

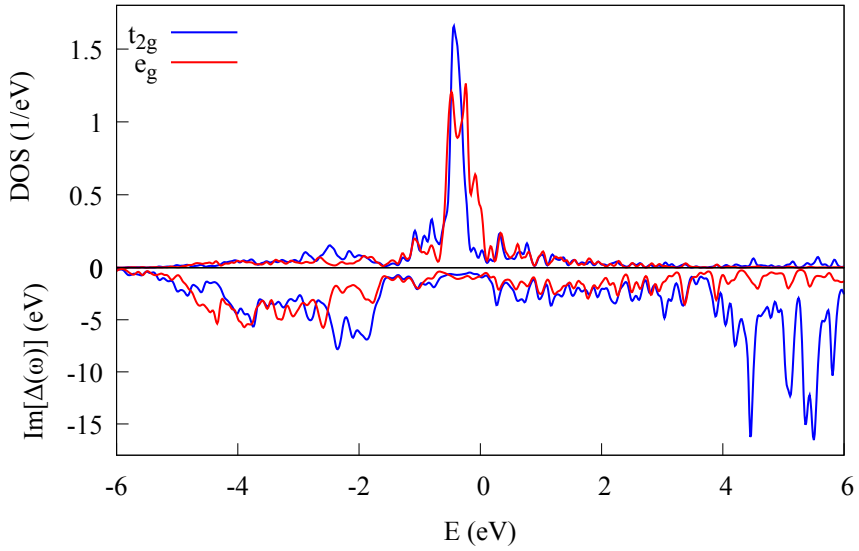

Figure 3.2: The projected t_{2g} and e_g orbital components of the LDA DOS (top) and the LDA hybridization function (bottom).

3.2 A cobalt atom in bulk copper

3.2.1 Setup, DFT and fitting

Cobalt is a transition metal whose incomplete shell is $3d$, a shell with an angular momentum number of $L = 2$ which holds 10 spin-orbital states. When coupled to a copper crystal with a *fcc* structure, the $3d$ orbitals become diagonal in the basis of cubic harmonics $m \in \{yz, xz, xy, x^2 - y^2, 3z^2 - r^2\}$, which was introduced in Sec. 2.3.

The cobalt impurity in bulk copper is modeled as $CoCu_{15}$, a $2 \times 2 \times 2$ *fcc* supercell of copper with a single atom substituted with a cobalt atom, as depicted in Fig. 3.1. The cubic crystal field splits the orbitals into two blocks, the triply-degenerate t_{2g} (for yz, xz and xy) and the doubly-degenerate e_g (for $x^2 - y^2$ and $3z^2 - r^2$), where the e_g block has a higher energy [45].

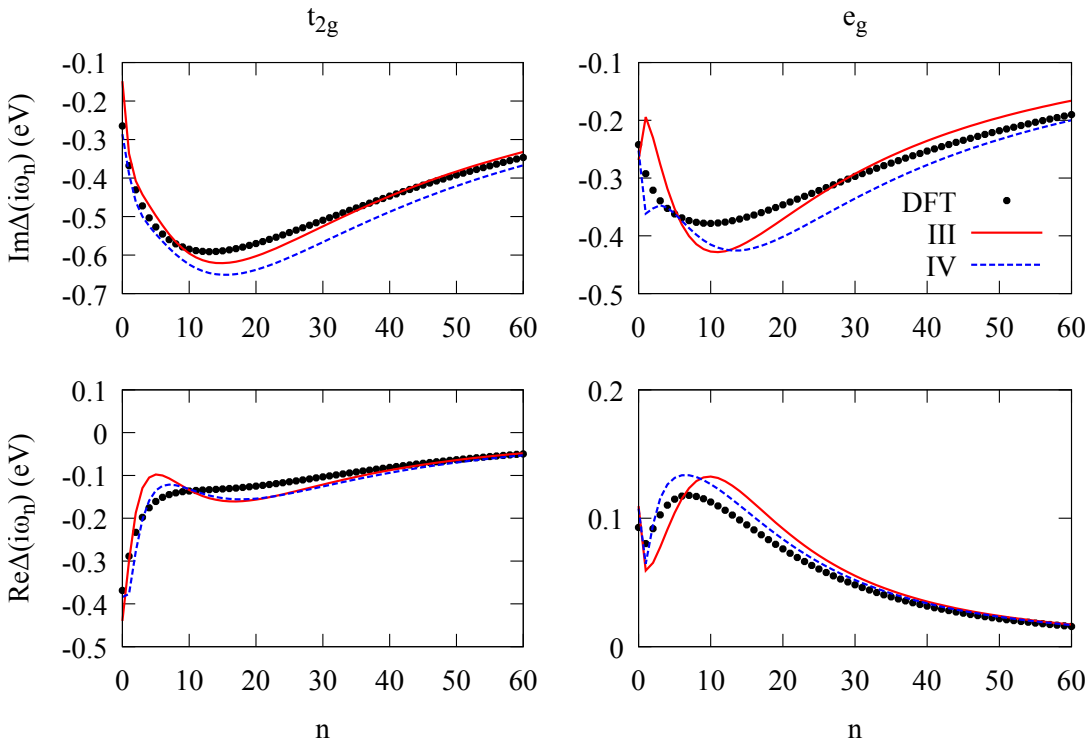

Figure 3.3: Fit of the discrete bath impurity model Eq. (2.49) to the DFT hybridization function Eq. (2.45) via minimization of the function in Eq. (2.50), using both sets of bath parameters in Tab. 3.1.

The material's electronic density was calculated using an implementation of the FLAPW method with LDA without spin-orbit coupling, as shown in Chapter 1 . The DOS for each spin-orbital was found by integrating the electronic density in the MT-sphere of the impurity. The upper cutoff of the DOS was chosen to be 6 eV. Fig. 3.2 shows the projected DOS for t_{2g} and e_g orbitals, as well as the imaginary part of the real-energy hybridization function.

The DOS of each orbital was normalized so that its total integral is equal to 1, in accordance with the condition in Eq. (2.20). This ensures that the occupation of each spin-orbital, which is the integral of the DOS up to the Fermi energy, can never exceed 1. The calculated occupations of the spin-orbitals are $n_{t_{2g}} = 0.772$ and $n_{e_g} = 0.793$. The total occupation is 7.804.

The DOS was used to construct the SIAM Hamiltonian of the material, which is shown in Eq. (2.43). The crystal field terms were found to be $\Delta^{\mathrm{CF}}_{t_{2g}} = 0.039$ eV and $\Delta^{\mathrm{CF}}_{e_g} = -0.059$ eV. Parameters ϵ_{mk} and V_{mk} were obtained by the fitting procedure described in Sec. 2.5, with $N_\omega = 637$. The parameter N_k defines the number of "bath" orbitals included in the discrete model: 30 spin-orbitals for $N_k = 3$ (model III), and 40 spin-orbitals for $N_k = 4$ (model IV). The fitting of the hybridization function is shown in Fig. 3.3, and the resulting parameters are shown in Tab. 3.1. The number of bath sites below Fermi energy for models III and IV is 10 and 20 respectively.

The interaction term of the impurity Hamiltonian was parameterized with the Slater integrals $F_0 = 4.0$ eV, $F_2 = 7.75$ eV and $F_4 = 4.85$ eV, which correspond to

m	k	ϵ_{mk} (eV)	V_{mk} (eV)
t_{2g}	1	-2.062	1.150
	2	0.316	0.407
	3	3.655	1.508
e_g	1	-2.337	1.077
	2	0.022	0.146
	3	1.395	0.790

m	k	ϵ_{mk} (eV)	V_{mk} (eV)
t_{2g}	1	-2.320	1.172
	2	-0.053	0.136
	3	0.432	0.476
	4	3.955	1.511
e_g	1	-2.693	1.104
	2	-0.132	0.206
	3	0.252	0.280
	4	2.306	0.830

Table 3.1: Values of the bath parameters ϵ_{mk} and V_{mk} obtained by fitting the hybridization function obtained from DFT, for models III (left) and IV (right).

	μ (eV)	N	ΔN	n_d	S	L	J	$Z_{t_{2g}}$	Z_{e_g}
DFT+ED, III	26	21.93	0.29	7.47	1.13	3.01	3.35	0.06	0.25
	27	22.31	0.50	7.77	0.99	2.89	3.18	0.10	0.23
	28	23.67	0.47	8.17	0.80	2.66	2.88	0.31	0.34
DFT+ED, IV	26	28.02	0.17	7.46	1.14	3.03	3.36	0.12	0.29
	27	28.71	0.49	7.77	0.99	2.90	3.18	0.30	0.23
	28	29.92	0.27	8.20	0.79	2.64	2.86	0.43	0.40
QMC[57]	26			7.51	1.02			0.38	0.39
	27			7.78	0.92			0.42	0.47
	28			8.06	0.82			0.48	0.56

Table 3.2: The total occupation N, fluctuation $\Delta N = \sqrt{\langle N^2 \rangle - \langle N \rangle^2}$, impurity occupation n_d, impurity spin S, orbital L and total moments J and quasiparticle weights $Z_{t_{2g}}$ and Z_{e_g} for each μ, at a temperature of $\beta = 40\,\mathrm{eV}^{-1}$, calculated by exact diagonalization and compared to the QMC calculations from Ref. [57].

an intra-orbital repulsion $U = 4.0$ eV and to an exchange interaction $J = 0.9$ eV, the characteristic values for $3d$ metals [17]. In order to correct for the double-counting of the Hartree-like contribution in the interaction term of Eq. (2.43), a constant value needs to be subtracted from the energy of each spin-orbital, physically interpreted as the chemical potential μ. This parameter defines the value of ϵ_d in Eq. (2.43), and was set to the three values used in Ref. [57], namely 26 eV, 27 eV and 28 eV. With two bath models and three chemical potential values, there are six discrete Anderson models in total.

The last step in the setup is the setting of the spin-orbit coupling. For the purpose of comparison of our method with Ref. [57], it will be set to zero. When modeling the Kondo effect, a SOC of $\xi = 0.079\,\mathrm{eV}$ is included, derived using Eq. (2.32). A minuscule magnetic field of 0.001 T in the direction of the z axis is added in order to force the angular momenta to align with the z axis.

μ (eV)	N	Energy (eV)	n_d	P_{d^6}	P_{d^7}	P_{d^8}	P_{d^9}	Multiplicity
26	28	−137.8498	7.459	0.082	0.413	0.449	0.050	3
27	28	−145.4226	7.689	0.046	0.317	0.532	0.100	3
	29	−145.4363	7.806	0.037	0.278	0.525	0.153	4
28	30	−153.4686	8.211	0.013	0.152	0.480	0.321	1
		−152.9139	8.083	0.015	0.176	0.532	0.268	3

Table 3.3: The energies and non-negligible (≥ 0.01) probability weights of impurity occupation numbers for the lowest eigen-energies of every sector, for different chemical potentials, for zero SOC. The multiplicity column indicates the number of eigenstates with the same energy and probability weights.

3.2.2 Exact diagonalization, comparison with CT-QMC

The exact diagonalization was performed using the Lanczos method in a reduced many-body Hilbert space, as described in Sec. 2.5. The excitation cutoffs were chosen to have the largest values allowed by memory constraints. The selected values were 5 for model III and 4 for model IV. The number of Lanczos states was set to 20. Convergence tests were performed in order to assess the influence of the number of Lanczos states on the results. No difference was found between the use of 20 or 60 Lanczos states.

For each model, several observables were measured as grand-canonical averages (Eq. (2.56)) — the total number of electrons, the occupation of the impurity d shell, and the spin moment in the d shell. The observables have been measured at room temperature, $\beta = 1/k_{\mathrm{B}}T = 40\,\mathrm{eV}^{-1}$, the same temperature used in Ref. [57]. The spin, orbital and total moments, S, L and J, were found using the expectation value $\langle \hat{O}^2 \rangle = \left\langle \hat{O}\left(\hat{O}+1\right)\right\rangle$. The results are shown in *Tab.* 3.2. For every value of μ, the observables of models III and IV are in good agreement with each other, which demonstrates convergence with respect to the bath-size parameter N_k. The observables of all models are in good agreement with the corresponding DFT+QMC results as well.

The mean impurity occupation is

$$n_d = \sum_n P_{d_n} \cdot n, \tag{3.4}$$

where P_{d_n} is the probability of finding n occupied spin-orbitals in the impurity. With $|\Omega_{N\alpha}\rangle$ as an eigenstate of the entire system and $|d_n i\rangle$ as the i-th impurity eigenstate with occupation n, $P_{d_n} = |\sum_i \langle d_n i|\Omega_{N\alpha}\rangle|^2$. The P_{d_n} values for each eigen-energy are shown in Tab. 3.3.

Since the Kondo effect is a low-temperature phenomenon that can't be observed directly at the high temperatures in which QMC is usually applied, the Kondo physics of the system were characterized in Ref. [57] with the help of renormalized perturbation theory [3]. By expressing the self-energy as a first-order Taylor expansion around $\omega = 0$

$$\Sigma_{m\sigma}(\omega) = \Sigma_{m\sigma}(0) + \omega \left.\frac{\partial \Sigma_{m\sigma}(\omega)}{\partial \omega}\right|_{\omega=0} + \Sigma^{\mathrm{rem}}_{m\sigma}(\omega), \tag{3.5}$$

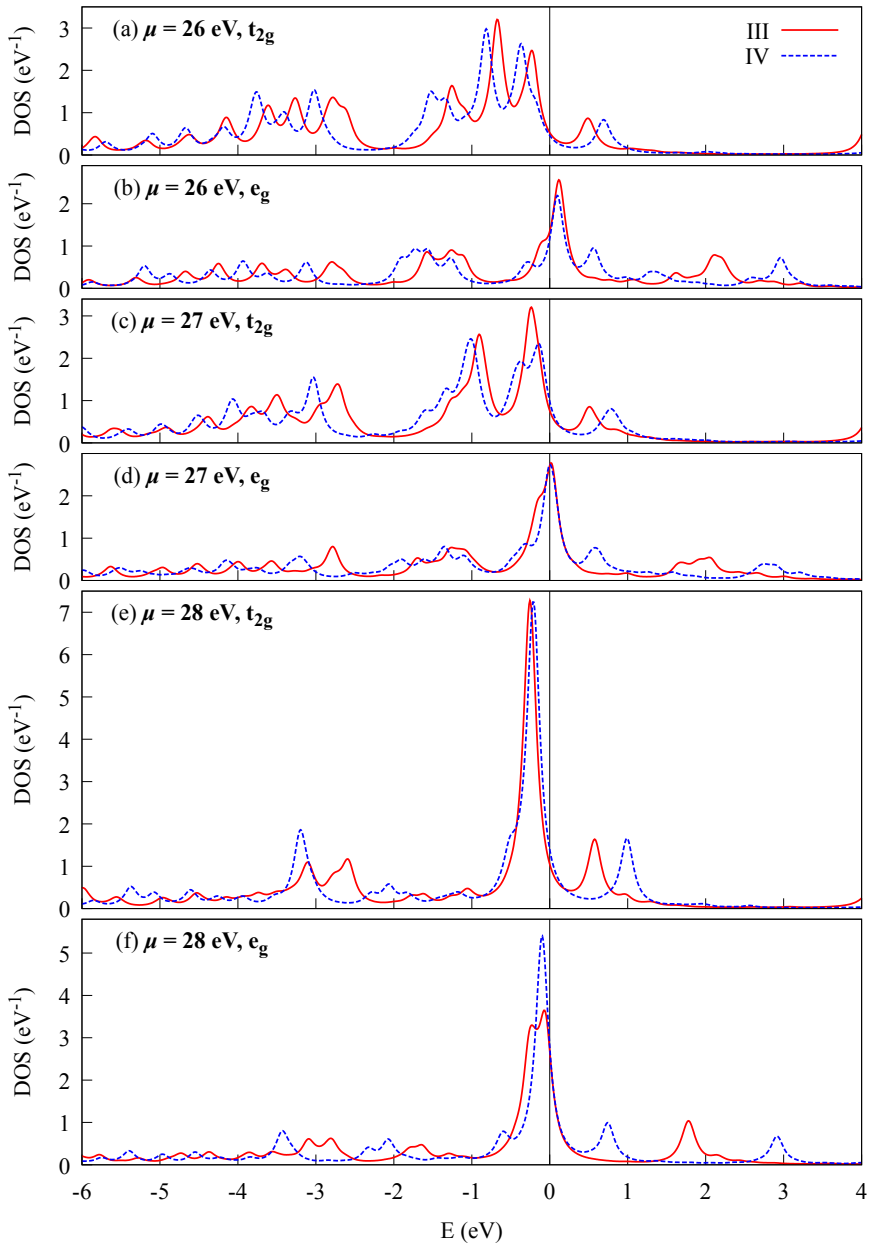

Figure 3.4: Density of states of the t_{2g} and e_g orbitals for model III and IV, for μ values of 26 eV, 27 eV and 28 eV. Lorentzian broadening with a full width at half maximum (FWHM) of 0.2 eV was applied.

the local Green's function can be rewritten as the effective Green's function of a quasi-particle whose self-energy is in on the order of ω^2:[1]

$$G^{\text{imp}}_{m\sigma}(\omega) = \frac{1}{\omega - \epsilon_m + i\Delta_{m\sigma} - \Sigma_{m\sigma}(\omega)} = \frac{Z_m}{\omega - \tilde{\epsilon}_m + i\tilde{\Delta}_{m\sigma} - \tilde{\Sigma}_{m\sigma}(\omega)}, \tag{3.6}$$

with the effective orbital energies $\tilde{\epsilon}_m = Z_m(\epsilon_m + \Sigma_{m\sigma}(0))$, hybridizations $\tilde{\Delta}_{m\sigma} = Z_m\Delta_{m\sigma}$ and self-energies $\tilde{\Sigma}_{m\sigma}(\omega) = Z_m\Sigma^{\text{rem}}_{m\sigma}(\omega)$. The parameter

$$Z_m = \left(1 - \left.\frac{\partial \text{Re}\left[\Sigma_m(\omega)\right]}{\partial\omega}\right|_{\omega=0}\right)^{-1} \tag{3.7}$$

is called the wavefunction renormalization factor, or the quasi-particle weight.

The self-energy $\Sigma_{m\sigma}(\omega)$ was computed from the Green's function of the Anderson impurity model as $\Sigma_{m\sigma}(\omega) = \omega - \left[H^{(0)}_{\text{imp}}\right]_{m\sigma} - \left[G^{-1}_{\text{imp}}(\omega)\right]_{m\sigma}$ where $H^{(0)}_{\text{imp}}$ is the impurity Hamiltonian without the Coulomb term [44].

The spectral function of each discrete model was calculated from the impurity's Green's function using Eq. (2.11) as

$$\rho^{\text{ED}}_m(\epsilon) = \frac{1}{\pi}\text{Im}\left[\text{Tr}\left[G^{\text{imp}}(\epsilon - i\delta)\right]_m\right], \tag{3.8}$$

with Lorentzian broadening of $\delta = 0.1$ eV. The spectra are depicted in Fig. 3.4. For each value of μ, the spectra of model III and IV are largely in agreement with each other.

The system's observables and quasi-particle weights as calculated by CT-QMC in Ref. [57] are shown in Tab. 3.3. For the t_{2g} states, our quasi-particle weights behave qualitatively similarly to the ones calculated by QMC, increasing with n_d. For the e_g states, the quasi-particle weight for $\mu = 27$ eV breaks the pattern, as it is slightly lower than for $\mu = 26$ eV.

A comparison of the spectral functions derived by ED and CT-QMC for $\mu = 27$ eV is shown in Fig. 3.5. The QMC DOS for each orbital contains a single smooth peak slightly below the Fermi energy. The ED spectra have peaks close to the Fermi energy as well, but they also show peaks for more distant energies. This discrepancy is expected, since the QMC peaks have been obtained by analytical continuation and thus can only be expected to be accurate close to the Fermi energy [60].

Throughout the rest of the chapter, model IV will be used.

3.2.3 Kondo effect

For the purpose of modeling the Kondo effect, a low temperature of $\beta = 500\,\text{eV}^{-1}$ (23.2 K) was set . Since the Kondo effect occurs when there is a resonance peak at the Fermi level, it can only be observed when the two sectors with the lowest

[1] The theory assumes a wide conduction band with a hybridization function independent of ω, so that it would be independent of the magnetic field. Since in our system there is no magnetic field, the wide band assumption is not necessary.

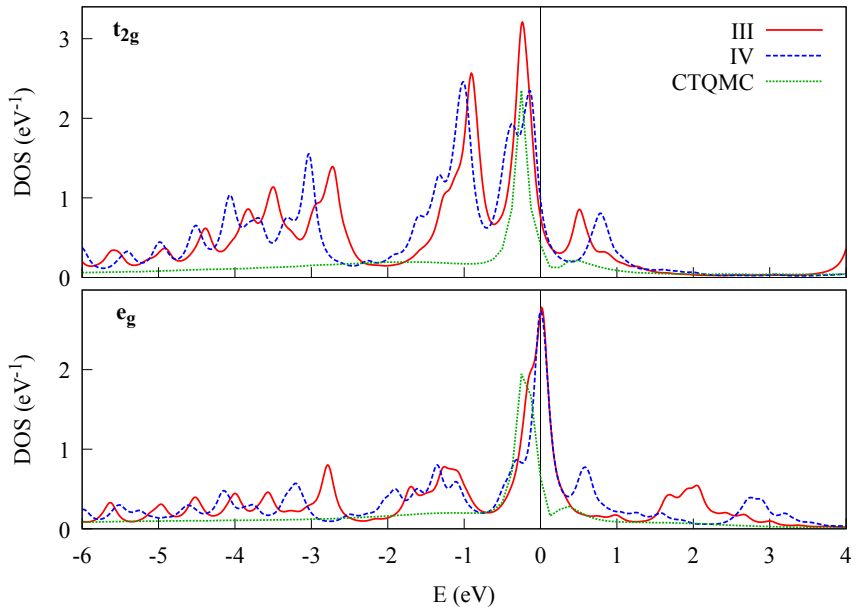

Figure 3.5: Comparison of the model IV DOS for $\mu = 27\,\text{eV}$ to the DOS derived by CT-QMC [57]. The QMC DOS has been re-scaled.

SOC (eV)	μ (eV)	N	ΔN	n_d	S	L	J
0	26	28.000	0.000	7.459	1.144	3.027	3.367
	27	28.999	0.028	7.806	0.971	2.875	3.152
	27.4	29.902	0.297	8.048	0.850	2.738	2.974
	28	30.000	0.000	8.211	0.784	2.629	2.846
0.079	26	28.000	0.000	7.462	1.138	3.031	3.749
	27	28.837	0.370	7.787	0.980	2.893	3.437
	27.5	29.516	0.500	8.011	3.164	0.873	2.761
	28	30.000	0.000	8.208	0.785	2.631	2.933

Table 3.4: The total occupation N, fluctuation ΔN, impurity occupation n_d, impurity spin S, orbital L and total moments J for $\mu = 27.4$ eV, at $\beta = 500\,\text{eV}^{-1}$, with and without SOC. μ was set so that $n_d \approx 8$.

μ (eV)	N	Energy (eV)	n_d	P_{d^6}	P_{d^7}	P_{d^8}	P_{d^9}	Multiplicity
26	28	−137.8498	7.459	0.082	0.413	0.450	0.050	4
27	28	−145.4226	7.689	0.046	0.317	0.532	0.100	4
	29	−145.4363	7.807	0.037	0.278	0.525	0.154	4
27.4	29	−148.5790	7.908	0.029	0.240	0.530	0.193	4
	30	−148.5862	8.063	0.019	0.197	0.507	0.257	1
		−148.1052	7.946	0.021	0.224	0.549	0.200	3
28	30	−153.4686	8.212	0.013	0.152	0.480	0.321	1
		−152.9139	8.083	0.015	0.176	0.532	0.268	3

Table 3.5: Impurity occupation numbers for the lowest eigen-energies of every sector, for different chemical potentials, without SOC.

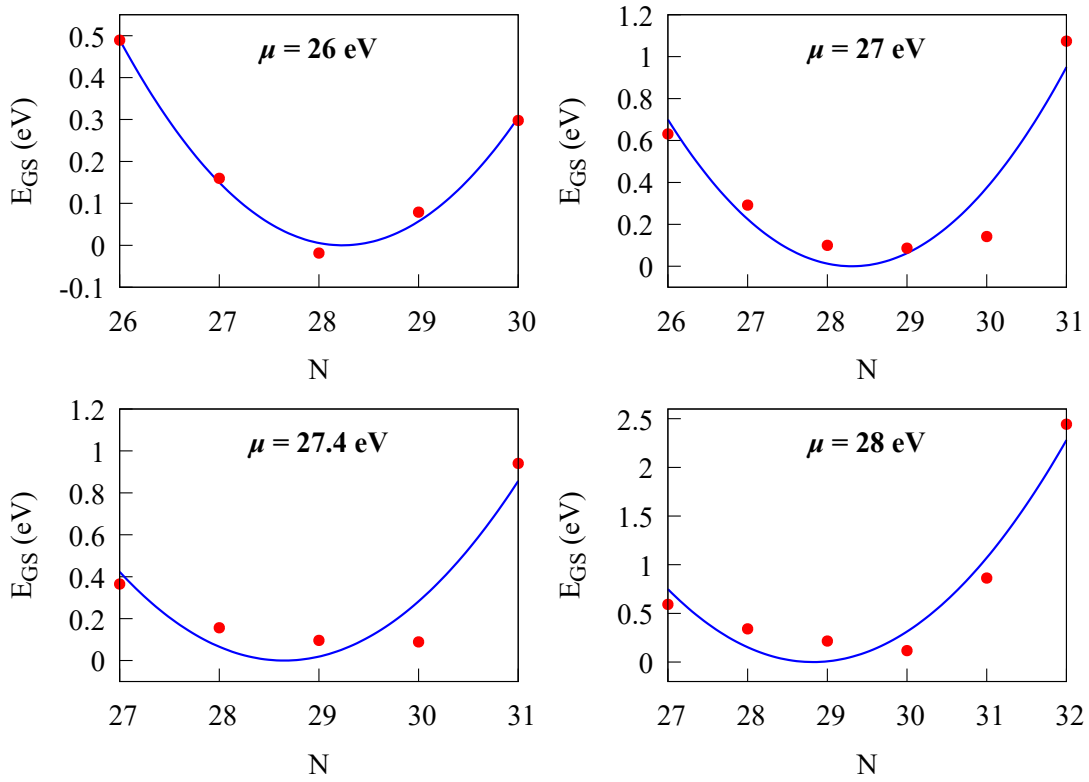

Figure 3.6: ground-state energy of a sector E_{GS} vs. the sector's population N, for multiple values of μ.

ground-state energies have ground-state energies that are very close to each other, as indicated by Eq. (2.61) for $\alpha = \alpha' = 0$. For this purpose, the chemical potential is adjusted to $\mu = 27.4$. The observables for this value are shown in Tab. 3.4. It can be seen that n_d is approximately equal to 8, in accordance to the DFT+QMC calculations in Ref. [57].

Fig. 3.6 shows the lowest energy per sector for each value of μ. The dependence in each model is roughly quadratic, since the leading energy terms are the chemical potential, which rises linearly with the number of particles, and the coupling energy, which is proportional to the number of electron–electron interactions [61]:

$$E\left(N\right) = -\mu N + \frac{U}{2} N\left(N-1\right). \tag{3.9}$$

Fig. 3.6 gives insight into the observed total population N shown in Tab. 3.4. For $\mu = 26\,\mathrm{eV}$, the system's ground state is $|\Omega_{28,0}\rangle$. The second-lowest state in the ensemble, $|\Omega_{29,0}\rangle$ is ~0.1 eV away from the ground state, well above the excitation range of about $1/\beta = 0.002\,\mathrm{eV}$ for the temperature of $\beta = 500\,\mathrm{eV}^{-1}$. For this reason, The observed total occupation is exactly $N = 28$, with zero fluctuation (in comparison, for $\beta = 40\,\mathrm{eV}^{-1}$ the excitation range is $1/\beta = 0.025\,\mathrm{eV}$, so the fluctuation has a relatively large size, as seen in Tab. 3.2). For $\mu = 28\,\mathrm{eV}$, the ground state is likewise a pure state, and the observed total occupation is $N = 30$. For $\mu = 27\,\mathrm{eV}$, the states and $|\Omega_{28,0}\rangle$ and $|\Omega_{29,0}\rangle$ are in resonance with each other, as evident by the DOS in Fig. 3.4 having a peak at Fermi energy. Due to the resonance, the fluctuation ΔN for $\mu = 27\,\mathrm{eV}$ is nonzero even at a low temperature.

μ	N	Energy (eV)	S_z	L_z	J_z
26	28	−137.8498	0.9203	0.0158	0.9361
		−137.8498	0.0000	0.0000	0.0000
		−137.8498	−0.9203	−0.0158	−0.9361
27	28	−145.4226	0.8298	0.0174	0.8472
		−145.4226	0.0000	0.0000	0.0000
		−145.4226	−0.8298	−0.0174	−0.8472
	29	−145.4363	0.5457	0.0174	0.5631
		−145.4363	0.5457	0.0013	0.5470
		−145.4363	−0.5457	−0.0013	−0.5470
		−145.4363	−0.5457	−0.0174	−0.5631
27.4	29	−148.5790	0.5199	0.0181	0.5380
		−148.5790	0.5199	0.0010	0.5209
		−148.5790	−0.5199	−0.0010	−0.5209
		−148.5790	−0.5199	−0.0181	−0.5380
	30	−148.5862	0.0000	0.0000	0.0000
		−148.1052	0.5232	0.0086	0.5318
		−148.1052	0.0000	0.0000	0.0000
		−148.1052	−0.5232	−0.0086	−0.5318
28	30	−153.4686	0.0000	0.0000	0.0000
		−152.9139	0.5091	0.0093	0.5185
		−152.9139	0.0000	0.0000	0.0000
		−152.9139	−0.5091	−0.0093	−0.5185

Table 3.6: The energies and spin values for the ground states for various values of μ, with no SOC.

For $\mu = 27.4\,\text{eV}$, the resonance is between $|\Omega_{29,0}\rangle$ and $|\Omega_{30,0}\rangle$, and $\Delta N = 0.297$, a high value (for comparison, the highest possible fluctuation value is 0.5).

Tab. 3.6 shows the lowest eigen-energies per sector and and the spin (S_z), orbit (L_z) and total (J_z) observables of each state ($\langle\Omega_{N\alpha}|\,\hat{O}\,|\Omega_{N\alpha}\rangle$), for each chemical potentials. Though the eigenvalues of each sector's ground state have different energies and moments for different values of μ, their qualitative structure is the same. The ground state of the $N = 28$ sector is a degenerate triplet, and the ground state of the $N = 29$ sector is a degenerate quadruplet. The ground state of the $N = 30$ sector is a singlet, and the first excitation is a triplet that is excited by roughly 0.5 eV. The spin moment is approximately 0.5, and the orbital moment is negligible. This structure corresponds to solution of the Kondo model for a localized $S = 1/2$ spin anti-ferromagnetically coupled to a single band of conduction electrons, as described in Sec. 3.1.

The calculations were performed with a SOC of $\xi = 0.079\,\text{eV}$ as well. The observabled occupations and moments are shown in Tab. 3.4. The chemical potential corresponding to $n_d \approx 8$ shifted to $\mu = 27.5$ eV. The qualitative behavior of the observables is similar to the case without SOC, other than the spin for

μ	N	Energy (eV)	S_z	L_z	J_z
27.5	29	−149.4050	0.4724	0.8453	1.3178
		−149.4050	0.3823	0.1446	0.5268
		−149.4050	−0.3823	−0.1446	−0.5268
		−149.4050	−0.4724	−0.8453	−1.3178
	30	−149.4067	0.0000	0.0000	0.0000
		−148.9334	0.4512	0.4907	0.9419
		−148.9334	0.0000	0.0000	0.0000
		−148.9334	−0.4512	−0.4907	−0.9419

Table 3.7: The energies and spin values for the ground states of model IV for $\mu = 27.5$ at room temperature ($\beta = 40\,\mathrm{eV}^{-1}$), with a SOC of 0.079 eV.

μ (eV)	N	Energy (eV)	n_d	P_{d^6}	P_{d^7}	P_{d^8}	P_{d^9}	Multiplicity
26	28	−137.8932	7.462	0.081	0.412	0.452	0.049	3
27	28	−145.4678	7.689	0.046	0.317	0.535	0.098	3
	29	−145.4704	7.807	0.037	0.278	0.526	0.153	4
27.5	29	−149.4050	7.933	0.027	0.230	0.531	0.202	4
	30	−149.4067	8.085	0.018	0.190	0.505	0.266	1
		−148.9334	7.970	0.020	0.214	0.549	0.211	3
28	30	−153.4799	8.208	0.013	0.153	0.482	0.320	1
		−152.9471	8.085	0.014	0.175	0.533	0.268	3

Table 3.8: Impurity occupation numbers for the lowest eigen-energies of every sector, for different chemical potentials, for a SOC of 0.079 eV.

$\mu = 27.5$ eV being significantly higher than for $\mu = 27.4$ eV without SOC, and the orbital being significantly lower.

Tab. 3.7 shows the lowest eigen-energies per sector and the observables S_z, L_z, J_z for each state for $\xi = 0.079\,\mathrm{eV}$ and $\mu = 27.5$ eV, similarly to Tab. 3.6. It can be seen that for the $N = 30$ sector, spin is no longer a good quantum number, since there is a significantly large orbital moment.

The energies and impurity occupation probability weights of the lowest eigen-states for every sector included in the grand-canonical calculations are shown in of Tab. 3.8, alongside their zero SOC counterparts. As can be seen, the effect of SOC on the occupations is negligible.

Fig. 3.7 shows the local DOS for $CoCu_{15}$ at $\beta = 500\,\mathrm{eV}^{-1}$, for the cases with and without SOC for which a resonance occurs at Fermi energy. The imaginary additive was set to $\eta = 6.28 \cdot 10^{-3}$. It can be seen that in both systems there is a peak close to Fermi energy. As inferred from Lehman's representation of the spectral function in Eq. (2.61), those peaks correspond to transitions between sectors (the addition or the removal of an electron). In this case, the peaks correspond to the $30 \to 29$ transition resonance. This, together with the ground state singlet in both systems, indicates the presence of a Kondo singlet state.

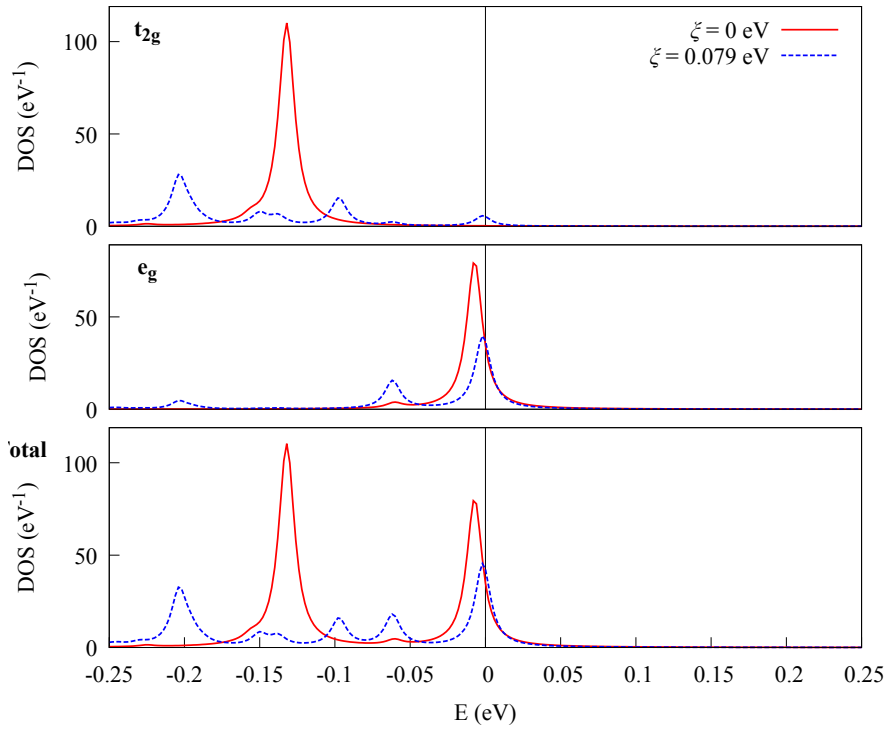

Figure 3.7: DOS for $CoCu_{15}$ at a low temperature ($\beta = 500\,\mathrm{eV}^{-1}$) for $\mu = 27.4\,\mathrm{eV}$ without SOC and for $\mu = 27.5\,\mathrm{eV}$ with a SOC of 0.079 eV.

3.3 A cobalt atom on a copper surface

3.3.1 Setup, DFT and fitting

The material under study consists of a copper crystal with the same *fcc* structure as in the previous section, and a cobalt atom situated on top of the surface between four copper atoms. The DFT calculations were performed on a supercell of four layers of Cu(100) on which the cobalt atom is situated, followed by empty space in the size of four copper layers above it. The system is depicted in Fig. 3.8, along with the x and y axes of the chosen axis system. The z axis is perpendicular to the plane.

This system has a lower symmetry than the system of a cobalt atom in bulk copper, since the z axis is now distinguishable from the x and y axes, while the chosen x and y axes are indistinguishable. The system exhibits a C_{4v} crystal symmetry which induces degeneracy between the xz and yz orbitals. There are thus four distinct orbitals — yz, xy, $x^2 - y^2$, $3z^2 - r^2$.

Partial structure relaxation was performed in VASP [62] together with the generalized gradient approximation (GGA) to spin-polarized DFT without SOC. The relaxed parameters were the atomic positions of the cobalt adatom and the two upper layers of copper. The relaxed distance between the cobalt adatom and the first Cu substrate layer was found to be 2.91 a.u., in a good agreement with previously reported value of 2.87 a.u. [63]. Afterwards, the DOS has been calculated in VASP. The orbitally resolved DOS is shown in Fig. 3.10.

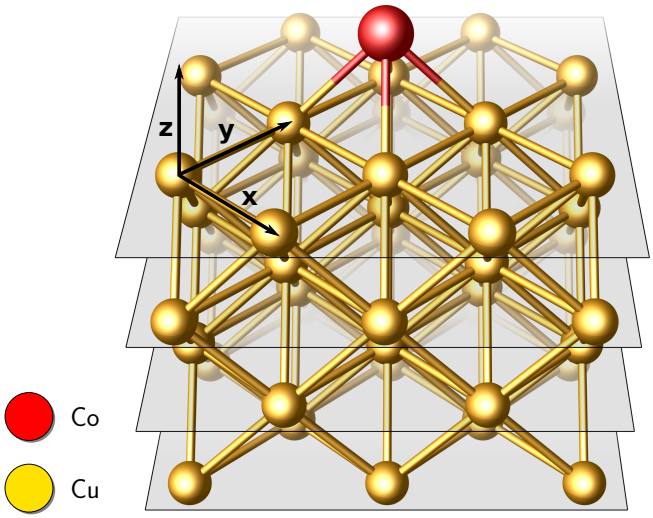

Figure 3.8: Model of the supercell of cobalt on Cu(100). The x and y axes of the coordinate system are depicted.

m	yz,xz	xy	x^2-y^2	$3z^2-r^2$
Δ_{CF}	-0.043	0.117	0.053	-0.082
$\epsilon_{m,k=1}$	-2.16	-1.99	-2.01	-2.57
$V_{m,k=1}$	0.85	0.65	0.65	0.72
$\epsilon_{m,k=2}$	-0.08	0.001	-0.02	-0.05
$V_{m,k=2}$	0.18	0.08	0.10	0.13
$\epsilon_{m,k=3}$	0.51	1.45	0.53	0.43
$V_{m,k=3}$	0.36	0.55	0.34	0.32
$\epsilon_{m,k=4}$	7.56	7.80	8.16	7.72
$V_{m,k=4}$	2.08	2.12	1.78	1.70

Table 3.9: Values of the bath parameters ϵ_{mk} and V_{mk} for cobalt on Cu(100), obtained by fitting the hybridization function obtained from DFT. (right).

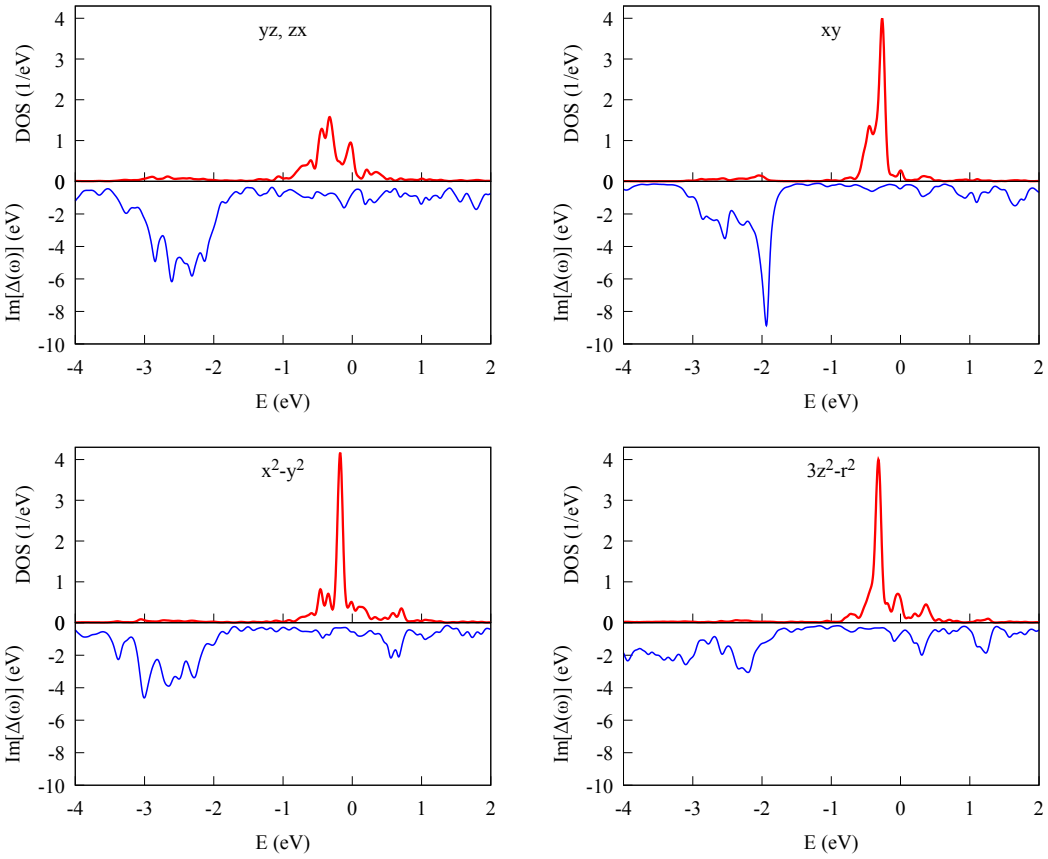

Figure 3.9: Orbitally resolved DOS and imaginary part of real-frequency hybridization function for Co@Cu(100) for each orbital.

$\xi = 0.0\,\text{eV}$

μ (eV)	$\langle N \rangle$	ΔN	n_d	S	L	J	P_{d^6}	P_{d^7}	P_{d^8}	P_{d^9}
27	26.00	0.01	7.74	1.03	3.01	3.32	0.03	0.27	0.62	0.08
27.4	26.55	0.50	7.93	0.94	2.87	3.15	0.02	0.21	0.58	0.18
27.5	27.00	0.02	8.03	0.89	2.79	3.04	0.02	0.19	0.55	0.24
28	27.00	0.00	8.17	0.82	2.68	2.91	0.01	0.14	0.51	0.33

$\xi = 0.079\,\text{eV}$

μ (eV)	$\langle N \rangle$	Var $[N]$	n_d	S	L	J	P_{d^6}	P_{d^7}	P_{d^8}	P_{d^9}
27	26.00	0.00	7.75	1.03	3.01	3.82	0.03	0.26	0.62	0.08
27.5	26.00	0.02	7.87	0.97	2.93	3.68	0.02	0.22	0.62	0.14
27.6	26.38	0.48	7.96	0.93	2.86	3.51	0.02	0.20	0.58	0.19
28	27.00	0.00	8.17	0.82	2.68	3.16	0.01	0.14	0.51	0.33

Table 3.10: The total occupation $\langle N \rangle$, fluctuation ΔN, impurity occupation $\langle n_d \rangle$, angular momentum observables S, L, J and non-zero probability weights per impurity occupation as functions of μ, for SOC values of 0 eV (top) and 0.079 eV (bottom), calculated by exact diagonalization.

3.3.2 Exact diagonalization

Exact diagonalization was performed using an excitation cutoff of 4, for several chemical potentials ranging between 26 eV to 28 eV, with SOC and without it. As with $CoCu_{15}$, the spin-orbit coupling was chosen to be $\xi = 0.079\,\text{eV}$ using the method shown in Sec. 2.3. For each system, the total occupation $\langle N \rangle$, fluctuation ΔN, impurity occupation $\langle n_d \rangle$ and the angular momentum observables S, L, J were measured at a low temperature of $\beta = 500\,\text{eV}^{-1}$. The observables measured for each model, along with the probability weights P_{d^6} to P_{d^9}, are shown in Tab. 3.10.

For $\mu = 27\,\text{eV}$, the system's ground state is $|\Omega_{26,0}\rangle$, the ground state of the pure $N = 26$ sector, as evident from the integer total occupation and zero variance. The main contributions to the impurity's occupation come from the P_{d^8} (which has a spin value of $S = 1$) and P_{d^7} ($S = \frac{3}{2}$) states. Accordingly, the observed spin is between 1 and $\frac{3}{2}$. For $\mu = 28\,\text{eV}$, the ground state is $|\Omega_{27,0}\rangle$, again with no state mixing. Compared to $\mu = 27\,\text{eV}$, the impurity occupation has less contribution from P_{d^7} and P_{d^8} and more from P_{d^9} ($S = \frac{1}{2}$). We expect a Kondo state to have a large contribution from the P_{d^8} state, since its spin value of $S = 1$ is capable of producing a singlet.

Since the resonance we're looking for occurs in a mixed state, we calibrate the chemical potential to value between 27 eV and 28 eV where significant fluctuation is detected. We find resonance close to $\mu = 27.5\,\text{eV}$: $\mu = 27.4\,\text{eV}$ for $\xi = 0\,\text{eV}$ and $\mu = 27.6\,\text{eV}$ for $\xi = 0.079\,\text{eV}$. Both of those systems have a fluctuation value

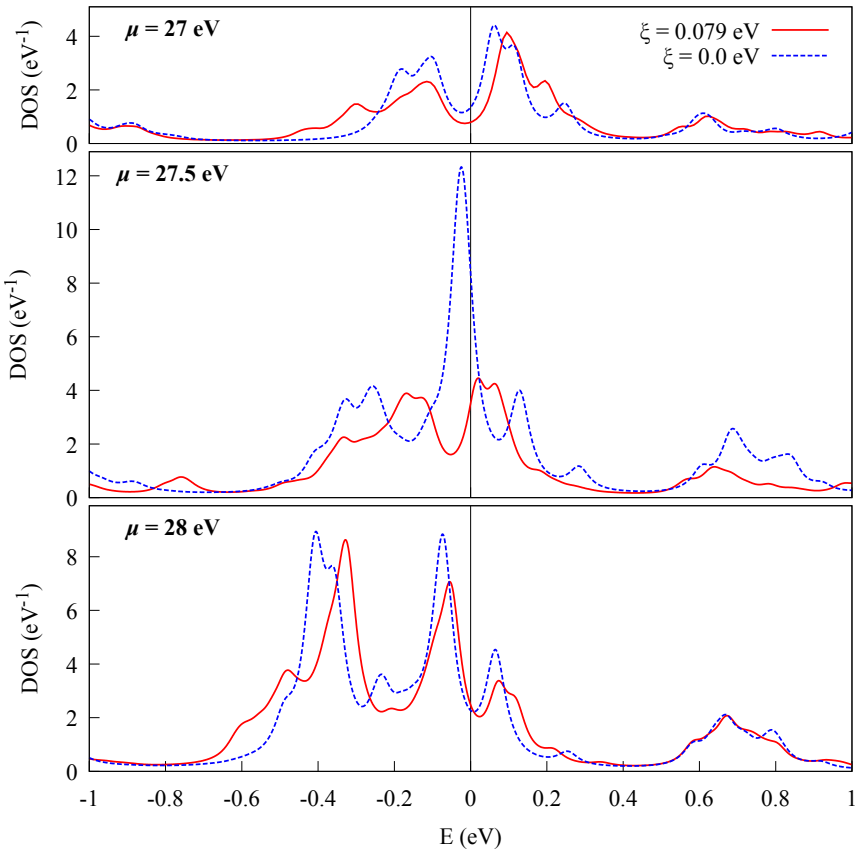

Figure 3.10: The total DOS for of a cobalt adatom on Co@Cu(100) with and without SOC, for chemical potentials of 27 eV, 27.5 eV and 28 eV.

of Var $[N] = 0.5$. For chemical potential values close to 27.5 eV, the impurity occupation is close to 8.

The DOS for chemical potentials 27 eV and 28 eV is shown in Fig. 3.10. Neither has a resonance peak near the Fermi energy, with or without SOC, which indicates the lack of Kondo resonance. The DOS for the intermediate chemical potentials is shown in Fig. 3.11. We find that for $\mu = 27.5$ eV there is a resonance peak close to Fermi level — below Fermi level for $\xi = 0.0$ eV and above for $\xi = 0.079$ eV. For, the adjusted chemical potentials, $\mu = 27.4$ eV for $\xi = 0$ eV and $\mu = 27.6$ eV for $\xi = 0.079$ eV, there is a peak right on the Fermi level. In Ref. [63], CT-QMC calculations in Co@Cu (100) with an occupation of $n_d = 8$ and the same choice of Coulomb and exchange potentials have also detected a resonance peak near Fermi level in the spectral function, which was interpreted as Kondo resonance.

The energies and measured angular momentum observables S_z, L_z, J_z for each model are shown in Tab. 3.11. When there is no SOC, the $|\Omega_{26,0}\rangle$ ground state is a degenerate triplet (with $J = 1$), and $|\Omega_{27,0}\rangle$ ground state is a degenerate doublet (with $J = \frac{1}{2}$). For $\mu = 27.4$ eV, the ground state is a mixture of both, and the difference in energies between the two is only 1.2 meV, close enough for resonance. Nevertheless, the lack of a singlet state indicates that no Kondo resonance is taking place.

$\xi = 0\,\mathrm{eV}$

μ (eV)	N	Energy (eV)	S_z	L_z	J_z
27	26	−142.2319	0.0000	0.0000	0.0000
		−142.2319	0.8847	0.0222	0.9069
		−142.2319	−0.8847	−0.0222	−0.9069
27.4	26	−145.3478	0.0000	0.0000	0.0000
		−145.3478	0.8343	0.0216	0.8127
		−145.3478	−0.8343	−0.0216	−0.8127
	27	−145.3490	0.5736	0.0222	0.5514
		−145.3490	−0.5736	−0.0222	−0.5514
28	27	−150.1992	0.5354	0.0220	0.5134
		−150.1992	−0.5354	−0.0220	−0.5134

$\xi = 0.079\,\mathrm{eV}$

μ (eV)	N	Energy (eV)	S_z	L_z	J_z
27	26	−146.2063	0.0000	0.0000	0.0000
		−146.2023	1.4788	0.9074	0.5714
		−146.2023	−1.4788	−0.9074	−0.5714
27.6	26	−146.9950	0.0000	0.0000	0.0000
		−146.9912	1.1040	0.6992	0.4048
		−146.9912	−1.1040	−0.6992	−0.4048
	27	−146.9931	1.4289	0.9467	0.4822
		−146.9931	−1.4289	−0.9467	−0.4822
28	27	−150.2373	1.3645	0.9117	0.4528
		−150.2373	−1.3645	−0.9117	−0.4528

Table 3.11: The energies and angular momentum values for the ground states and lowest excitations for various values of μ, for SOC values of 0 eV (top) and 0.079 eV (bottom).

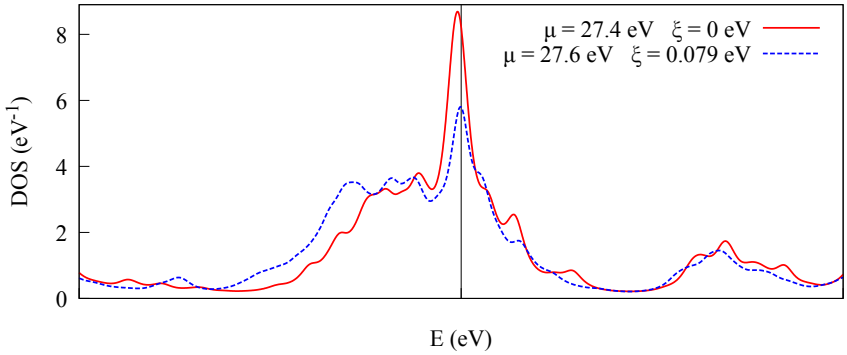

Figure 3.11: The total DOS for of a cobalt adatom on Co@Cu(100) without SOC for $\mu = 27.4\,\text{eV}$ and with SOC for $\mu = 27.5\,\text{eV}$.

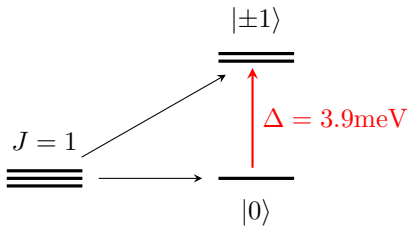

Figure 3.12: Splitting of the effective spin $J = 1$ triplet by SOC for $\mu = 27.6\,\text{eV}$.

When SOC is present, the triplet's energy creates an energy gap between the $J_z = 0$ state and the $J_z = \pm 1$ states. This indicates that the magnetic anisotropy can be modeled using the effective Hamiltonian

$$\hat{H}_{\text{MA}} = D\hat{J}_z^2. \tag{3.10}$$

The splitting is portrayed in Fig. 3.12 For $\mu = 27.6\,\text{eV}$, it is a 3.9 meV gap, compared to the 1.9 meV difference between the singlet state and the $|\Omega_{27,0}\rangle$ ground state. This indicates the presence of Kondo resonance.

3.3.3 Differential conductance

The DFT+ED model can be evaluated by comparing its observable properties to experimental data. Experimental exploration of adatom systems is performed using spin tunneling spectroscopy (STS) measurements. In an STS experiment, a conducting tip is placed close to the adatom, a bias voltage V is applied between the tip and the sample and the tunneling current I is measured [58]. The measurement's results usually come in the form of the differential conductance $\frac{\mathrm{d}I}{\mathrm{d}(eV)}$ (the nonlinear extension of classical conductance $G = \frac{I}{V}$) plotted against the bias eV. This plot allows identifying the various channels that contribute to the conductance.

The STS measurements for Co@Cu(100) are shown in Ref. [58]. The tunneling spectrum takes an asymmetric Fano line shape, which occurs due to Abrikosov-Suhl-Kondo resonance — interference between the tip-adatom tunneling and the tip-substrate tunneling [64]. The strength of the resonance for each spin-orbital is characterized by the Fano parameter

$$q_{m\sigma}(\epsilon) = \frac{t_{m\sigma} + w_{m\sigma} V \mathrm{Re}\left[G^{\mathrm{bath}}_{m\sigma}(\epsilon)\right]}{\pi w_{m\sigma} V \rho^{\mathrm{bath}}_{m\sigma}(\epsilon)} \tag{3.11}$$

where $t_{m\sigma}$ is the tip-adatom tunneling coefficient, $w_{m\sigma}$ is the tip-substrate tunneling coefficient, and $G^{\mathrm{bath}}_{m\sigma}(\omega)$ and $\rho^{\mathrm{bath}}_{m\sigma}(\omega)$ are the bath's Green's function and DOS respectively. In terms of the bath energies ϵ_{mk} from Eq. (2.43),

$$G^{\mathrm{bath}}_{m\sigma}(\epsilon) = \sum_{mk} \frac{1}{\epsilon - \epsilon_{mk} + i\eta}, \tag{3.12}$$

$$\rho^{\mathrm{bath}}_{m\sigma}(\epsilon) = -\frac{1}{\pi}\mathrm{Im}\left[G^{\mathrm{bath}}_{m\sigma}(\epsilon)\right]. \tag{3.13}$$

For the strongly localized d-orbitals, the Fano parameter can be approximated to its value in the vicinity of the Fermi energy [65]. In the limit of $w_{m\sigma} \gg t_{m\sigma}$, the Fano parameter is independent of both tunneling coefficients:

$$q_{m\sigma}(E_F) = -\frac{\mathrm{Re}\left[G^{\mathrm{bath}}_{m\sigma}(E_F)\right]}{\mathrm{Im}\left[G^{\mathrm{bath}}_{m\sigma}(E_F)\right]}. \tag{3.14}$$

The Fano line shap of differential conductance in an STS system is derived in Ref. [66] using a non-equilibrium Green's function method. The theory uses the Tersoff and Hamann model [67], which assumes the tip to be a single atom with only an s-shell. The bias V is assumed to be small compared to the tunnelling barrier. The differential conductance is

$$\frac{\mathrm{d}I(\epsilon)}{\mathrm{d}(eV)} = \sum_{m\sigma} \mathrm{G}_\sigma \left(1 + Y_{m\sigma}(\epsilon)\right), \tag{3.15}$$

where the transition intensity is

$$Y_{m\sigma}(\epsilon) = \Gamma_{m\sigma}(E_F)\left(\left(1 - q^2_{m\sigma}\right)\mathrm{Im}\left[G^d_{m\sigma}(\epsilon)\right] + 2q_{m\sigma}\mathrm{Re}\left[G^d_{m\sigma}(\epsilon)\right]\right). \tag{3.16}$$

$\Gamma_{m\sigma}(\epsilon) = -\mathrm{Im}\left[\Delta_{m\sigma}(E_F)\right]$ is the level-broadening caused by hybridization between the impurity and the surface. The tip-substrate conductance G_σ is treated as independent of spin and can be ignored.

In order to highlight the Fano line shape, the energy of each orbital can be rescaled as

$$\tilde{\epsilon}_{m\sigma} \equiv \frac{\epsilon - \epsilon_{m\sigma} + \mathrm{Re}\left[\Sigma_{m\sigma}(\epsilon)\right]}{\mathrm{Im}\left[\Sigma_{m\sigma}(\epsilon)\right]}, \tag{3.17}$$

where $\epsilon_{m\sigma}$ is the occupation energy of orbital m and $\Sigma_{m\sigma}(\epsilon)$ is the impurity's self-energy. The differential conductance is then [64]

$$\frac{\mathrm{d}I(\epsilon)}{\mathrm{d}(eV)} \sim \sum_{m\sigma} \frac{\left(\tilde{\epsilon}_{m\sigma}(\epsilon) + q_{m\sigma}\right)^2}{\tilde{\epsilon}^2_{m\sigma}(\epsilon) + 1}. \tag{3.18}$$

Fig. 3.13 depicts the calculated differential conductance in the vicinity of the Fermi energy. It can be seen that the predicted differential conductance is qualitatively similar in shape to the experimental one.

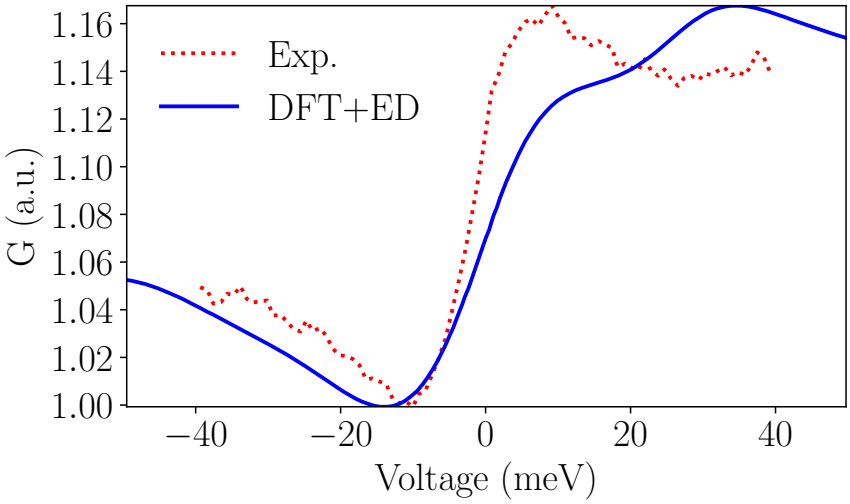

Figure 3.13: Simulated differential conductance, plotted against the STS spectrum from Ref. [58], using arbitrary units.

m	yz,xz	xy	x^2-y^2	$3z^2-r^2$
Δ_{CF}	0.028	0.039	-0.076	−0.019
$\epsilon_{m,k=1}$	-3.78	-3.86	-3.44	−3.57
$V_{m,k=1}$	1.43	1.87	1.37	1.53
$\epsilon_{m,k=2}$	-0.60	-0.72	-0.70	−0.53
$V_{m,k=2}$	0.44	0.62	0.63	0.30
$\epsilon_{m,k=3}$	0.06	0.10	0.06	0.06
$V_{m,k=3}$	0.17	0.21	0.16	0.13
$\epsilon_{m,k=4}$	1.53	2.86	1.76	3.69
$V_{m,k=4}$	0.61	1.81	0.64	0.96

Table 3.12: Values of the bath parameters ϵ_{mk} and V_{mk} obtained by fitting the hybridization function obtained from DFT.

3.4 A cobalt atom on a surface of $Cu_2N/Cu\,(001)$

3.4.1 Setup, DFT and fitting

The modeled material is a supercell of three Cu(001) layers, a Cu_2N-(2×2) monolayer, and a cobalt adatom placed on a copper ion. Above the material there is vacuum with the height of four layers of copper. It is depicted in Fig. 3.14. Similarly to Co on Cu, the material does not exhibit cubic symmetry in relation to the adatom. However, if choosing a Cartesian coordinate system where the x and y axes are both at an angle of 45 degrees to the vectors that span the Cu_2N layer, the system becomes physically symmetrical to transformation between them. Like with copper on bare Cu(001), there are four distinct orbitals — yz, xy, x^2-y^2, $3z^2-r^2$.

The DFT calculation was performed using FLAPW with LDA, without the inclusion of spin.

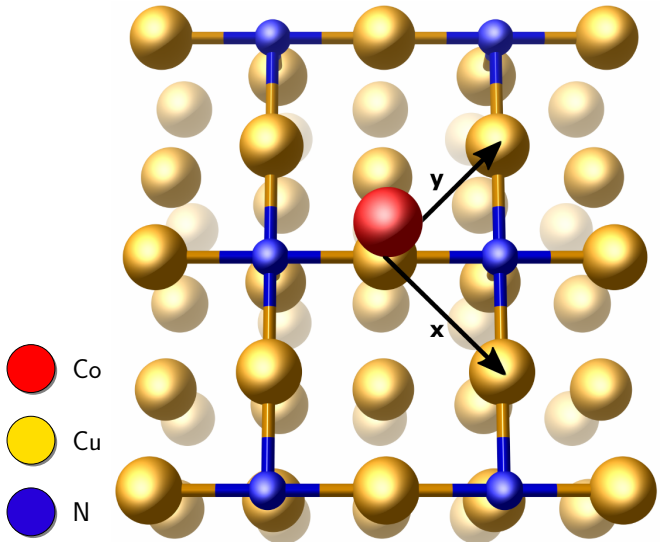

Figure 3.14: Model of the supercell of Co@Cu_2N/Cu (001). The x and y axes of the coordinate system are depicted. The z axis is perpendicular to the plane.

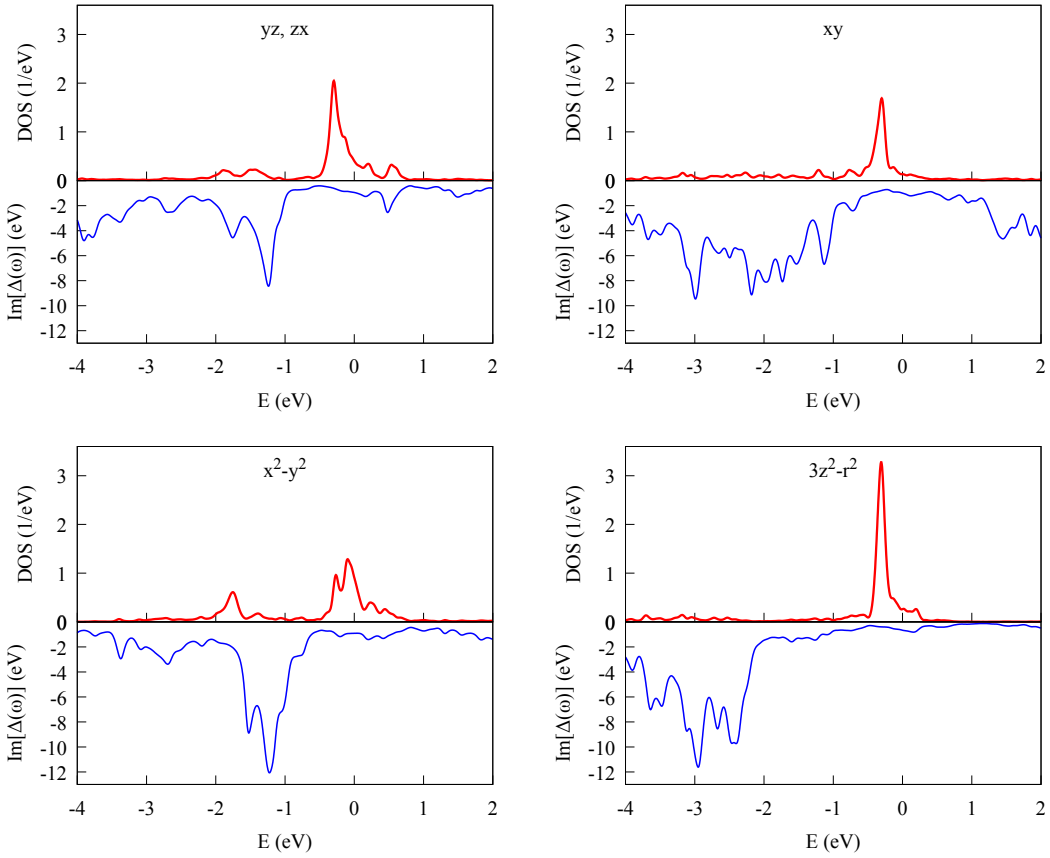

Figure 3.15: Orbitally resolved DOS and imaginary part of real-frequency hybridization function for Co@Cu_2N/Cu (001) for each orbital.

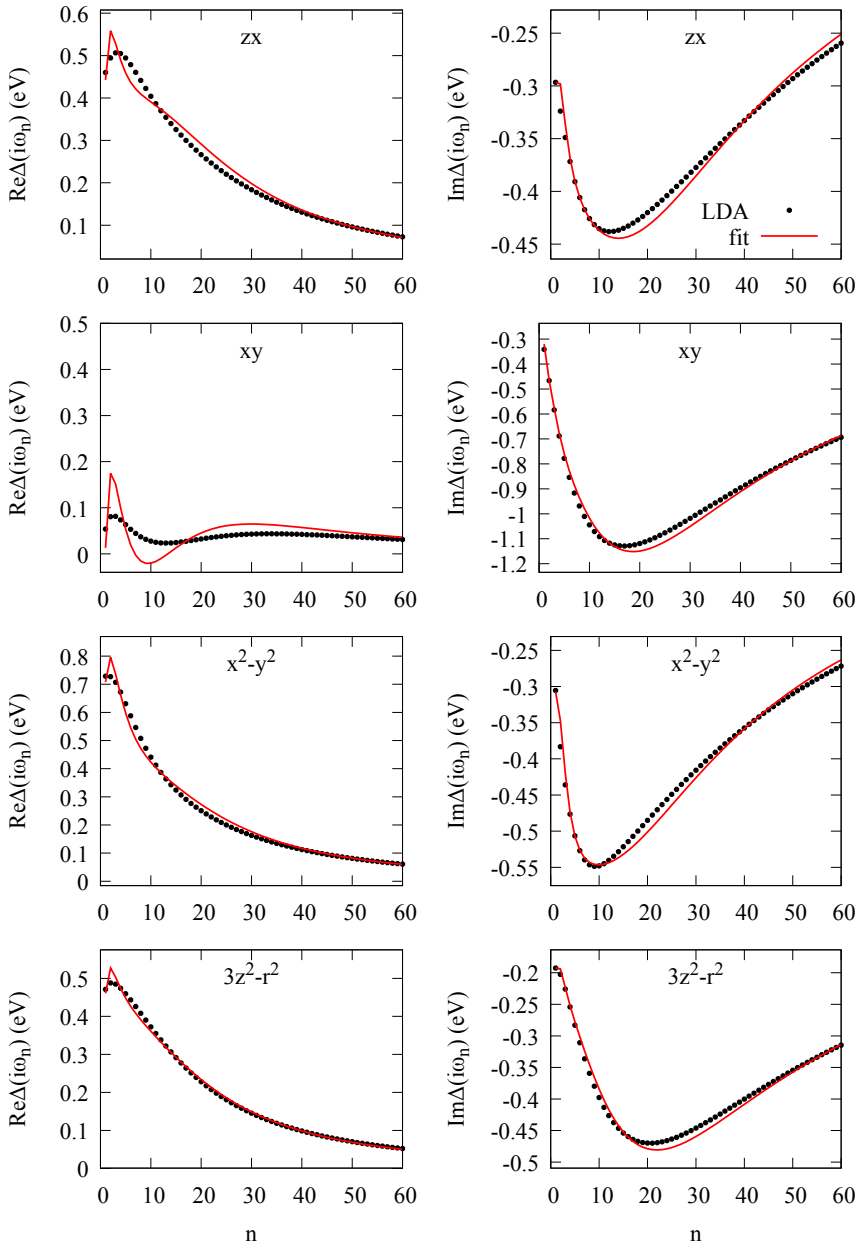

Figure 3.16: Fit of the discrete bath impurity model Eq. (2.49) to the DFT hybridization function Eq. (2.45) via minimization of the function in Eq. (2.50), using the bath parameters in Tab. 3.12.

ξ (eV)	μ (eV)	$\langle N\rangle$	ΔN	n_d	S	L	J
0	25	27.00	0.00	7.074	1.38	2.94	3.41
	26	27.00	0.00	7.289	1.29	2.94	3.36
	27	28.00	0.00	7.697	1.07	2.97	3.82
0.079	25	27.00	0.00	7.07	1.38	2.95	3.96
	26	27.76	0.43	7.40	1.21	2.98	3.90
	27	28.00	0.00	7.70	1.07	2.97	3.82

Table 3.13: The total occupation $\langle N\rangle$, fluctuation ΔN, impurity occupation $\langle n_d\rangle$ and impurity spin as functions of μ, calculated by exact diagonalization.

The discrete bath was chosen to have $N_k = 4$. The fitted hybridization function is shown in Fig. 3.16, and the calculated bath parameters are shown in Tab. 3.12. As with $CoCu_{15}$, there are 20 bath sites below Fermi level.

3.4.2 Exact diagonalization

Exact diagonalization was performed with an excitation cutoff of 4. Three chemical potential values were used — 25 eV, 26 eV and 27 eV. Spin-orbit coupling was set to $\xi = 0.079\,\text{eV}$. For the purpose of comparison, the calculations were also performed for zero SOC.

Tab. 3.13 shows the total electron occupation $\langle N\rangle$, fluctuation ΔN, impurity occupation $\langle n_d\rangle$ and expectation values for the spin (S), orbital (L) and total (J) moments at the low temperature of $\beta = 500\,\text{eV}^{-1}$.

Tab. 3.14 shows the lowest eigen-energies for each sector that significantly contribute to the ground state for every μ value, and the corresponding non-negligible probabilities for each occupation number of the impurity. Focusing on the case with SOC, For $\mu = 25\,\text{eV}$, the ground state is a doublet which is a predominantly d^7 state with non-integer valence ($n_d = 7.07$) due to hybridization with the substrate. For $\mu = 27\,\text{eV}$, the ground state is a singlet which is a predominantly d^8 state. For $\mu = 26\,\text{eV}$, the singlet and the doublet's energies are very close to each other — the gap is of 3.4 meV, in the same order of magnitude as the temperature (2 meV), which enables the charge fluctuation.

When looking at the case without SOC, in comparison, the ground state for $\mu = 26\,\text{eV}$ and $N = 27$ is a quadruplet, and the lowest two states for $\mu = 27\,\text{eV}$ have a negligible gap between them, so the ground state is effectively a triplet.

The lowest energy as a function of N for $\mu = 26\,\text{eV}$ and $\xi = 0.079\,\text{eV}$ is shown in Fig. 3.17. This dependence roughly quadratic, as described by Eq. (3.9). The minimum corresponds to a non-integer occupation of $N_{GS} = 27.85$ (The observed occupation, for comparison, is $\langle N\rangle = 27.76$).

The spectral functions of each of the models are shown in Fig. 3.18. The imaginary additive used is the smallest one allowed for this quantization in accordance with Sec. 2.5.2.1 — 0.00314 eV. For $\mu = 26\,\text{eV}$ with SOC there is a resonance peak at Fermi energy. The occupation observables in Tab. 3.13 allow us to identify the resonance peaks. The total occupation for $\mu = 26\,\text{eV}$ is a number between 27 and 28, indicating that the resonance peak on the Fermi energy corresponding to the transition from $|\Omega_{28,0}\rangle$ to $|\Omega_{27,0}\rangle$. For $\mu = 25\,\text{eV}$, the peak is shifted ~0.1 eV

$\xi = 0\,\text{eV}$

μ (eV)	N	Energy (eV)	n_d	P_{d^6}	P_{d^7}	P_{d^8}	P_{d^9}	Multiplicity
25	27	−147.8402	7.074	0.166	0.579	0.228	0.016	4
26	27	−155.0182	7.289	0.106	0.518	0.336	0.034	4
	28	−154.9914	7.417	0.079	0.461	0.411	0.045	1
		−154.9913	7.417	0.079	0.461	0.411	0.045	2
27	28	−162.5560	7.695	0.037	0.322	0.547	0.090	1
		−162.5559	7.694	0.037	0.322	0.547	0.090	2

$\xi = 0.079\,\text{eV}$

μ (eV)	N	Energy (eV)	n_d	P_{d^6}	P_{d^7}	P_{d^8}	P_{d^9}	Multiplicity
25	27	−147.8939	7.074	0.165	0.581	0.227	0.016	2
		−147.8855	7.074	0.164	0.582	0.227	0.016	2
26	27	−155.0725	7.289	0.105	0.520	0.335	0.034	2
		−155.0635	7.289	0.105	0.520	0.335	0.034	2
	28	−155.0759	7.432	0.077	0.453	0.420	0.046	1
		−155.0711	7.428	0.078	0.455	0.417	0.046	1
		−155.0710	7.428	0.078	0.455	0.417	0.046	1
27	28	−162.6486	7.697	0.037	0.320	0.549	0.090	1
		−162.6406	7.695	0.037	0.322	0.547	0.091	2

Table 3.14: The energies and non-negligible (≥ 0.01) probability weights of impurity occupation numbers for the lowest eigen-energies of every sector, for different chemical potentials, for SOC values of 0 eV (top) and 0.079 eV (bottom).

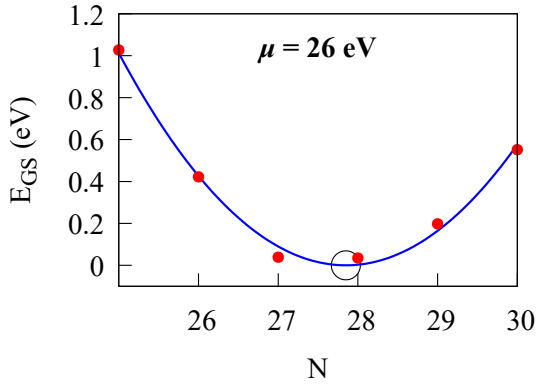

Figure 3.17: ground-state energy E_{GS} vs. number of electrons N for $\mu = 26\,\text{eV}$ and $\xi = 0.079\,\text{eV}$. The energy minimum is indicated with a black circle.

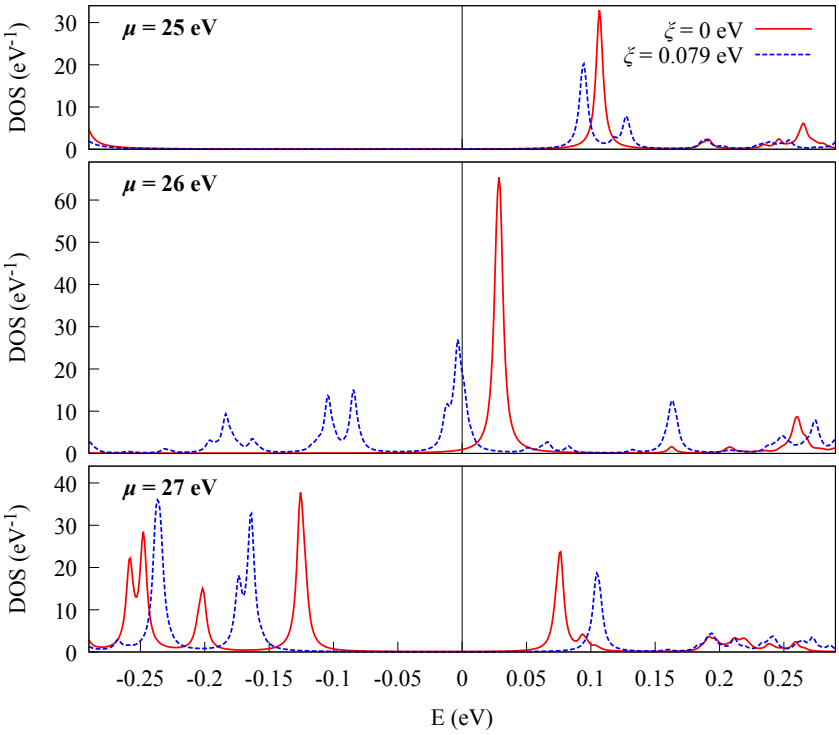

Figure 3.18: Total density of states for μ values of 26 eV, 27 eV and 28 eV, with SOC of 0.079 eV.

above the Fermi energy, which matches the observation that its occupation is $N = 27$ with zero charge fluctuation. For $\mu = 27\,\text{eV}$, the $28 \rightarrow 27$ peak is shifted ~0.15 eV down, so the total occupation is $N = 28$. The peak 0.1 eV above the Fermi energy corresponds to the transition from $29 \rightarrow 28$ transition.

3.4.3 Magnetic anisotropy

The expectation values of spin, orbit and total moments for each of the lowest eigenstates of each model are shown in Tab. 3.15. Those observables illuminate the structure of the ground state quadruplet and triplet, and can be used to model them as the approximate eigenstates of the phenomenological Hamiltonian of magnetic anisotropy [68]:

$$\hat{H}_{\text{MA}} = D\hat{J}_z^2 + E\left(\hat{J}_x^2 - \hat{J}_y^2\right). \tag{3.19}$$

The amplitudes D and E set the strength of the uniaxial and transverse magnetic anisotropy respectively. Those values can be deduced from the energies in Tab. 3.15.

Fig. 3.19 shows the structures of the ground-state quadruplet of $N = 27$ and the ground-state triplet of $N = 28$, for $\xi = 0.079\,\text{eV}$. The quadruplet is an effective d^7 state with $J = \frac{3}{2}$ which is split into the doublets $\left|\pm\frac{1}{2}\right\rangle$ and $\left|\pm\frac{3}{2}\right\rangle$ by the uniaxial component of $\hat{H}_{\text{MA}}$. In general, the transverse component mixes the doublets and creates four distinct energy levels, but according to the quadruplet energies in Tab. 3.15 no in-plane anisotropy takes place. From the J_z observables

$\xi = 0\,\mathrm{eV}$

μ (eV)	N	Energy (eV)	S_z	L_z	J_z
25	27	−147.8402	0.4229	0.0029	0.4257
		−147.8402	−0.4229	−0.0028	−0.4257
		−147.8402	1.2686	0.0086	1.2771
		−147.8402	−1.2686	−0.0086	−1.2771
26	27	−155.0182	0.3915	0.0034	0.3949
		−155.0182	−0.3915	−0.0034	−0.3949
		−155.0182	1.1745	0.0101	1.1846
		−155.0182	−1.1745	−0.0101	−1.1846
	28	−154.9914	0.0000	0.0000	0.0001
		−154.9913	0.2769	−0.0016	0.2754
		−154.9913	−0.2769	0.0016	−0.2752
27	28	−162.5560	0.0001	0.0000	0.0001
		−162.5559	0.3775	−0.0026	0.3749
		−162.5559	−0.3775	0.0026	−0.3749

$\xi = 0.079\,\mathrm{eV}$

μ (eV)	N	Energy (eV)	S_z	L_z	J_z
25	27	−147.8939	0.3661	0.2193	0.5855
		−147.8939	−0.3661	−0.2193	−0.5855
		−147.8855	1.0825	0.6408	1.7233
		−147.8855	−1.0825	−0.6408	−1.7233
26	27	−155.0725	0.3415	0.2242	0.5657
		−155.0725	−0.3415	−0.2242	−0.5657
		−155.0635	1.0078	0.6453	1.6531
		−155.0635	−1.0078	−0.6453	−1.6531
	28	−155.0759	0.0000	0.0000	0.0000
		−155.0711	0.0012	0.0000	0.0016
		−155.0710	−0.0012	0.0000	−0.0016
27	28	−162.6486	0.0000	0.0000	0.0000
		−162.6406	0.0018	0.0000	0.0022
		−162.6406	−0.0018	0.0000	−0.0022

Table 3.15: The energies and spin values for the ground states for various values of μ, for zero SOC values of 0 eV (top) and 0.079 eV (bottom).

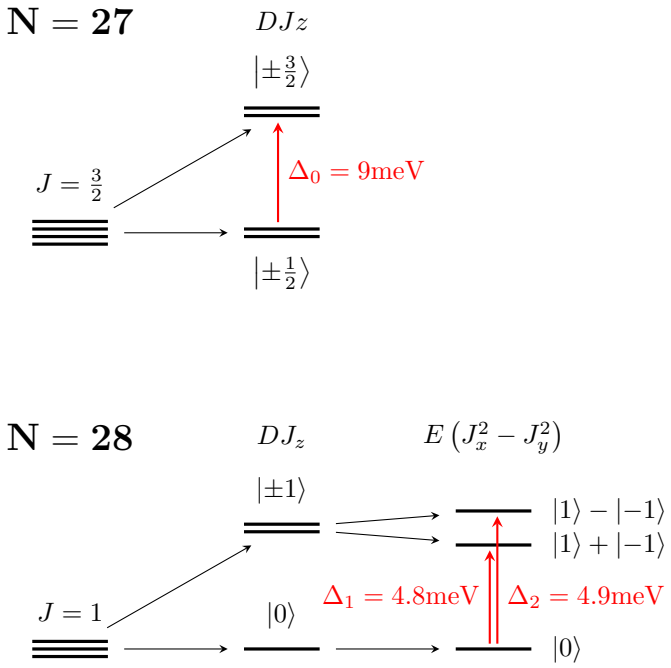

Figure 3.19: Splitting of the effective spin $J = \frac{3}{2}$ quadruplet by the magnetic anisotropy in *Eq.* (3.19). The spin excitation Δ_0 from $\left|m = \pm\frac{1}{2}\right\rangle$ to $\left|m = \pm\frac{3}{2}\right\rangle$ gives rise to an inelastic step in the differential conductance.

we can see that the $\left|\pm\frac{1}{2}\right\rangle$ doublet has a lower energy, hence $D > 0$. The projections of $D\hat{J}_z^2$ on the $\left|\pm\frac{1}{2}\right\rangle$ and $\left|\pm\frac{3}{2}\right\rangle$ doublets are $\frac{1}{4}D$ and $\frac{9}{4}D$ respectively, which means that the uniaxial component induces an energy gap of $\Delta_0 = D$. From the quadruplet energies we get $D = 9\,\text{meV}$.

The triplet is an effective d^8 state with $J = 1$. The uniaxial component splits the triplet into a singlet $|0\rangle$ and a doublet $|\pm1\rangle$ with a gap of D, and the transverse component splits the doublet into the two linear combinations $\frac{1}{\sqrt{2}}\left(\left|\frac{1}{2}\right\rangle \pm \left|-\frac{1}{2}\right\rangle\right)$ with an energy gap of $2E$ between them. The doublet energies are thus expected to be at gaps of $\Delta_{1,2} = D \pm E$ from the singlet. Using the triplet energies in Tab. 3.15 we find that, $\Delta_1 = 4.8\,\text{meV}$ and $\Delta_2 = 4.9\,\text{meV}$, thus $D = 4.85\,\text{meV}$ and $E = 0.05\,\text{meV}$.

3.4.4 Differential conductance

The results of STS measurements of Co@Cu_2N/Cu (001) can be seen in Ref. [69, 70]. The plot of differential conductance against the bias voltage is symmetrical, with a peak at zero bias and a single step at ~5 meV in each direction of the bias.

In theoretical models of magnetic anisotropy, the differential conductance plot is expected to have a step corresponding to every excitation energy [71, 72]. Whenever the bias grows larger than an the excitation energy, this excitation becomes energetically possible. The steps seen in the experimental results [69, 70] correspond to the lowest excitation, or multiple overlapping excitations.

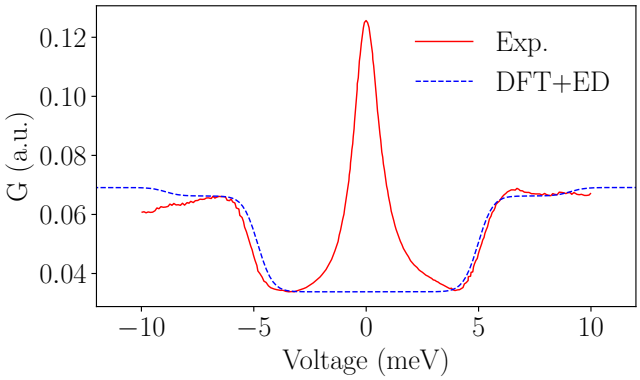

Figure 3.20: Calculated inelastic contribution to the differential conductance at the ground state for $\mu = 26\,\text{eV}$, plotted against the STS spectrum for $T = 2.5\,\text{K}$ from Ref. [70], using arbitrary units. The spectrum was normalized to fit the experimental result.

The expression for the inelastic part of the finite-temperature tunneling spectrum through a magnetic anisotropy is [71]

$$I(V) = \sum_{N\alpha\alpha'} p_{N\alpha} \left|\langle N\alpha| \hat{H}_{\text{MA}} |N\alpha'\rangle\right|^2 \sum_{\zeta=\pm1} \frac{eV - \zeta\left(E_{N\alpha} - E_{N\alpha'}\right)}{1 - e^{-\zeta\beta(eV - \zeta(E_{N\alpha} - E_{N\alpha'}))}}. \tag{3.20}$$

$\zeta = \pm 1$ is used to symmetrize the function around $eV = 0$.

The state occupations $p_{27,\alpha}$ and $p_{28,\alpha}$ are taken to be equal to the relative weights of the respective sectors in the ground state mixture, namely 0.15 and 0.85 respectively. The matrix element $\langle N\alpha| \hat{H}_{\text{MA}} |N\alpha'\rangle$ defines the transitions that are possible according to conservation laws, thereby prohibiting transitions between sectors. At low temperatures ($\beta \gg 1$), the double derivative of the function consists of peaks at every energy equal to a gap $E_{N\alpha} - E_{N'\alpha'}$, and the lower the temperature, the narrower the peak. This gives the differential conductance a characteristic stepwise structure. The derivative of differential conductance corresponding to our system should describe the three aforementioned transitions:

$$\begin{aligned}\frac{\mathrm{d}^2 I}{\mathrm{d}\left(eV\right)^2} &\approx \sum_{N\alpha\alpha'} \sum_{\zeta=\pm1} p_{N\alpha} \left|\langle N\alpha| \hat{H}_{\text{MA}} |N\alpha'\rangle\right|^2 \delta\left(eV - \zeta\left(E_{N\alpha} - E_{N\alpha'}\right)\right) \\ &\sim \sum_{\zeta=\pm1} 0.15\left(\delta\left(eV - \zeta\Delta_0\right)\right) + 0.85\left(\delta\left(eV - \zeta\Delta_1\right) + \delta\left(eV - \zeta\Delta_2\right)\right).\end{aligned} \tag{3.21}$$

The inelastic contribution to the differential conductance $\mathrm{G} = \frac{\mathrm{d}I}{\mathrm{d}(eV)}$ was calculated for $T = 2.5\text{K}$ ($\beta = 4640\,\text{eV}^{-1}$) by numerically calculating Eq. (3.20) and differentiating it. It is shown in Fig. 3.20, plotted against the experimental spectrum from Ref. [70] with the same temperature. It has a main inelastic step at ~5 meV and a secondary step at ~9 meV. This plot can be compared to the experimental differential conductance, measured by STM [69, 70]. In the experimental data, only the main step is present.

3.4.5 Strong magnetic field

The DFT+ED method will be used to study the system's behavior under a strong external magnetic field. The XMCD experiments we compare our calculations to

B (meV)	μ (eV)	n_d	S_z	L_z	T_z	R_{LS}
0.01	26	7.397	0.0000	0.0000	0.0000	—
0.6	26	7.396	0.0425	0.0314	−0.0015	0.422
20	26.15	7.407	0.7882	0.7048	−0.0182	0.487
Exp. [73]	—	—	—	0.91±0.23	—	0.62±0.1

Table 3.16: Occupation n_d, spin S_z, orbital L_z, dipole moment T_z, and orbit-dipole ratio $R_{LS} = L_z/(2S_z + 7T_z)$ for the impurity per external magnetic field B and chemical potential μ.

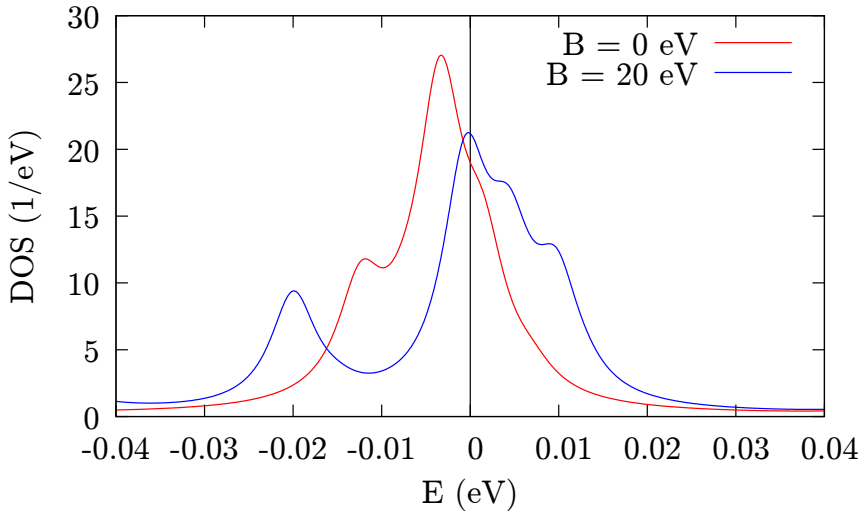

Figure 3.21: Spectral DOS for systems with external magnetic fields of $B = 10\,\mathrm{T}$ and $B = 300\,\mathrm{T}$.

were performed in an external magnetic field of 5 T, at a temperature of 8 K. A system was set up with $\mu = 26\,\mathrm{eV}$ and a magnetic field of $B = 0.6$ meV (~10 T) parallel to the z-axis. The resulting solution, seen in Tab. 3.16, is nearly paramagnetic with very small spin and orbital moments, mainly due to the spin-flip terms included in the full Coulomb interaction matrix [74]. In order to get a magnetic solution, we increased the field strength to $B = 20\,\mathrm{meV}$ (~300 T). The impurity occupation for the new system is $n_d = 7.29$. In order to bring the impurity occupation n_d to the same value of 7.4 as for $B = 0.6\,\mathrm{meV}$, we changed the chemical potential to 26.15 eV. The resulting spin, orbital magnetic moments are $M_S = \mu_B \cdot 2S_z = 1.58\mu_B$ and $M_L = \mu_B L_z = 0.7\mu_B$, and the orbit-dipole ratio $R_{LS} = \frac{L_z}{2S_z+7T_z}$ are in reasonable agreement with the XMCD experimental data [73].

The spectral density of the magnetic system ($B = 20$ meV) is compared to the paramagnetic system ($B = 0\,\mathrm{meV}$) in Fig. 3.21. The near-Fermi level peak for $B = 0\,\mathrm{meV}$ is split into two peaks by the $B = 20\,\mathrm{meV}$ field, in agreement with STM spectra [70].

Chapter summary

Three systems with cobalt atoms as impurities were studied using the DFT+ED method — $CoCu_{15}$, Co@Cu (001) and Co@Cu_2N/Cu (001). For each material, the DOS generated by DFT was used to construct a discrete AIM with four bath sites per impurity orbital. The chemical potential μ was used as a parameter, whose value was adjusted according to the observed occupation of the impurity's valence shell. Each system was measured with spin-orbit coupling and without it, in order to assess its effect on the qualitative shape of the ground state and first excitations.

For $CoCu_{15}$, the observed impurity occupation and impurity spin for three values of μ were found to be in good agreement with the DFT+QMC measurements in Ref. [57]. A resonance peak was achieved with a singlet ground state, which we interpret as Kondo resonance.

For Co@Cu (001), a resonance peak was found between the sectors $|\Omega_{26,0}\rangle$ and $|\Omega_{27,0}\rangle$. When calculated without SOC, the ground state is a mixture between degenerate triplet and a degenerate doublet. The application of SOC caused the triplet to split, forming a ground-state singlet. This indicates that a Kondo effect depends on the presence of SOC. The system was modeled as an STS system with Abrikosov-Suhl-Kondo resonance, and its Green's function was used to construct a Fano line shape that was used compared to an experimentally observed zero-bias anomaly.

For Co@Cu_2N, a Kondo peak was found between the $J = \frac{3}{2}$-like d^7 state and the $J = 1$-like d^8 state. The ground state and lowest excitations were modeled using a phenomenological Hamiltonian of magnetic anisotropy, and the energy gaps were used to construct a differential conductance curve that was found to be reasonably close to STS measurements. Finally, the system was run with a considerably higher magnetic field, and the resulting magnetic moments and DOS were found to show large orbital contributions to the magnetic moment of the cobalt adatom that were not accounted for in the $S = \frac{3}{2}$ models [70, 69].

Possible future extensions of the work in this chapter include the use of more than 4 excitations in the truncated Fock basis, direct comparison between DFT+ED and DFT+U, and the conduction of comparison with DFT+QMC on materials other than $CoCu_{15}$.

Chapter 4

Magnetic anisotropy of alloys

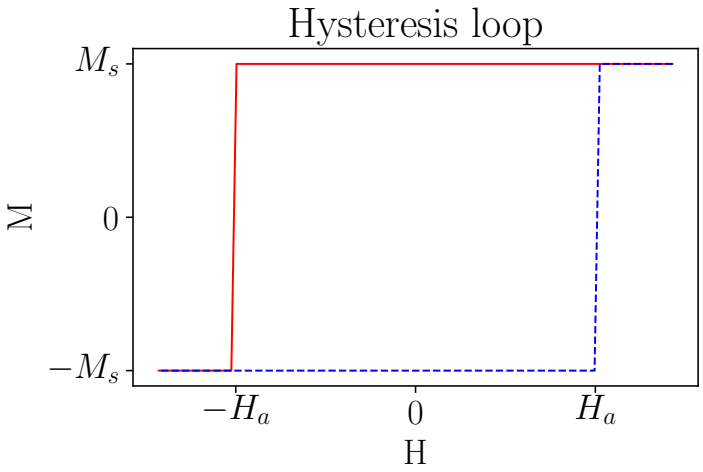

Figure 4.1: The magnetization as a function of external magnetic field in a hysteresis loop according to the Stoner-Wohlfarth model, for a uniaxial magnetic anisotropy parallel to the external field. In this case, $M_r = M_s$. The red line depicts the magnetization for a monotonic reduction of the external field from H_a to $-H_a$, and the blue line shows the opposite process.

In this chapter, we use various DFT schemes to investigate the magnetic anisotropy of hexagonal alloys of Fe_2Hf and $Fe_7Hf_3Sb_2$. The investigation was done as part of an effort to find good permanent magnets among alloys that are free of rare earth elements [75].

A permanent magnet is a material that, once magnetized, is capable of sustaining its own magnetic field even when the external magnetic field is removed. This property manifests as a hysteresis loop. When the external magnetic field varies from a high value (higher than the saturation value) in one direction to a high value in the opposite direction and back, the magnetization as a function of the field follows different (but symmetrical) paths in each direction. The magnetic saturation M_s is the magnetization to which the material asymptotically approaches in the limit of high external field. The anisotropy field H_a is the smallest magnetic field needed to completely reverse the magnetization. The

coercivity H_c and saturation remanence M_r are the absolute values of the loop's intersection of the $M = 0$ and $H = 0$ axes respectively.

Hysteresis is caused by magnetic anisotropy — dependence of the magnetic field's energy on its direction, due to the material's crystal structure. Hysteresis is particularly strong in materials with uniaxial magnetic anisotropy, i.e. materials that have only one easy axis (direction in which the anisotropy energy is at minimum [76]). In such a material, flipping the direction of magnetization necessarily requires applying a magnetic field strong enough to overcome the material's hard axis, which is perpendicular to the easy axis. The parameter that characterizes this energy is the magneto-crystalline anisotropy energy (MAE), the energy difference between the easy and hard axis.

Fig. 4.1 depicts the hysteresis loop of a system with a uniaxial magnetic anisotropy parallel to the external field, modeled by the Stoner-Wohlfarth model [77]. In this case, remanence is perfect, so that $M_r = M_s$, and the coercivity is at its upper value, so that $H_c = H_a$.

A good permanent magnet needs a high saturation moment in order to sustain strong magnetization, a Curie temperature (the temperature below which ferromagnetism occurs) significantly higher than room temperature, and a coercivity of at least $\mu_0 H_c = 1.5\,\mathrm{T}$, which is achieved when the MAE density is about 4 $\mathrm{MJ/m^3}$ [78]. Another important parameter is the maximum energy product $(BH)_{\max} = \frac{1}{4}\mu_0 M_s^2$, which is proportional to the magnet's energy density [77]. The larger the maximum energy product, the smaller the volume of the magnet necessary for its application. Finally, in order to resist self-demagnetization, the material's hardness parameter $k \equiv \sqrt{\frac{K_1}{\mu_0 M_s^2}}$ should be higher than 1 [77].

For example, the neodymium-based alloy $Nd_2Fe_{14}B$, a widely used rare-earth permanent magnet, has a Curie temperature of 588 K, a saturation moment of 1.28 MA/m, and a uniaxial MAE of 4.9 $\mathrm{MJ/m^3}$ with a tetragonal easy c-axis [79].

An additional condition for the practical viability of a material is its thermodynamic stability relatively to its constituent elements. The stability is evaluated using the enthalpy of formation — the energy required to assemble the crystal from its constituent elements.

In the first part, the investigated materials are the hexagonal alloy Fe_2Hf and a version of it with iron atoms substituted by antimony. Using a FLAPW basis with PAW potentials and LSDA, the MAE and magnetic moments of Fe_2Hf with and without antimony substitutions are calculated, and are compared to experimental values. The rest of the magnetic parameters are derived by modeling it as a uniaxial magnet, and are compared to criteria appearing in literature.

In the second part, the alloys UFe_{12} and $UFe_{10}Si_2$ are studied using two parallel approaches to LSDA+U — the orbital polarization correction method and the Hubbard-I approximation. The two methods are used to examine the itinerant and localized features of interactions between incomplete $5f$-shells. The magnetic moments of individual atoms, as well as the spectra of f-shell and other states were calculated by both of the approaches.

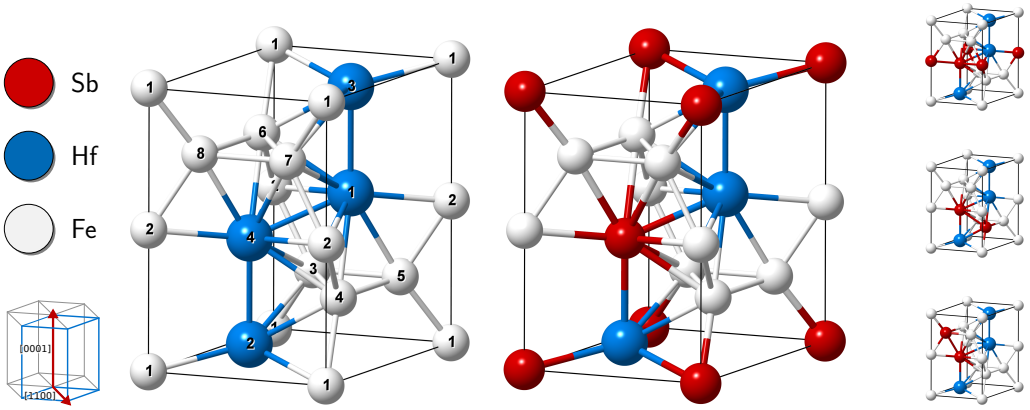

Figure 4.2: Left: crystal structure for a pristine Fe_2Hf with site indices for iron and hafnium. Center: crystal structure of the Fe58-Hf25-Sb17 configuration with the lowest total energy ([Fe (1) − Hf (4)]). Right: crystal structures of the configurations corresponding to the remaining symmetry groups of Fe58-Hf25-Sb17 (top to bottom: [Fe (2) − Hf (4)], [Fe (4) − Hf (4)], [Fe (8) − Hf (4)]).

4.1 Hexagonal Fe-Hf-Sb

4.1.1 Material

The Fe_2Hf crystal is in a hexagonal Laves phase with Strukturbericht designation C14 (space group $P6_3/mmc$) [80]. It is depicted in Fig. 4.2 (left). It has three special Wyckoff positions — (2a) and (6h) are occupied by iron atoms, and (4f) is occupied by hafnium atoms. The unit cell is a 60° angle rhombic prism with the lattice constants $a = 4.968$Å and $c = 8.098$Å, the length of the base's side and height of the unit cell respectively [81]. The volume of the unit cell is thus $173.1\,\text{Å}^3$ (it will be denoted as formula unit, or f.u.). The relative coordinates, Wyckoff positions and elements of each site are shown in the three leftmost columns of Tab. 4.1. The space group has two free parameters with experimentally determined values, $x = 0.17$ for (6h) and $z = 0.56$ for (4f) [82, 83].

Hafnium is a refractory metal (RM) in the wider definition [84]. Fe_2Hf has been explored as an example of a Fe-RM system that could exhibit high MAE, due to the difference in ionic radius between iron and hafnium which causes a difference in the spin-orbit coupling of the unfilled d-shells [85, 76]. Nevertheless, it is not considered as a viable candidate for a magnetically hard material, because it has been experimentally shown that the stochiometric C14 phase (where the iron-to-hafnium atom number ratio is exactly 2) is less stable at room temperature than the C15 phase, which has low MAE [85].

One of the proposed approaches to modify Fe_2Hf into a stable material is to mix it with antimony. In a study by Goll *et al.* [76], an alloy Fe60.0-Hf26.5-Sb13.5 was synthesized, in an off-stochiometric phase of the form $(Fe, Sb)_{2+x}\,Hf_{1-x}$. It had undergone scanning tunneling microscopy and energy dispersive X-ray analysis. It was found to have a saturation polarization of $M_s \sim 1\,\text{T}$, an anisotropy constant of $K_1 \sim 1.5\,\text{MJ/m}^{-3}$ and a Curie temperature of $T_c \sim 470\,\text{K}$, fulfilling the standards mentioned in this chapter's introduction.

For computational efficiency reasons, the alloy Fe60.0-Hf26.5-Sb13.5 alloy is approximated here in a single unit cell, where a single iron site and a single

Wyckoff positions	Internal position	Fe_2Hf Element	Fe_2Hf Magnetic moments (μ_B)	Fe58-Hf25-Sb17 Element	Fe58-Hf25-Sb17 Magnetic moments (μ_B)
(2a)	$(0, 0, 0)$	Fe (1)	1.71	Sb	–0.03
	$(0, 0, 1/2)$	Fe (2)	1.71	Fe	2.00
(6h)	$(x, 2x, 1/4)$	Fe (3)	1.74	Fe	1.64
	$(-2x, -x, 1/4)$	Fe (4)	1.74	Fe	1.64
	$(x, -x, 1/4)$	Fe (5)	1.74	Fe	1.64
	$(2x, x, -1/4)$	Fe (6)	1.74	Fe	1.55
	$(-x, -2x, -1/4)$	Fe (7)	1.74	Fe	1.55
	$(-x, x, -1/4)$	Fe (8)	1.74	Fe	1.55
(4f)	$(1/3, 2/3, z)$	Hf (1)	–0.35	Hf	–0.28
	$(2/3, 1/3, z - 1/2)$	Hf (2)	–0.35	Hf	–0.30
	$(1/3, 2/3, 1/2 - z)$	Hf (3)	–0.35	Hf	–0.27
	$(2/3, 1/3, -z)$	Hf (4)	–0.35	Sb	0.01
	Total		13.48		10.48

Table 4.1: Calculated magnetic moments inside the MT-spheres of each atom in the unit cell. The coordinates are relative to the dimensions of the unit cell. The parameters' values are $x = 0.17$ and $z = 0.56$. Negative coordinates can be converted to positive by adding 1 to them.

hafnium site are occupied by antimony atoms. This makes the alloy to be effectively Fe58-Hf25-Sb17 (the ratios are given as approximate parts of 100). The unit cell has 32 possible configurations. Due to the crystal's symmetry, those configurations can be categorized into 4 groups, so that the configurations in each group are physically equivalent. A representative configuration from each group is shown in Fig. 4.2 (center and right).

4.1.2 Results

The system's electronic structure was calculated using the PAW method (as described in Sec. 1.6.3), implemented using VASP, without SOC. The total energy of each of the 32 configurations of Fe58-Hf25-Sb17 was calculated. As was expected, the configurations in each group all have the same energy. The energies per f.u. (formula unit) of each group relative to the lowest are shown in Tab. 4.2. The configurations are denoted in terms of the Fe_2Hf atoms that the antimony atoms replace; for example, $[\mathrm{Fe}\,(1) - \mathrm{Hf}\,(1)]$ corresponds to the crystal where $\mathrm{Fe}\,(1)$ and $\mathrm{Hf}\,(1)$ are replaced by antimony. The groups were numbered from the lowest-energy one to the highest. In Fig. 4.2, a configuration of the lowest energy ($[\mathrm{Fe}\,(1) - \mathrm{Hf}\,(4)]$) is shown in the center, and representative of the three others (top to bottom: $[\mathrm{Fe}\,(2) - \mathrm{Hf}\,(4)]$, $[\mathrm{Fe}\,(4) - \mathrm{Hf}\,(4)]$, $[\mathrm{Fe}\,(8) - \mathrm{Hf}\,(4)]$) are shown to the right. As can be seen, Fe58-Hf25-Sb17 has the lowest total energy when the antimony dopants are as far from each other as possible. For this reason, Fe58-Hf25-Sb17 is represented in the rest of the chapter by the configuration $[\mathrm{Fe}\,(1) - \mathrm{Hf}\,(4)]$.

Group	Sb substitution sites	ΔE (eV/f.u.)
1	[Fe (1) − Hf (1)] [Fe (2) − Hf (2)] [Fe (2) − Hf (3)] [Fe (1) − Hf (4)]	0
2	[Fe (3) − Hf (1)] [Fe (4) − Hf (1)] [Fe (5) − Hf (1)] [Fe (6) − Hf (2)] [Fe (7) − Hf (2)] [Fe (8) − Hf (2)] [Fe (3) − Hf (3)] [Fe (4) − Hf (3)] [Fe (5) − Hf (3)] [Fe (6) − Hf (4)] [Fe (7) − Hf (4)] [Fe (8) − Hf (4)]	0.137
3	[Fe (6) − Hf (1)] [Fe (7) − Hf (1)] [Fe (8) − Hf (1)] [Fe (3) − Hf (2)] [Fe (4) − Hf (2)] [Fe (5) − Hf (2)] [Fe (6) − Hf (3)] [Fe (7) − Hf (3)] [Fe (8) − Hf (3)] [Fe (3) − Hf (4)] [Fe (4) − Hf (4)] [Fe (5) − Hf (4)]	0.215
4	[Fe (2) − Hf (1)] [Fe (1) − Hf (2)] [Fe (1) − Hf (3)] [Fe (2) − Hf (4)]	0.258

Table 4.2: The 32 possible configurations of the $Fe_7Hf_3Sb_2$ unit cell, grouped according to shared symmetry, and their energy relative to the lowest configuration.

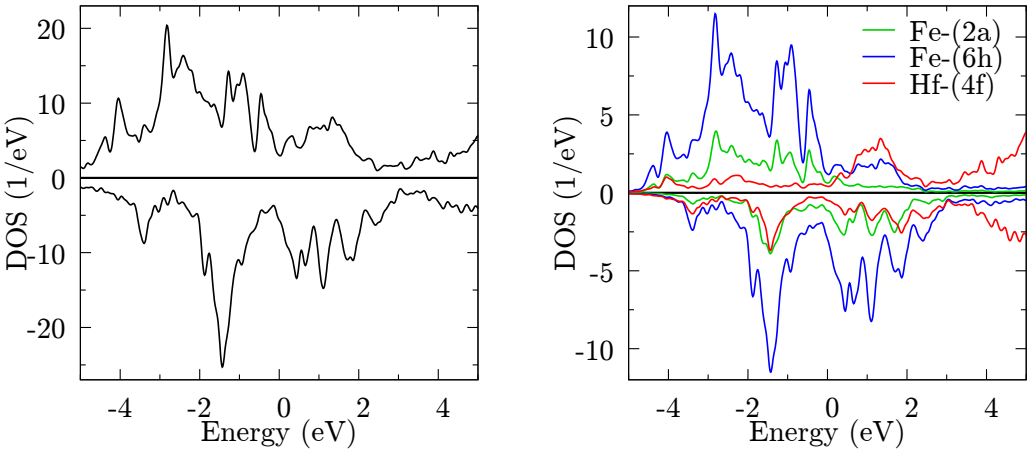

Figure 4.3: Spin-projected DOS of the 3*d*-states of iron and 5*d*-states hafnium in Fe_2Hf, with $E_F = 0$. Left: Total DOS. Right: DOS summed over each atom species and Wyckoff position. The up and down spins are shown on the top and bottom part of each plot respectively.

The magnetic moments for each atom in the unit cell were calculated in the muffin-tin volume of each atom, and are shown in Tab. 4.1. For Fe_2Hf, all atoms of the same Wyckoff positions have the same moments, with hafnium and iron being anti-aligned. The antimony dopants in Fe58-Hf25-Sb17 have almost no magnetic moment. Their presence raises slightly the moment of Fe-(2a), reduces slightly the moments of hafnium and Fe-(6h), and reduces the total magnetic moment by $3\mu_B$.

Fig. 4.3 shows the density of states for Fe_2Hf, projected on the valence shells of iron and hafnium. It can be seen that for the iron atoms (in both (2a) and (6h) Wyckoff positions), the spin-down states are shifted upwards compared to the spin-up states, whereas for the hafnium atoms the splitting is in the opposite direction. This matches the measured anti-alignment of iron and hafnium's magnetic moments.

4.1.3 Magnetic parameters

The phenomenological model of MAE in uniaxial crystals up to the first approximation is

$$E_{\mathrm{MA}} = K_1 \sin^2 \theta, \tag{4.1}$$

with K_1 as the magneto-crystalline anisotropy constant and θ as the angle between the magnetization and the easy axis [0001] [77]. The magnetic anisotropy energy of the system was evaluated by calculating the total energy for two orientations of the magnetization — the easy axis [0001] and the in-plane direction [1100] — and subtracting the two:

$$E_{\mathrm{MA}} = E\,[1100] - E\,[0001] \tag{4.2}$$

The energies were calculated using relativistic FLAPW [86] using LSDA with SOC. The discrete Brillouin zone incorporated about 3200 k-points for Fe_2Hf

Composition	$M_{\text{sat}}\left(\frac{\mu_B}{\text{f.u.}}\right)$	$E_{\text{MA}}\left(\frac{\text{meV}}{\text{f.u.}}\right)$	Volume $\left(\text{Å}^3\right)$	$\frac{c}{a}$
Unrelaxed Fe_2Hf	13.48	-0.57	173	1.63
Unrelaxed Fe58-Hf25-Sb17	10.48	0.88	173	1.63
Relaxed Fe58-Hf25-Sb17	10.93	1.37	179	1.64
Exp. Fe60-Hf26.5-Sb13.5 [76]	$10.87 - 15.53$	$1.57 - 1.69$	180	1.627

Table 4.3: The saturation magnetization M_s, MAE E_{MA}, unit cell volume and lattice constant ratio for each of the calculated substances and the experimental results.

and 5400 points for Fe58-Hf25-Sb17, with Gaussian smearing (see Eq. (1.42)) of $\sigma = 1\,\text{mRy}$.

The doping of Fe_2Hf by antimony is expected to affect the atomic coordinates and the unit cell's volume and shape. For this reason, Fe58-Hf25-Sb17 underwent relaxation of the atomic coordinates, the unit cell's volume and the c/a ratio before calculating its electronic structure. The relaxation was performed in VASP using the quasi-Newtonian RMM-DIIS method [87] with a residual force threshold of $0.1\,\text{meV/Å}$. For comparison, the system was also run without relaxation.

The results are given in Tab. 4.3, and are compared to the experimental results from Ref. [76] for Fe60-Hf26.5-Sb13.5. Fe_2Hf has a negative MAE, which indicates preference to the in-plane direction, whereas Fe58-Hf25-Sb17 has positive MAE, which indicates uniaxial magnetic anisotropy as desired. The relaxation of the Fe58-Hf25-Sb17 system significantly changes the measured MAE, bringing it closer to the experimental values.

The saturation magnetization of each system is the total magnetic moment per unit volume ($M_s = m_{\text{tot}}/\text{f.u.}$). The saturation magnetization is only slightly increased by the relaxation, and is on the low end of the experimental measurements. The saturation magnetization's relatively low value may be the caused by our model having a larger concentration of antimony than the experiment, since antimony has been shown to reduce its value. The relaxation caused the unit cell's volume to increase, which is consistent with the increase in saturation magnetization.

The anisotropy field in a uniaxial crystal is [77]

$$\mu_0 H_a = \frac{2K_1}{M_s} = 4.5\,\text{T}. \tag{4.3}$$

The other magnetic parameters mentioned in this chapter's introduction have been calculated and are shown in Tab. 4.8, alongside the recommended magnetic parameters from literature. Though the material has relatively low MAE density, magnetic saturation and maximum energy product, it has a high anisotropy field and hardness parameter.

4.1.4 Stability

In order to evaluate the thermodynamic stability of Fe58-Hf25-Sb17, we need to calculate its enthalpy of formation — the difference between the total energy of the crystal and the total energy of its constituent elements. A negative enthalpy

	Relaxed Fe58-Hf25-Sb17	Requirements
K_1 $\left(\frac{\mathrm{MJ}}{\mathrm{m}^3}\right)$	1.27	4 [78]
$\mu_0 M_s$(T)	0.71	1.25 [88]
$\mu_0 H_a$ (T)	4.51	3.75 [88]
$(BH)_{\max}$ $\left(\frac{\mathrm{KJ}}{\mathrm{m}^3}\right)$	99.6	460 [89]
k	1.79	1 [77]

Table 4.4: Magneto-crystalline anisotropy constant K_1, magnetic saturation moment M_s, anisotropy field H_a, maximum energy product $(BH)_{\max}$ and hardness parameter k of the relaxed Fe58-Hf25-Sb17 model, compared to requirements from literature.

indicates a stable material, since it is energetically favorable when created by annealing. The expression for the enthalpy is [90]

$$\Delta H = E - \sum_i x_i \mu_i, \tag{4.4}$$

where E is the total energy of the supercell, x_i is the number of atoms of element i in the supercell and μ_i is its chemical potential of element i. By convention, the chemical potentials are calculated from the unit cell total energy of each element's crystalline form, which is found by DFT. The enthalpies of the systems are

$$\Delta H_{\mathrm{Fe_2Hf}} = E_{\mathrm{Fe_2Hf}} - \frac{8}{2} E_{\mathrm{Fe}} - \frac{4}{2} E_{\mathrm{Hf}} \tag{4.5}$$

and

$$\Delta H_{\text{Fe58-Hf25-Sb17}} = E_{\text{Fe58-Hf25-Sb17}} - \frac{7}{2} E_{\mathrm{Fe}} - \frac{3}{2} E_{\mathrm{Hf}} - \frac{2}{6} E_{\mathrm{Sb}}. \tag{4.6}$$

The enthalpy of Fe_2Hf was found to be $-1.165\,\mathrm{eV/f.u.}$, and the enthalpy of Fe58-Hf25-Sb17 was found to be $-0.724\,\mathrm{eV/f.u}$. The negative sign of the enthalpy indicates that the antimony-doped crystal is thermodynamically stable, albeit less so than Fe_2Hf.

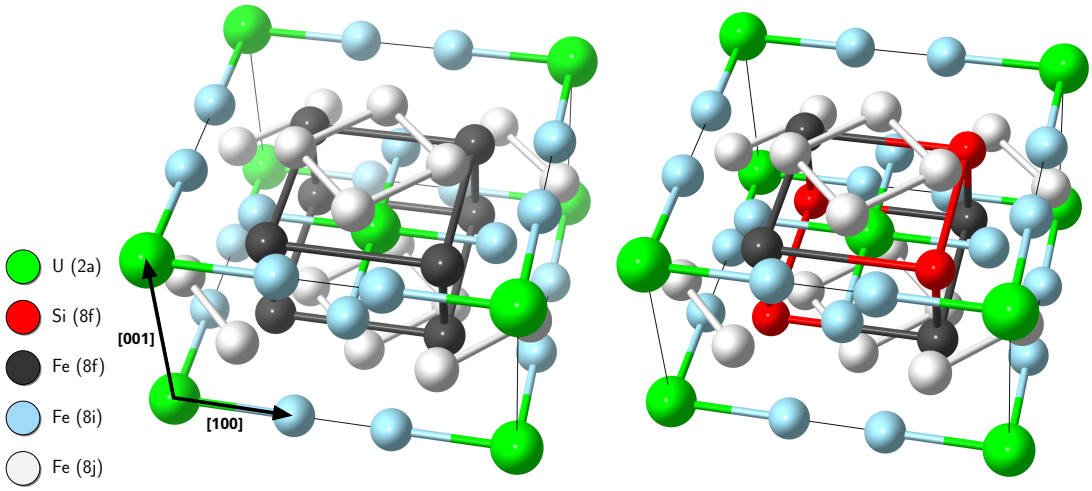

Figure 4.4: Left: Crystal structure of pristine UFe_{12}, consisting of two unit cells. Right: crystal structure of a configuration of $UFe_{10}Si_2$ with both silicon atoms in the unit cell replacing (8f) iron atoms.

Wyckoff positions	Internal position	Element
(2a)	$(0,0,0)$	U
(8f)	$\left(\pm\frac{1}{4},\pm\frac{1}{4},\pm\frac{1}{4}\right)$	Fe
(8i)	$(\pm x_3,0,0)$,$(0,\pm x_3,0)$	Fe
(8j)	$\left(\pm x_4,\frac{1}{2},0\right)$,$\left(\frac{1}{2},\pm x_4,0\right)$	Fe

Table 4.5: The Wyckoff positions and coordinates of the atoms in UFe_{12}. The values of the variables are $x_3 = 0.36$ and $x_4 = 0.28$.

4.2 Magnetic anisotropy of U-based ferromagnets

4.2.1 Crystal structure

UFe_{12} has a body-centered tetragonal structure with tetragonal symmetry. Its Strukturbericht designation is $D2_b$ (space group I4/mmm, no. 139), as depicted in Fig. 4.4 (left). The dimensions of the supercell, which includes two unit cells, are $a = 8.47\,\text{Å}$ (length and width) and $c = 4.72\,\text{Å}$ (height) [91]. This gives it a volume of $338.6\,\text{Å}^3$. The size of the unit cell is half of it, $169.3\,\text{Å}^3$.

The crystal consists of four distinct Wyckoff positions — (2a) is occupied by uranium, and (8f), (8i) and (8j) are occupied by iron. Their coordinates are shown in Tab. 4.5. The coordinates of each Wyckoff position are determined by the crystal structure up to two parameters, x_3 and x_4, which are unique for each material. The parameter values for UFe_{12} are $x_3 = 0.36$ and $x_4 = 0.28$ [91].

In UFe_{12}, uranium is a $5f$-shell actinide with the electronic configuration $[\text{Rn}]\,5f^3 6d^1 7s^2$. Its valence shells are $6d$ and $5f$, with 10 and 14 spin-orbitals respectively. Since the $5f$-shell is more local, it has a narrower bandwidth, and

thus a higher DOS around the Fermi energy, which makes it dominate the conductivity.

$UFe_{10}Si_2$ is the instance of the $UFe_{10-x}Si_x$ class of materials with the highest Curie temperature and molecular magnetic moment [92]. It has the same crystal structure as UFe_{12}, with silicon atoms randomly occupying the (8f) and (8j) Wyckoff positions [91, 93]. An ab-initio computation of a periodic system can't model a disordered system exactly, so our system will consist of a single unit cell with two iron sites replaced by silicon. In order to keep the system as symmetrical as possible, both silicon atoms will be placed in (8f) positions. The crystal structure used in this work is depicted in Fig. 4.4 (right). The dimentions of the $UFe_{10}Si_2$ supercell are $a = 8.37$ and $c = 4.721$, making a supercell volume of $330.7\,\text{Å}^3$ and a unit cell volume of $165.35\,\text{Å}^3$ [91, 92].

4.2.2 LSDA+U approaches

The system's electronic structure has been calculated using a FLAPW solver, using LSDA+U, as described in Sec. 1.3.2.

Two different approaches to LSDA+U were used — the orbital polarization correction (OPC) method, an itinerant model which assumes a low Coloumb interaction in the $5f$-shell, and the Hubbard-I approximation (HIA), a localized model which assumes a weak hybridization between the uranium impurity and the rest of the system. The two approaches are used because in systems of uranium impurities embedded in transition metals, the $5f$-shell states may exhibit either itinerant superconducting behavior or localized magnetic behavior, depending roughly on the shortest distance between impurities. According to the Hill plot for uranium compounds, the transition from itinerant to local behavior generally occurs for distances larger than 3.5 Å, through some crystals such as UBe_{13} and UPt_3 retain superconducting behavior for larger distances [94]. For UFe_{12}, the U-U distance is the supercell's height, 4.72 Å.

4.2.2.1 LSDA+U(OPC)

The LSDA+U(OPC) approach is described in Sec. 1.3.2.2. The interaction parameters used in our calculation are $U = 0.51$ eV and $J = 0.51$ eV, using Slater integrals reduced to 70% of the atomic Hartree-Fock values [95]. By choosing the Coulomb interaction U to be equal to the exchange interaction J, the model includes the anisotropic energy only.

The OPC term can be expressed as an eigenvalue shift term by replacing the orbital interaction term $-\frac{1}{2}\sum_{i\neq j}\hat{L}_i\hat{L}_j$, which applies to every couple of electrons i and j in the ground state, with the mean-field approximation $-\frac{1}{2}\sum_{i\neq j}\hat{L}_i^z\hat{L}_j^z$ [96]. The resulting one-electron eigenvalue shift is

$$E^{\text{OPC}} = -E^3 l m_l, \tag{4.7}$$

where E^3 is the third Racah parameter [97], $l = 3$ is the f-shell orbital momentum and m_l is the magnetic quantum number [96].

The non-spherical double-counting term consists of the contributions $\langle lm|\,\hat{Y}\,|lm'\rangle$, where $\hat{Y}$ are the spherically non-symmetric harmonics from the muffin-tin part of Eq. (1.52) [98].

Under the OPC scheme, the MAE is calculated in a similar manner to Tab. 4.3:

$$E_{\mathrm{MA}} = E\left[100\right] - E\left[001\right]. \tag{4.8}$$

$E\left[100\right]$ and $E\left[001\right]$ were calculated in the same discretized reciprocal space in every iteration of the DFT algorithm. The total energy convergence was found to be better than 0.1 meV.

4.2.2.2 LSDA+U(HIA)

The LSDA+U(HIA) method incorporates interaction into DFT+U via the exact diagonalization of an atomic Hamiltonian. Unlike the DFT+ED method used in the previous chapter, under LSDA+U(HIA) the diagonalization is a part of the DFT self-consistency loop, and is used to produce the occupation matrix $n_{\gamma\gamma'}$, which can then be plugged into the LSDA+U energy functional in Eq. (1.27). This method assumes the atomic limit, where there's a weak hybridization between the impurity's f-states and its other, more itinerant shells. Under this assumption, the system's f-states are described using the impurity part of Anderson impurity model [99]:

$$\hat{H}_{\mathrm{imp}} = H_0 + H_U, \tag{4.9}$$

where

$$H_0 = \sum_{\gamma} \epsilon_f f_{\gamma}^{\dagger} f_{\gamma} + \sum_{\gamma\gamma'} \left(\xi \mathbf{l}\cdot\mathbf{s} + \Delta_{\gamma\gamma'}^{\mathrm{CF}} + \frac{\Delta^{\mathrm{ex}}}{2}\hat{\sigma}_z \right) f_{\gamma}^{\dagger} f_{\gamma'} \tag{4.10}$$

and

$$H_U = \frac{1}{2} \sum_{m_1 m_2 m_3 m_4 \sigma\sigma'} U_{m_1 m_2 m_3 m_4} f_{m_1\sigma}^{\dagger} f_{m_2\sigma'}^{\dagger} f_{m_3\sigma'} f_{m_4\sigma}. \tag{4.11}$$

The non-interacting term of H_0 includes, in addition to the spin-orbit coupling term $\xi\mathbf{l}\cdot\mathbf{s}$ and crystal field term Δ^{CF} used in previous chapters, the exchange field Δ^{ex}.

The local Hamiltonian $\hat{H}_{\mathrm{imp}}$ is diagonalized using the Lanczos method, and is used to construct the local Green's function of the decoupled system, with and without interaction respectively:

$$G_{\gamma\gamma'}^{\mathrm{imp}}\left(z\right) = \left\langle\gamma\right| \left(z - \hat{H}_{\mathrm{imp}}\right)^{-1} \left|\gamma'\right\rangle, \tag{4.12}$$

$$G_{\gamma\gamma'}^{0}\left(z\right) = \left\langle\gamma\right| \left(z - \hat{H}_{0}\right)^{-1} \left|\gamma'\right\rangle. \tag{4.13}$$

The self-energy $\hat{\Sigma}\left(z\right)$ is obtained from the Green's function via the Dyson equation:

$$\hat{\Sigma}\left(z\right) = \left[\hat{G}^{0}\left(z\right)\right]^{-1} - \left[\hat{G}^{\mathrm{imp}}\left(z\right)\right]^{-1} \tag{4.14}$$

The self-energy matrix represents the energy contribution of the interaction. It is incorporated into the DFT model by adding it to the Hamiltonian matrix in the expression of the Green's function DFT from Eq. (1.60):

$$G_{\gamma\gamma'}^{\mathrm{DFT}}(z) = \frac{1}{\Omega_{\mathrm{BZ}}} \int_{\mathrm{BZ}} \mathrm{d}\mathbf{k} \left\langle \gamma \right| \left(z + \mu - \hat{H}^{\mathrm{LSDA}}(\mathbf{k}) - \hat{\Sigma}(z) \right)^{-1} \left| \gamma' \right\rangle \tag{4.15}$$

The full Green's function is then used to derive the occupation matrix $n_{\gamma\gamma'}$ — the integral over the non-diagonal spectral density $-\mathrm{Im}G_{\gamma\gamma'}^{\mathrm{DFT}}(\epsilon)/\pi$ for the energies below the Fermi energy:

$$n_{\gamma\gamma'} = -\frac{1}{\pi} \mathrm{Im} \int_{-\infty}^{\epsilon_F} G_{\gamma\gamma'}^{\mathrm{DFT}}(\epsilon)\, d\epsilon. \tag{4.16}$$

The Coulomb repulsion was set to $U = 3$ eV, while for exchange interaction we used the same value as before, $J = 0.51$ eV.

MAE calculation with HIA is more difficult than with OPC, because the strong interaction raises each energy in the two terms of Eq. (4.8), and catastrophic cancellation[1] harms the precision of their difference. Using the previous method, an accuracy of 0.1 meV was not achieved. The MAE is thus calculated using a Hamiltonian term describing the crystal field energy of the uranium atom [89, 91]:

$$\hat{H}_{\mathrm{CF}} = \sum_{nm} A_n^m \left\langle r^n \right\rangle \Theta_n(J)\, \hat{O}_n^m \tag{4.17}$$

In this term, $\hat{O}_n^m$ are the Stevens operators [100], $\Theta_n(J)$ are the Stevens factors for a ground state multiplet J and $A_n^m \left\langle r^n \right\rangle$ are the crystal-field parameters for the $5f$-shell. With θ as the altitude angle of the quantization axis, the energy contribution of the CF term is [89]

$$E_{\mathrm{MA}}(\theta) = \frac{1}{4} \left\langle J, J_z(\theta) = -J \right| \hat{H}_{\mathrm{CF}} \left| J, J_z(\theta) = -J \right\rangle - \mathrm{const.} \tag{4.18}$$

The MAE contribution of a Uranium atom can be calculated as the difference $E_{\mathrm{MA}}\left(\frac{\pi}{2}\right) - E_{\mathrm{MA}}(0)$. In the first approximation, the MAE is equal to $K_1 \sin^2\theta$.

4.2.3 Results

The two LSDA+U approaches were used to calculate the spin, orbital and total magnetic moments parallel to the [001] crystal direction for each atom in each crystal. The calculated momenta are shown in Tab. 4.6, along with the sum of spin, orbital and total moments per unit cell. As can be seen, the moments of iron and silicon sites are almost identical between the methods, as uranium's interactions affect them very weakly. The orbital moments of uranium are much larger when calculated in HIA. The spin momenta of uranium and iron are anti-parallel to each other. This matches the known mechanism, where a transition impurity couples anti-ferromagnetically to a transition ferromagnetic host if the

[1] Loss of significant digits which occurs when two floating point numbers are substracted.

UFe_{12}

Element	HIA			OPC		
	m_S	m_L	m_{tot}	m_S	m_L	m_{tot}
U (2a)	-2.28	4.57	2.29	-1.98	2.30	0.32
Fe (8f)	1.68	0.06	1.74	1.69	0.05	1.74
Fe (8i)	2.42	0.10	2.52	2.40	0.10	2.50
Fe (8j)	2.05	0.09	2.14	2.00	0.09	2.09
Unit cell	21.94	5.61	27.55	21.97	3.25	25.21

$UFe_{10}Si_2$

Element	HIA			OPC		
	m_S	m_L	m_{tot}	m_S	m_L	m_{tot}
U (2a)	−2.28	4.70	2.42	−2.76	2.95	0.19
Si (8f)	−0.08	0.00	−0.08	−0.08	0.00	−0.08
Fe (8f)	1.69	0.07	1.76	1.72	0.08	1.80
Fe (8i)	2.29	0.11	2.40	2.30	0.11	2.41
Fe (8j)	1.91	0.11	2.02	1.93	0.11	2.04
Unit cell	17.25	5.73	21.92	16.98	3.95	20.93

Table 4.6: Spin m_S, orbital m_L and total m_{tot} magnetic moments (all in units of μ_B) alongside the [001] direction for individual atoms and the total unit cell, for UFe_{12} (top) and $UFe_{10}Si_2$ (bottom).

	U MAE (meV/f.u.)	Total MAE (meV/f.u.)
UFe_{12} (OPC)	—	-67.5
UFe_{12} (HIA)	8.92	11.12
$UFe_{10}Si_2$ (HIA)	2.56	3.99
$UFe_{10}Si_2$ (Exp.)	—	3.1

Table 4.7: MAE of the uranium atom and the total MAE, for UFe_{12} and $UFe_{10}Si_2$. Experimental data from Ref. [93] is provided for reference.

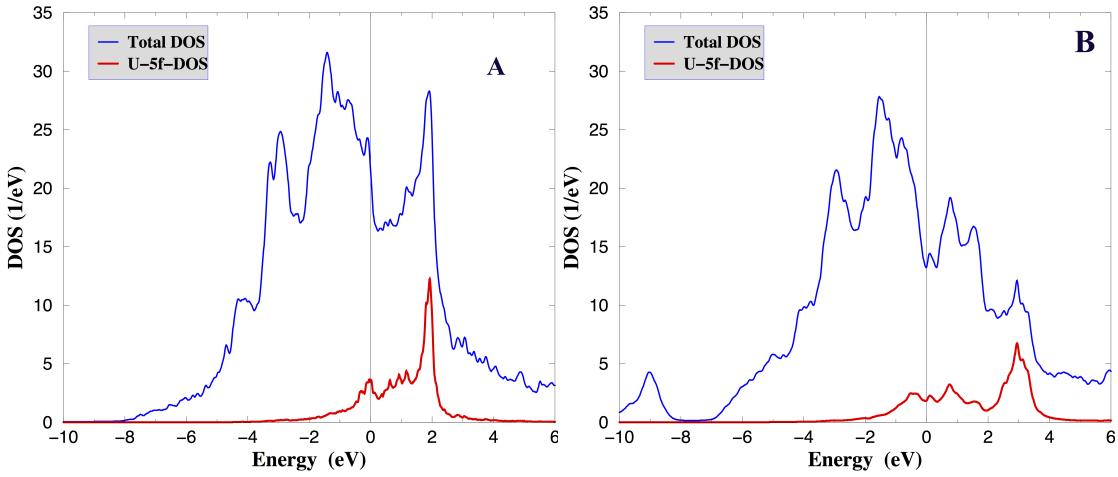

Figure 4.5: Total DOS and DOS projected on the U-5f states in the LSDA+U(OPC) approach, for UFe_{12} (A) and $UFe_{10}Si_2$ (B).

two elements are on the opposite sides of the transition series [101, 102]. Silicon atoms are almost non-magnetic.

The comparison of the two tables in Tab. 4.6 allows to examine the effect of substitution of Fe-(8f) atoms by silicon on the rest of the moments. The moments of uranium are very weakly affected, while the spin moments of Fe-(8i) and Fe-(8j) are reduced. The reduction is caused by silicon's valence shell having a smaller total spin than iron — with three electrons in a p-shell, it has a total spin of $S = \frac{3}{2}$, compared to iron's 6 electrons in a d-shell with a spin of $S = 2$. In total, where UFe_{12} has a total magnetic moment per unit cell of $m_{\text{tot}} = 27.6\,\mu_B$, for $UFe_{10}Si_2$ it is reduced to $m_{\text{tot}} = 21.9\,\mu_B$ (as per the HIA calculations). The experimental value, in comparison, is $m_{\text{tot}} = 16.5\,\mu_B$ [93].

For UFe_{12}, the MAE was calculated using both OPC and HIA approaches. The results are shown in Tab. 4.7. Of the two approaches, only HIA is in qualitative agreement with the experimental results [91, 102] — the itinerant OPC approach results in a very high negative MAE for UFe_{12}, indicating preference for an easy-plane magnetic moment, while the localized HIA approach predicts a uniaxial MAE. The MAE for $UFe_{10}Si_2$ was calculated using the HIA approach. It is significantly lower than the undoped crystal, and reasonably close to the experimental results [93].

Densities of states have been calculated for both UFe_{12} and $UFe_{10}Si_2$, using both OPC and HIA. Fig. 4.5 shows the total DOS for LSDA+U(OPC), as well as the DOS projected on the U-5f states, and the sum of the spectra for all

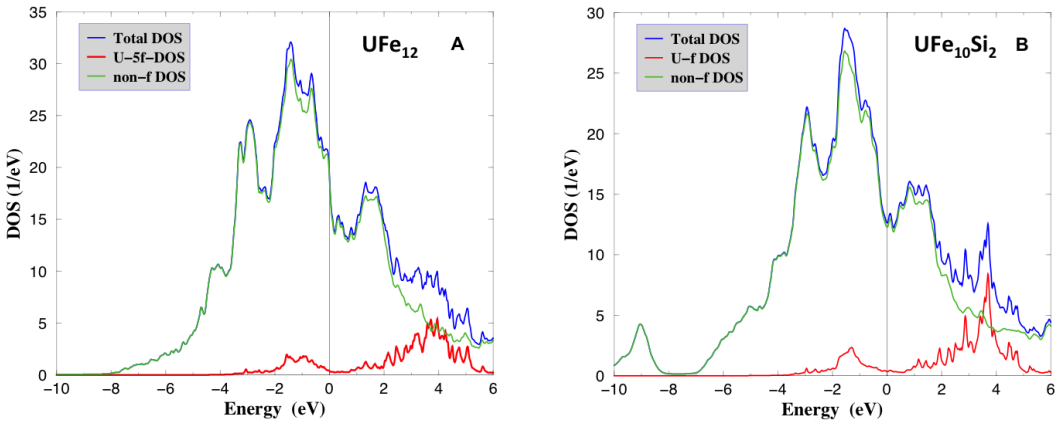

Figure 4.6: DOS in the LSDA+U(HIA) approach, for UFe_{12} (A) and $UFe_{10}Si_2$ (B) — total, projected on the U-5f states, and the difference between the latter and the former.

states other than the U-5f shell. Fig. 4.6 shows the total and U-5f DOS for LSDA+U(HIA). It can be seen that in the OPC approach there is a contribution to spectrum around the Fermi level, while in the HIA approach the impurity spectrum has a peak roughly 0.5–1.5 eV below the Fermi energy. This reflects the difference between the two LSDA+U approaches — for the itinerant OPC, the impurity electrons are more mobile than for the localized HIA, which exhibits a gap.

4.2.4 Stability

The thermodynamic stability of UFe_{12} can be calculated using the method described in Sec. 4.1.4, with LSDA. Using E_{Fe} as the energy of the iron crystal and E_{U} as the energy of the α-U crystal (the orthorhombic phase of uranium), the enthalpy is

$$\Delta H_{\mathrm{UFe_{12}}} = E_{\mathrm{UFe_{12}}} - E_{\mathrm{U}} - \frac{12}{2} E_{\mathrm{Fe}} = 3.349 \, \frac{\mathrm{eV}}{\mathrm{f.u.}}. \tag{4.19}$$

The enthalpy is positive, which indicates that UFe_{12} is not thermodynamically stable.

Applying a similar calculation to $UFe_{10}Si_2$, we get

$$\Delta H_{\mathrm{UFe_{10}Si_2}} = E_{\mathrm{UFe_{10}Si_2}} - E_{\mathrm{U}} - \frac{10}{2} E_{\mathrm{Fe}} - \frac{2}{4} E_{\mathrm{Si}} = -1.425 \, \frac{\mathrm{eV}}{\mathrm{f.u.}}, \tag{4.20}$$

where E_{Si} is the energy of the face-centered diamond cubic crystal of silicon. This enthalpy is negative, which indicates that $UFe_{10}Si_2$ is thermodynamically stable.

Within the LSDA+U(HIA) model, we can't calculate the enthalpies $\Delta H_{\mathrm{UFe_{12}}}$ and $\Delta H_{\mathrm{UFe_{10}Si_2}}$ in the aforementioned manner, because the energy functional for α-U is different from the ones for UFe_{12} and $UFe_{10}Si_2$. Nevertheless, the difference in enthalpies can be calculated:

	LSDA+U (HIA)	Requirements
K_1 $\left(\frac{\mathrm{MJ}}{\mathrm{m}^3}\right)$	2.41	4 [78]
$\mu_0 M_s$ (T)	1.54	1.25 [88]
$\mu_0 H_a$ (T)	3.92	3.75 [88]
$(BH)_{\max}$ $\left(\frac{\mathrm{KJ}}{\mathrm{m}^3}\right)$	475	460 [89]
k	1.13	1 [77]

Table 4.8: Magneto-crystalline anisotropy constant K_1, magnetic saturation moment M_s, anisotropy field H_a, maximum energy product $(BH)_{\max}$ and hardness parameter k of $UFe_{10}Si_2$ as calculated by LSDA+U(HIA) and compared to requirements from literature.

$$\begin{aligned}\Delta H_{\mathrm{UFe_{10}Si_2}} - \Delta H_{\mathrm{UFe_{12}}} &= E_{\mathrm{UFe_{10}Si_2}} - E_{\mathrm{UFe_{12}}} + \frac{2}{2}E_{\mathrm{Fe}} - \frac{2}{4}E_{\mathrm{Si}} \\ &= -3.234\,\frac{\mathrm{eV}}{\mathrm{f.u.}}. \end{aligned} \tag{4.21}$$

This indicates that the silicon-doped crystal tends to be more stable.

4.2.5 Magnetic parameters

The calculated MAE and magnetic moment of $UFe_{10}Si_2$ can be used to derive its magnetic parameters, and compare them to the requirements of a good permanent magnet, as mentioned in the chapter's introduction.

Using the first approximation for uniaxial MAE from Eq. (4.1), the magneto-crystalline anisotropy constant is found to be $K_1 = 2.41\,\frac{\mathrm{MJ}}{\mathrm{m}^3}$.

The other relevant magnetic parameters have been calculated similarly as in Sec. 4.1, and are shown in Tab. 4.8, compared to requirements taken from literature. It can be seen that while the MAE of $UFe_{10}Si_2$ is below the required standard, the rest of the required parameters are above their respective required values.

Chapter summary

Fe58-Hf25-Sb17 and $UFe_{10}Si_2$ have been studied by the appropriate DFT approaches in order to evaluate their potential as stable permanent magnets.

Out of four distinct configurations of Fe58-Hf25-Sb17, the energetically preferable configuration was found. Fe_2Hf and Fe58-Hf25-Sb17 had their total energies and magnetic moments per atom calculated using a FLAPW basis with PAW potentials and LSDA. The magnetic saturation and MAE of each material were found to be in agreement with experimental results. It was found that doping Fe_2Hf with antimony turns its MAE from positive to negative, and thus making it uniaxial. It was also found that the doping makes the crystal less thermodynamically stable. The MAE density and magnetic moment calculated using HIA were used to derive the material's anisotropy field, maximum energy product and hardness parameter. Comparing those to recommended values from literature,

it's possible to predict that the material can function as a hard magnet, albeit not a very compact one.

The magnetic moments of UFe_{12} and $UFe_{10}Si_2$ were calculated using two LSDA+U approaches, the itinerant OPC and the local HIA. Out of the two, only HIA calculations yielded a uniaxial MAE, in agreement with experimental data. This suggests that a strong local interaction plays an important role in the material's MAE. The MAE density and magnetic moment calculated using HIA were used to derive the material's other magnetic parameters, and were found to satisfy the requirements of a permanent magnet. While the substitution of two iron atoms in UFe_{12} with silicon reduces the uniaxial MAE, it significantly stabilizes it thermodynamically. $UFe_{10}Si_2$ is thus a promising candidate to be a magnetically hard material.

Conclusions

In this work, we have described methods for ab-initio computation of the electronic properties of strongly correlated materials, and applied them to a selection of systems that have experimental results available for comparison.

The first two chapters laid down the theoretical foundations of the methods used in our work, and provided some computational details. Chapter 1 focused on DFT and the various methods used as part of the self-consistent loop. In particular, the methods most relevant to our work are LSDA+U, GGA, FLAPW and PAW. Chapter 2 described the DFT+ED process, by which the results of the DFT calculation can be used to construct a discrete multi-orbital Anderson impurity model. Computational details of the diagonalization and the calculation of the spectral function have been provided.

In Chapter 3, we applied DFT+ED to three systems of cobalt impurities coupled to metals, for the purpose of studying the conductive properties of the systems. The first system, a cobalt atom in bulk copper, was found to produce observables that partially agree with existing DFT+QMC results. The second and third system, a cobalt adatom on a copper surface with and without a Cu_2N layer, were found to predict a differential conductance curve that agree with experimental measurements. Moreover, for $CoCu_{15}$ and $Co@Cu_2N/Cu\,(001)$ the exact diagonalization made it possible to detect a singlet as the ground state, which, along with the resonance at Fermi level, indicates the presence of a Kondo effect.

In Chapter 4, we studied the magnetic properties of the alloys Fe_2Hf and Fe58-Hf25-Sb17, as well as UFe_{12} and $UFe_{10}Si_2$. We found the configuration of Fe58-Hf25-Sb17 with the lowest energy and calculated its MAE and magnetic saturation, which were found to be in reasonable agreement with experiment. The other magnetic parameters were calculated and compared to recommended values from literature.

$UFe_{10}Si_2$ was used as a test case for comparing two LSDA+U approaches, an itinerant and a local one. The local method yielded a uniaxial MAE, in qualitative agreement with experimental data, while the itinerant one didn't. The local method was then used to model the magnetic properties of $UFe_{10}Si_2$, which were found to fulfill the needed criteria for a magnetically hard material. The calculated enthalpies of formation showed that the doping of Fe_2Hf by antimony makes it slightly more unstable, whereas the doping of UFe_{12} by silicon stabilizes it.

Overall, this work shows that DFT+ED and LSDA+U(HIA) are capable of producing results that qualitatively agree with experiments and other computational methods, as well as giving new interpretations of existing phenomena.

The work also points to Fe58-Hf25-Sb17 and $UFe_{10}Si_2$ as promising permanent magnets.

As computer clusters increase in processing power and storage, ab-initio calculation of the electronic properties of materials becomes less time- and power-consuming and more accessible to researchers, increasing the size of the systems to which computational methods can be applied. However, the trend depends on the constant miniaturization of electronic components, and as they shrink to the atomic level, research into the properties of many-body quantum systems is in constant demand. Essentially, Moore's law affects both sides of the equation, perpetually giving computational physicists more ability, but also more demands and challenges. This work is a contribution to the effort to keep the feedback loop going.

Bibliography

[1] X. Zhou, W.-S. Lee, M. Imada, N. Trivedi, P. Phillips, H.-Y. Kee, P. Törmä, and M. Eremets. High-temperature superconductivity. *Nat. Rev. Phys.*, 3(7):462–465, 2021.

[2] M. Imada, A. Fujimori, and Y. Tokura. Metal-insulator transitions. *Reviews of modern physics*, 70(4):1039, 1998.

[3] A. C. Hewson. *The Kondo Problem to Heavy Fermions*, volume 2 of *Cambridge Studies in Magnetism*. Cambridge University Press, Cambridge, 1993.

[4] P. Hohenberg and W. Kohn. Inhomogeneous electron gas. *Phys. Rev.*, 136(3B):B864, 1964.

[5] R. G. Parr and W. Yang. *Density-Functional Theory of Atoms and Molecules*. Oxford University Press, New York, 1989.

[6] R. M. Dreizler and E. K. Gross. *Density functional theory: an approach to the quantum many-body problem*. Springer Science & Business Media, 2012.

[7] C. A. Ullrich. *Time-Dependent Density-Functional Theory*. Oxford Graduate Texts. Oxford University Press, Oxford, 2012.

[8] D. M. Ceperley and B. J. Alder. Ground state of the electron gas by a stochastic method. *Phys. Rev. Lett.*, 45(7):566, 1980.

[9] S. H. Vosko, L. Wilk, and M. Nusair. Accurate spin-dependent electron liquid correlation energies for local spin density calculations: a critical analysis. *Can. J. Phys.*, 58(8):1200–1211, 1980.

[10] D. J. Singh and L. Nordstrom. *Planewaves, Pseudopotentials, and the LAPW method*. Springer Science & Business Media, 2006.

[11] U. Von Barth and L. Hedin. A local exchange-correlation potential for the spin polarized case: I. *J. Phys. C: Solid State Phys.*, 5(13):1629, 1972.

[12] V. I. Anisimov, F. Aryasetiawan, and A. I. Lichtenstein. First-principles calculations of the electronic structure and spectra of strongly correlated systems: the LDA+U method. *J. Phys. Condens. Matter*, 9(4):767, 1997.

[13] I. Solovyev, A. Liechtenstein, and K. Terakura. Is Hund's second rule responsible for the orbital magnetism in solids? *Phys. Rev. Lett.*, 80(26):5758, 1998.

[14] A. Liechtenstein, V. I. Anisimov, and J. Zaanen. Density-functional theory and strong interactions: Orbital ordering in Mott-Hubbard insulators. *Phys. Rev. B*, 52(8):R5467, 1995.

[15] C. Herring. A new method for calculating wave functions in crystals. *Phys. Rev.*, 57(12):1169, 1940.

[16] V. Anisimov and O. Gunnarsson. Density-functional calculation of effective coulomb interactions in metals. *Phys. Rev. B*, 43(10):7570, 1991.

[17] E. Şaşıoğlu, C. Friedrich, and S. Blügel. Effective coulomb interaction in transition metals from constrained random-phase approximation. *Phys. Rev. B*, 83:121101, Mar 2011.

[18] I. Solovyev, P. Dederichs, and V. Anisimov. Corrected atomic limit in the local-density approximation and the electronic structure of d impurities in Rb. *Phys. Rev. B*, 50(23):16861, 1994.

[19] V. I. Anisimov, J. Zaanen, and O. K. Andersen. Band theory and mott insulators: Hubbard U instead of Stoner I. *Phys. Rev. B*, 44(3):943, 1991.

[20] S. L. Dudarev, G. A. Botton, S. Y. Savrasov, C. Humphreys, and A. P. Sutton. Electron-energy-loss spectra and the structural stability of nickel oxide: An LSDA+U study. *Phys. Rev. B*, 57(3):1505, 1998.

[21] A. B. Shick, A. Liechtenstein, and W. E. Pickett. Implementation of the LDA+U method using the full-potential linearized augmented plane-wave basis. *Phys. Rev. B*, 60(15):10763, 1999.

[22] J. P. Perdew, K. Burke, and M. Ernzerhof. Generalized gradient approximation made simple. *Phys. Rev. Lett.*, 77(18):3865, 1996.

[23] G. Oliver and J. Perdew. Spin-density gradient expansion for the kinetic energy. *Phys. Rev. A*, 20(2):397, 1979.

[24] E. H. Lieb and S. Oxford. Improved lower bound on the indirect Coulomb energy. *Int. J. Quantum Chem.*, 19(3):427–439, 1981.

[25] J. P. Perdew, K. Burke, and Y. Wang. Generalized gradient approximation for the exchange-correlation hole of a many-electron system. *Phys. Rev. B*, 54(23):16533, 1996.

[26] Y. Zhang and W. Yang. Comment on "generalized gradient approximation made simple". *Phys. Rev. Lett.*, 80(4):890, 1998.

[27] B. Hammer, L. B. Hansen, and J. K. Nørskov. Improved adsorption energetics within density-functional theory using revised Perdew-Burke-Ernzerhof functionals. *Phys. Rev. B*, 59(11):7413, 1999.

[28] N. W. Ashcroft and N. D. Mermin. *Solid state physics*. Cengage Learning, 2022.

[29] A. Baldereschi. Mean-value point in the Brillouin zone. *Phys. Rev. B*, 7(12):5212, 1973.

[30] D. J. Chadi and M. L. Cohen. Special points in the Brillouin zone. *Phys. Rev. B*, 8(12):5747, 1973.

[31] H. J. Monkhorst and J. D. Pack. Special points for Brillouin-zone integrations. *Phys. Rev. B*, 13(12):5188, 1976.

[32] P. E. Blöchl, O. Jepsen, and O. K. Andersen. Improved tetrahedron method for Brillouin-zone integrations. *Phys. Rev. B*, 49(23):16223, 1994.

[33] E. Wimmer, H. Krakauer, M. Weinert, and A. Freeman. Full-potential self-consistent linearized-augmented-plane-wave method for calculating the electronic structure of molecules and surfaces: O_2 molecule. *Phys. Rev. B*, 24(2):864, 1981.

[34] M. Weinert, E. Wimmer, and A. Freeman. Total-energy all-electron density functional method for bulk solids and surfaces. *Phys. Rev. B*, 26(8):4571, 1982.

[35] M. Weinert. Solution of Poisson's equation: Beyond Ewald-type methods. *J. Math. Phys.*, 22(11):2433–2439, 1981.

[36] G. Kresse and D. Joubert. From ultrasoft pseudopotentials to the projector augmented-wave method. *Phys. Rev. B*, 59(3):1758, 1999.

[37] P. E. Blöchl. Projector augmented-wave method. *Phys. Rev. B*, 50(24):17953, 1994.

[38] D. Hamann, M. Schlüter, and C. Chiang. Norm-conserving pseudopotentials. *Phys. Rev. Lett.*, 43(20):1494, 1979.

[39] G. B. Bachelet, D. R. Hamann, and M. Schlüter. Pseudopotentials that work: From H to Pu. *Phys. Rev. B*, 26(8):4199, 1982.

[40] D. Vanderbilt. Soft self-consistent pseudopotentials in a generalized eigenvalue formalism. *Phys. Rev. B*, 41(11):7892, 1990.

[41] P. W. Anderson. Localized magnetic states in metals. *Phys. Rev.*, 124:41–53, Oct 1961.

[42] O. Gunnarsson and K. Schönhammer. Electron spectroscopies for ce compounds in the impurity model. *Phys. Rev. B*, 28(8):4315, 1983.

[43] O. Gunnarsson, O. K. Andersen, O. Jepsen, and J. Zaanen. Density-functional calculation of the parameters in the Anderson model: Application to Mn in CdTe. *Phys. Rev. B*, 39:1708–1722, Jan 1989.

[44] J. Kolorenč, A. B. Shick, and A. I. Lichtenstein. Electronic structure and core-level spectra of light actinide dioxides in the dynamical mean-field theory. *Phys. Rev. B*, 92:085125, Aug 2015.

[45] E. Pavarini. Crystal-field theory, tight-binding method and Jahn-Teller effect. *Correlated electrons: from models to materials*, 2:6–2, 2012.

[46] T. Wolfram and Ş. Ellialtıoğlu. *Applications of group theory to atoms, molecules, and solids*. Cambridge University Press, 2014.

[47] A. Georges, L. d. Medici, and J. Mravlje. Strong correlations from Hund's coupling. *Annu. Rev. Condens. Matter Phys.*, 4(1):137–178, 2013.

[48] A. MacDonald, W. Picket, and D. Koelling. A linearised relativistic augmented-plane-wave method utilising approximate pure spin basis functions. *J. Phys. C: Solid State Phys.*, 13(14):2675, 1980.

[49] E. Gull, A. J. Millis, A. I. Lichtenstein, A. N. Rubtsov, M. Troyer, and P. Werner. Continuous-time Monte Carlo methods for quantum impurity models. *Rev. Mod. Phys.*, 83(2):349, 2011.

[50] N. Metropolis, A. W. Rosenbluth, M. N. Rosenbluth, A. H. Teller, and E. Teller. Equation of state calculations by fast computing machines. *J. Chem. Phys.*, 21(6):1087–1092, 1953.

[51] W. K. Hastings. Monte Carlo sampling methods using Markov chains and their applications. *Biometrika*, 57(1):97–109, 04 1970.

[52] C. Zhu, R. H. Byrd, P. Lu, and J. Nocedal. Algorithm 778: L-BFGS-B: Fortran subroutines for large-scale bound-constrained optimization. *ACM Trans. Math. Software*, 23(4):550–560, 1997.

[53] J. L. Morales and J. Nocedal. Remark on "Algorithm 778: L-BFGS-B: Fortran subroutines for large-scale bound constrained optimization". *ACM Trans. Math. Software*, 38(1):1–4, 2011.

[54] R. B. Lehoucq, D. C. Sorensen, and C. Yang. *ARPACK users' guide: solution of large-scale eigenvalue problems with implicitly restarted Arnoldi methods*. SIAM, 1998.

[55] C. Lanczos. An iteration method for the solution of the eigenvalue problem of linear differential and integral operators. *J. Res. Natl. Bur. Stand.*, 45(4):255–282, 1950.

[56] R. Mozara, M. Valentyuk, I. Krivenko, E. Şaşıoğlu, J. Kolorenč, and A. I. Lichtenstein. Cobalt adatoms on graphene: Effects of anisotropies on the correlated electronic structure. *Phys. Rev. B*, 97(8):085133, 2018.

[57] B. Surer, M. Troyer, P. Werner, T. O. Wehling, A. M. Läuchli, A. Wilhelm, and A. I. Lichtenstein. Multiorbital Kondo physics of Co in Cu hosts. *Phys. Rev. B*, 85(8):085114, 2012.

[58] N. Knorr, M. A. Schneider, L. Diekhöner, P. Wahl, and K. Kern. Kondo effect of single Co adatoms on Cu surfaces. *Phys. Rev. Lett.*, 88(9):096804, 2002.

[59] J. Kondo. Resistance minimum in dilute magnetic alloys. *Prog. Theor. Phys.*, 32(1):37–49, 1964.

[60] M. Jarrell and J. E. Gubernatis. Bayesian inference and the analytic continuation of imaginary-time quantum Monte Carlo data. *Phys. Rep.*, 269(3):133–195, 1996.

[61] J. Hubbard. Electron correlations in narrow energy bands. II. The degenerate band case. *Proc. R. Soc. A*, 277(1369):237–259, 1964.

[62] G. Kresse and J. Furthmüller. Efficiency of ab-initio total energy calculations for metals and semiconductors using a plane-wave basis set. *Comput. Mater. Sci.*, 6(1):15–50, 1996.

[63] A. Valli, M. P. Bahlke, A. Kowalski, M. Karolak, C. Herrmann, and G. Sangiovanni. Kondo screening in Co adatoms with full coulomb interaction. *Phys. Rev. Res.*, 2(3):033432, 2020.

[64] K. R. Patton, S. Kettemann, A. Zhuravlev, and A. Lichtenstein. Spin-polarized tunneling microscopy and the Kondo effect. *Phys. Rev. B*, 76(10):100408, 2007.

[65] T. Wehling, H. Dahal, A. I. Lichtenstein, M. Katsnelson, H. Manoharan, and A. Balatsky. Theory of Fano resonances in graphene: The influence of orbital and structural symmetries on STM spectra. *Phys. Rev. B*, 81(8):085413, 2010.

[66] M. Plihal and J. W. Gadzuk. Nonequilibrium theory of scanning tunneling spectroscopy via adsorbate resonances: Nonmagnetic and Kondo impurities. *Phys. Rev. B*, 63(8):085404, 2001.

[67] J. Tersoff and D. R. Hamann. Theory of the scanning tunneling microscope. *Phys. Rev. B*, 31(2):805, 1985.

[68] C. F. Hirjibehedin, C.-Y. Lin, A. F. Otte, M. Ternes, C. P. Lutz, B. A. Jones, and A. J. Heinrich. Large magnetic anisotropy of a single atomic spin embedded in a surface molecular network. *Science*, 317(5842):1199–1203, 2007.

[69] J. C. Oberg, M. R. Calvo, F. Delgado, M. Moro-Lagares, D. Serrate, D. Jacob, J. Fernández-Rossier, and C. F. Hirjibehedin. Control of single-spin magnetic anisotropy by exchange coupling. *Nat. Nanotechnol.*, 9(1):64, 2014.

[70] A. F. Otte, M. Ternes, K. Von Bergmann, S. Loth, H. Brune, C. P. Lutz, C. F. Hirjibehedin, and A. J. Heinrich. The role of magnetic anisotropy in the Kondo effect. *Nat. Phys.*, 4(11):847–850, 2008.

[71] J. Fernández-Rossier. Theory of single-spin inelastic tunneling spectroscopy. *Phys. Rev. Lett.*, 102(25):256802, 2009.

[72] S. Loth, C. P. Lutz, and A. J. Heinrich. Spin-polarized spin excitation spectroscopy. *New J. Phys.*, 12(12):125021, 2010.

[73] M. Etzkorn et al. Comparing XMCD and DFT with STM spin excitation spectroscopy for Fe and Co adatoms on Cu_2N/Cu (100). *Phys. Rev. B*, 92(18):184406, 2015.

[74] V. Mazurenko, S. Iskakov, A. Rudenko, I. Kashin, O. Sotnikov, M. Valentyuk, and A. I. Lichtenstein. Correlation effects in insulating surface nanostructures. *Phys. Rev. B*, 88(8):085112, 2013.

[75] L. Kyvala, M. Tchaplianka, A. B. Shick, S. Khmelevskyi, and D. Legut. Large uniaxial magnetic anisotropy of hexagonal Fe-Hf-Sb alloys. *Crystals*, 10(6):430, 2020.

[76] D. Goll, T. Gross, R. Loeffler, U. Pflanz, T. Vogel, A. Kopp, T. Grubesa, and G. Schneider. Hard magnetic off-stoichiometric $(Fe, Sb)_{2+x} Hf_{1-x}$ intermetallic phase. *Phys. Status Solidi–Rapid Res. Lett.*, 11(9):1700184, 2017.

[77] R. Skomski and J. Coey. Magnetic anisotropy – how much is enough for a permanent magnet? *Scr. Mater.*, 112:3–8, 2016.

[78] K. Skokov and O. Gutfleisch. Heavy rare earth free, free rare earth and rare earth free magnets-vision and reality. *Scr. Mater.*, 154:289–294, 2018.

[79] D. Givord, H. Li, and R. P. De La Bâthie. Magnetic properties of Y_2Fe_14B and Nd_2Fe_14B single crystals. *Solid State Commun.*, 51(11):857–860, 1984.

[80] M. J. Mehl, D. Hicks, C. Toher, O. Levy, R. M. Hanson, G. Hart, and S. Curtarolo. The aflow library of crystallographic prototypes: part 1. *Comput. Mater. Sci.*, 136:S1–S828, 2017.

[81] K. v. Buschow, P. Van Engen, and R. Jongebreur. Magneto-optical properties of metallic ferromagnetic materials. *J. Magn. Magn. Mat.*, 38(1):1–22, 1983.

[82] Fe_2Hf ($HfFe_2$ ht1) crystal structure: Datasheet from "pauling file multinaries edition – 2012" in springermaterials (https://materials.springer.com/isp/crystallographic/docs/sd_0261733). Copyright 2016 Springer-Verlag Berlin Heidelberg & Material Phases Data System (MPDS), Switzerland & National Institute for Materials Science (NIMS), Japan.

[83] K. Ikeda. Ferromagnetism in hexagonal and cubic Fe_2Hf compounds. *Int. J. Mater. Res.*, 68(3):195–198, 1977.

[84] L. L. Snead, D. T. Hoelzer, M. Rieth, and A. A. Nemith. Refractory alloys: Vanadium, niobium, molybdenum, tungsten. In *Structural alloys for nuclear energy applications*, pages 585–640. Elsevier, 2019.

[85] J. Booth. Ferromagnetic transition metal intermetallic compounds. *Handbook of Ferromagnetic Materials*, 4:211–308, 1988.

[86] A. B. Shick, D. Novikov, and A. J. Freeman. Relativistic spin-polarized theory of magnetoelastic coupling and magnetic anisotropy strain dependence: Application to Co/Cu (001). *Phys. Rev. B*, 56(22):R14259, 1997.

[87] P. Pulay. Convergence acceleration of iterative sequences. the case of SCF iteration. *Chem. Phys. Lett.*, 73(2):393–398, 1980.

[88] A. Landa, P. Söderlind, E. E. Moore, and A. Perron. Thermodynamics and magnetism of $SmFe_12$ compound doped with Co and Ni: An ab initio study. *Appl. Sci.*, 12(10):4860, 2022.

[89] J. Herbst. $R_2Fe_{14}B$ materials: Intrinsic properties and technological aspects. *Rev. Mod. Phys.*, 63(4):819, 1991.

[90] D. W. Oxtoby, H. P. Gillis, and L. J. Butler. *Principles of modern chemistry*. Cengage learning, 2015.

[91] T. Berlureau, B. Chevalier, P. Gravereau, L. Fournes, and J. Etourneau. Investigation of the U $(Fe_{10-x}Co_x)$ Si_2 ternary system with $0 \leq x \leq 10$ by x-ray powder diffraction, magnetic and 57fe mössbauer studies. *J. Magn. Magn. Mat.*, 102(1-2):166–174, 1991.

[92] A. Andreev, S. Andreev, and E. Tarasov. Magnetic properties of $UFe_{12-x}Si_x$. *Journal of the Less Common Metals*, 167(2):255–259, 1991.

[93] A. Andreev, M. Bartashevich, H. A. Katori, and T. Goto. Magnetic anisotropy and magnetostriction of UFe_10Si_2. *J. Alloys Compd.*, 216(2):221–225, 1995.

[94] A. M. Boring and J. L. Smith. Plutonium condensed-matter physics. *Los Alamos Science*, 26:90, 2000.

[95] K. T. Moore and G. van der Laan. Nature of the $5f$ states in actinide metals. *Rev. Mod. Phys.*, 81(1):235, 2009.

[96] O. Eriksson, B. Johansson, and M. Brooks. Meta-magnetism in UCoAl. *J. Phys. Condens. Matter*, 1(25):4005, 1989.

[97] L. Nugent. Theory of the tetrad effect in the lanthanide (III) and actinide (III) series. *J. inorg. nucl. chem.*, 32(11):3485–3491, 1970.

[98] A. B. Shick and W. E. Pickett. Spin-orbit coupling induced degeneracy in the anisotropic unconventional superconductor UTe_2. *Phys. Rev. B*, 100(13):134502, 2019.

[99] A. B. Shick, S.-i. Fujimori, and W. E. Pickett. UTe_2: A nearly insulating half-filled $j = \frac{5}{2} 5f^3$ heavy-fermion metal. *Phys. Rev. B*, 103(12):125136, 2021.

[100] K. Stevens. Matrix elements and operator equivalents connected with the magnetic properties of rare earth ions. *Proc. Phys. Soc. A*, 65(3):209, 1952.

[101] I. Campbell. Indirect exchange for rare earths in metals. *J. Phys. F: Met. Phys.*, 2(3):L47, 1972.

[102] M. Brooks, O. Eriksson, and B. Johansson. $3d$-$5d$ band magnetism in rare earth transition metal intermetallics: $LuFe_2$. *J. Phys. Condens. Matter*, 1(34):5861, 1989.

List of Figures

List of Tables

List of Publications

This thesis is based on the following publications:

L. Kyvala, M. Tchaplianka, A. B. Shick, S. Khmelevskyi, and D. Legut. Large uniaxial magnetic anisotropy of hexagonal Fe-Hf-Sb alloys. *Crystals*, 10(6):430, 2020.

M. Tchaplianka, A. B. Shick, and A. I. Lichtenstein. Valence fluctuations and Kondo resonance in Co adatom on Cu_2N/Cu (100) surface: DFT+ED study. *New J. Phys.*, 23(10):103037, 2021.

M. Tchaplianka, A. B. Shick, and J. Kolorenč. Modeling of Co impurity in Cu host using DFT+ED. *J. Phys. Conf. Ser.*, volume 2164, page 012045. IOP Publishing, 2022.

A. B. Shick, M. Tchaplianka, and A. I. Lichtenstein. Spin-orbit coupling and Kondo resonance in the Co adatom on the Cu (100) surface: DFT plus exact diagonalization study. *Phys. Rev. B*, 106(24):245115, 2022.

A. B. Shick, I. Halevy, M. Tchaplianka, and D. Legut. Itinerant-localized dichotomy in magnetic anisotropic properties of U-based ferromagnets. *Sci. Rep.*, 13(1):2646, 2023.

List of Abbreviations

- AIM — Anderson impurity model
- APW — augmented planewave
- DMFT — dynamical mean field theory
- CF — crystal field
- DFT — density functional theory
- DOS — density of states
- ED — exact diagonalization
- FLAPW — full-potential linearized augmented planewaves
- FWHM — full width at half maximum
- f.u. — formula unit
- GGA — generalized gradient approximation
- HIA — Hubbard-I approximation
- LAPW — linearized augmented planewave
- LDA — local density approximation
- LSDA — local spin-density approximation
- MAE — magnetocrystalline anisotropy energy
- MFT — mean field theory
- MT — muffin-tin
- OPC — orbital polarization correction
- PAW — projector-augmented planewave
- PBE — Perdew-Burke-Ernzerhof
- CT-QMC — continuous-time quantum Monte Carlo
- SIAM — single-impurity Anderson model
- STS — spin tunneling spectroscopy

- VASP — Vienna Ab-Initio Simulation Package
- xc — exchange-correlation

Appendix A

Attachments

A.1 Notation

The notation in this work is the product of compromise. Ideally, it should adhere to convention, be consistent and not be too busy. Since those three goals are contradictory at times, choices had to be made. This section describes in brief the notation used. Examples are shown in brackets.

- Constants are depicted using normal letters, either small or capital (k_B, B)
- Vectors in real space or the reciprocal space are depicted using a bold letter ($\mathbf{k}$).
- Quantum operators and matrices are depicted as capital letters with a hat ($\hat{H}$). Operators which are applied to a specific set of indices are depicted without a hat, as are matrix elements ($H_{m\sigma}$). Creation/annihilation operators are depicted with small letters ($d_{m\sigma}$).
- Functions are depicted with the domain parameter in round brackets ($\rho(\mathbf{r})$). The derivative of a function omits the parameter.
- Functionals are depicted with square brackets ($E[\rho]$). The function's parameter is generally omitted.
- Quantum states are depicted as wavefunctions ($\phi_{n\mathbf{k}}(\mathbf{r})$) or as vectors in Dirac notation ($|\phi\rangle$).
- A group of parameters enumerated by indices is depicted in curly brackets ($\{\epsilon_{km}, V_{km}\}$). The range of the indices is omitted.

A.2 Metropolis-Hastings algorithm

In CT-QMC, each configuration can be specified by the variable-length vector $\boldsymbol{\tau}$ which contains, in order, every segment (τ_i', τ_i) in the configuration, where the segments don't overlap (i.e. $\tau_{i-1} < \tau_i'$ and $\tau_i < \tau_{i+1}'$). Under the Monte Carlo method, the summation is performed by stochastically moving from one configuration to a neighboring one over a large number of steps. During each step, the

current configuration either undergoes a transition or stays the same. A transition is performed by either removing one of the segments in $\boldsymbol{\tau}$, or by inserting a new one in an unoccupied space. The probability of each transition is set to preserve detailed balance — every possible transition should be in equilibrium with its opposite [50, 51].

$\boldsymbol{\tau}'$ will represent a configuration where a new segment is inserted into $\boldsymbol{\tau}$. $p_{\boldsymbol{\tau}}$ is the probability weight of configuration $\boldsymbol{\tau}$:

$$p_{\boldsymbol{\tau}} = w_{\mathrm{loc}}\left(\boldsymbol{\tau}\right) \mathrm{d}\tau_1 \cdots \mathrm{d}\tau_n \mathrm{d}\tau'_1 \cdots \mathrm{d}\tau'_n,$$

with the local state space density

$$w_{\mathrm{loc}}\left(\boldsymbol{\tau}\right) = \det\left[\boldsymbol{\Delta}^m\right] \mathrm{Tr}\left[\hat{T}_\tau e^{-\beta \hat{H}_{\mathrm{loc}}} d_{m\sigma}(\tau_n) d^\dagger_{m\sigma}(\tau'_n) \cdots d_{m\sigma}(\tau_1) d^\dagger_{m\sigma}(\tau'_1)\right].$$

The probability densities of the insertion and its reverse process are $W_{\boldsymbol{\tau}\to\boldsymbol{\tau}'}$ and $W_{\boldsymbol{\tau}'\to\boldsymbol{\tau}}$ respectively. Detailed balance is maintained when

$$p_{\boldsymbol{\tau}} W_{\boldsymbol{\tau}\to\boldsymbol{\tau}'} = p_{\boldsymbol{\tau}'} W_{\boldsymbol{\tau}'\to\boldsymbol{\tau}} \tag{A.1}$$

Under the Metropolis-Hastings algorithm, in order for a transition to manifest, it must pass through two steps — proposal and acceptance. Its total probability density is then the product of the probability densities of each step: $W = W^{\mathrm{prop}} W^{\mathrm{acc}}$.

There is a degree of freedom in choosing the acceptance probability densities. They are chosen to be as large as possible in order to make the process converge to equilibrium as fast as possible and to explore as much of the configuration space as it can within the given number of steps:

$$W^{\mathrm{acc}}_{\boldsymbol{\tau}\to\boldsymbol{\tau}'} = \min\left[1, R_{\boldsymbol{\tau}\to\boldsymbol{\tau}'}\right], \tag{A.2}$$

$$W^{\mathrm{acc}}_{\boldsymbol{\tau}'\to\boldsymbol{\tau}} = \min\left[1, \frac{1}{R_{\boldsymbol{\tau}\to\boldsymbol{\tau}'}}\right], \tag{A.3}$$

where $R_{\boldsymbol{\tau}\to\boldsymbol{\tau}'}$ is the acceptance ratio:

$$R_{\boldsymbol{\tau}\to\boldsymbol{\tau}'} \equiv \frac{p_{\boldsymbol{\tau}'} W^{\mathrm{prop}}_{\boldsymbol{\tau}'\to\boldsymbol{\tau}}}{p_{\boldsymbol{\tau}} W^{\mathrm{prop}}_{\boldsymbol{\tau}\to\boldsymbol{\tau}'}}. \tag{A.4}$$

For CT-HYB, the proposition of a segment is done in two steps - selecting the segment's starting time τ'_i from 0 to β (which is rejected if it lies on an existing segment), and then selecting the segment's endpoint τ_i in the interval $\left(\tau'_i, \tau'_{i+1}\right)$ of length $l_{\max}$. The proposition probability is

$$W^{\mathrm{prop}}_{\boldsymbol{\tau}\to\boldsymbol{\tau}'} = \frac{\mathrm{d}\tau}{\beta} \cdot \frac{\mathrm{d}\tau}{l_{\max}}. \tag{A.5}$$

The deletion pribability density is equally divided between all vertices that can be removed:

$$W^{\text{prop}}_{\boldsymbol{\tau}'\to\boldsymbol{\tau}} = \frac{1}{n+1}. \tag{A.6}$$

The acceptance ratio is then

$$R_{\boldsymbol{\tau}\to\boldsymbol{\tau}'} = \frac{\beta l_{\max}}{n+1} \cdot \frac{w_{\text{loc}}\left(\boldsymbol{\tau}'\right) \det\left[\Delta\left(\boldsymbol{\tau}'\right)\right]}{w_{\text{loc}}\left(\boldsymbol{\tau}\right) \det\left[\Delta\left(\boldsymbol{\tau}\right)\right]}. \tag{A.7}$$

Since the insertion and removal of anti-segments is mathematically equivalent, the acceptance ratio for them is the same as in Eq. (A.7).

The proposal probability of shifting a point is identical to the proposal probability of the inverse move. Their acceptance ratio is then

$$R_{\boldsymbol{\tau}\to\boldsymbol{\tau}'} = \frac{w_{\text{loc}}\left(\boldsymbol{\tau}'\right) \det\left[\Delta\left(\boldsymbol{\tau}'\right)\right]}{w_{\text{loc}}\left(\boldsymbol{\tau}\right) \det\left[\Delta\left(\boldsymbol{\tau}\right)\right]}. \tag{A.8}$$

A.3 Derivation of the Kondo model

The following model will model the lowest states of a discrete AIM using a simplified single-impurity Anderson model, and then map it on the Kondo model using a procedure described in Ref. [3]

The SIAM Hamiltonian is

$$\hat{H} = \sum_{\sigma} \epsilon_d n^d_\sigma + \frac{1}{2}\sum_{\sigma} U n^d_\sigma n^d_{\bar{\sigma}} + \sum_{k\sigma} \epsilon_k n^b_{k\sigma} + \sum_{k\sigma} \left(V_k d^\dagger_\sigma b_{k\sigma} + \text{h.c.} \right), \tag{A.9}$$

The impurity's possible states can be represented by its occupation, as $|0\rangle$, $|1\rangle$ or $|2\rangle$ (The fact that $|1\rangle$ represents two degenerate states is not a problem for our purposes), with the energies

$$E_0 = 0, \tag{A.10}$$
$$E_1 = \epsilon_d, \tag{A.11}$$
$$E_2 = 2\epsilon_d + U. \tag{A.12}$$

Assuming $\epsilon_d < 0$, E_1 is the impurity's lowest state, and E_0 and E_2 are excitations.

The space of the system's states will be subdivided into three partitions, each corresponding to one of the states $|0\rangle$, $|1\rangle$, $|2\rangle$. The projection operators $P_n \equiv |n\rangle\langle n|$ can be used to partition the system's Hamiltonian into blocks:

$$\hat{H}_{mn} \equiv \hat{P}_m \hat{H} \hat{P}_n$$

represents the coupling of $|m\rangle$ states to $|n\rangle$ states. The operator $\hat{P}_n$ is hermitian, therefore so is the matrix of $\hat{H}_{mn}$:

$$\hat{H}_{mn} = \hat{H}^\dagger_{nm}.$$

We're looking for an effective Hamiltonian for a half-occupied impurity — a Hamiltonian $\hat{H}'_{11}$ whose eigenstates are $|1\rangle$, with the same eigenenergies E as the full Hamiltonian. This is done by downfolding it to the $|1\rangle$ subspace :

$$\hat{H}'_{11} = \hat{H}_{11} + \hat{H}_{10}\left(E - \hat{H}_{00}\right)^{-1}\hat{H}_{01} + \hat{H}_{12}\left(E - \hat{H}_{22}\right)^{-1}\hat{H}_{21}, \tag{A.13}$$

where E is the total energy of the system — the sum of occupied bath levels and a single occupied impurity level, plus the impurity-bath coupling term:

$$E = E_{\text{bath}} + \epsilon_m + \mathcal{O}\left(V^2\right). \tag{A.14}$$

The two additional elements describe virtual excitations. The former term describes a process where the impurity loses an electron for the bath and then gains another one. The second term describes a process where the impurity gains an electron first and then loses an electron.

In AIM terms, the relevant transition elements (in which the impurity gains an electron) are

$$\begin{aligned}\hat{H}_{10} &= \sum_{k\sigma} V_k d^\dagger_\sigma \left(1 - n^d_{\bar{\sigma}}\right) b_{k\sigma},\\ \hat{H}_{12} &= \sum_{k\sigma} V_k d^\dagger_\sigma n^d_{\bar{\sigma}} b_{k\sigma},\end{aligned}$$

where $\bar{\sigma}$ is the opposite spin from σ.

The virtual excitation terms of Eq. (A.13) can be calculated in the first order by neglecting the coupling energy in Eq. (A.14). In the first transition, the impurity energy goes to 0, and the bath gains the energy ϵ_k of the newly-occupied bath level. The term is thus

$$\begin{aligned}\hat{H}_{10}\left(E - \hat{H}_{00}\right)^{-1}\hat{H}_{01} &= \sum_{kk'\sigma\sigma'} V^\star_k d^\dagger_\sigma \left(1 - n^d_{\bar{\sigma}}\right) b_{k\sigma} \frac{1}{E - (E_{\text{bath}} + \epsilon_k)} V_{k'} d_{\sigma'} \left(1 - n^d_{\bar{\sigma}'}\right) b^\dagger_{k'\sigma'}\\ &\approx \sum_{kk'\sigma\sigma'} \frac{V^\star_k V_k}{\epsilon_d - \epsilon_k} d^\dagger_\sigma b_{k\sigma} d_{\sigma'} b^\dagger_{k\sigma'} \left(1 - n^d_{\bar{\sigma}'}\right).\end{aligned} \tag{A.15}$$

The second excitation has an impurity and energy of $2\epsilon_m + U$ and a bath energy that loses the energy of the transitioning bath level. The term is

$$\begin{aligned}\hat{H}_{12}\left(E - \hat{H}_{22}\right)^{-1}\hat{H}_{21} &= \sum_{kk'\sigma\sigma'} V^\star_k d^\dagger_\sigma b_{k\sigma} \frac{1}{E - (2\epsilon_d + U + E_{\text{bath}} - \epsilon_{k'})} V_{k'} d_{\sigma'} b^\dagger_{k'\sigma'} n^d_{\bar{\sigma}'}\\ &\approx \sum_{kk'\sigma\sigma'} \frac{-V^\star_k V_{k'}}{\epsilon_d + U - \epsilon_{k'}} d^\dagger_\sigma b_{k\sigma} d_{\sigma'} b^\dagger_{k\sigma'} n^d_{\bar{\sigma}'}.\end{aligned} \tag{A.16}$$

Assuming a spin parallel to the z-axis, the up and down spins don't hybridize, allowing us to remove all terms where $\sigma \neq \sigma'$.

Substituting Eq. (A.15) and Eq. (A.16) into Eq. (A.13), we get

$$\hat{H}'_{11} - \hat{H}_{11} = \sum_{kk'\sigma} \left(\frac{V_k^\star V_k}{\epsilon_d - \epsilon_k} d_\sigma^\dagger b_{k\sigma} d_\sigma b_{k\sigma}^\dagger \left(1 - n_{\bar{\sigma}}^d\right) - \frac{V_k^\star V_{k'}}{\epsilon_d + U - \epsilon_{k'}} d_\sigma^\dagger b_{k\sigma} d_\sigma b_{k\sigma}^\dagger n_{\bar{\sigma}}^d \right),$$

$$= \sum_{kk'} \left(\frac{V_k^\star V_{k'}}{\epsilon_d + U - \epsilon_{k'}} + \frac{V_k^\star V_{k'}}{\epsilon_k - \epsilon_d} \right) \left(n_\uparrow^d - n_\downarrow^d\right) \left(b_{k\uparrow}^\dagger b_{k'\uparrow} - b_{k\downarrow}^\dagger b_{k'\downarrow}\right) \quad \text{(A.17)}$$

$$+ \sum_{kk'\sigma} \left(\frac{V_k^\star V_{k'}}{\epsilon_k - \epsilon_d} - \frac{V_k^\star V_{k'}}{\epsilon_d + U - \epsilon_{k'}} \right) b_{k\sigma}^\dagger b_{k'\sigma} \quad \text{(A.18)}$$

The first term of this Hamiltonian has the same form as the Kondo model in Eq. (3.2), with

$$J_{kk'} = V_k^\star V_{k'} \left(\frac{1}{\epsilon_d + U - \epsilon_{k'}} + \frac{1}{\epsilon_k - \epsilon_d} \right). \quad \text{(A.19)}$$

The second term is the scattering term:

$$K_{kk'} = V_k^\star V_{k'} \left(\frac{1}{\epsilon_k - \epsilon_d} - \frac{1}{\epsilon_d + U - \epsilon_{k'}} \right) \quad \text{(A.20)}$$